الجمهورية الجـزائريـة الديمقراطيـة الشـعبيــة
PEOPLE'S DEMOCRATIC REPUBLIC OF ALGERIA
وزارة التعليم العــالي والبـحث العلمي
MINISTERY OF HIGH EDUCATION AND SCIENTIFIC RESEARCH

جـامعة سعد دحلـب البليــدة1
UNIVERSITY of SAAD DAHLEB BLIDA 1
كلية العلوم – دائرة الفيزياء
Faculty of Sciences - Department of Physics

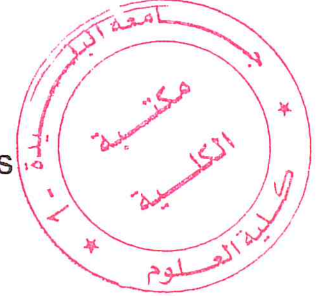

جامعة البليدة 1 - مكتبة الكلية - كلية العلوم

MASTER DIPLOMA THESIS

In Physics
Option: Applied Physics in Microsystems.

THEME

MODELING AND DESIGN OF GRAPHENE/GaAs SOLAR CELL

By:

- **ABDESSELAM Rachid**
- **NEFFAI Mohamed**

Members of Jury:

Mr. A. BENHAFFAF	MAA	Université Blida 1	President
Dr. H. TAHI	MCB	CDTA Baba Hassene	Examiner
Dr. A. HASSEIN-BEY / A.TAHRAOUI	MCB	Université Blida 1	Thesis Advisors

Blida, September 2017

Abstract

The discovery of Graphene has allowed researchers to access a whole new world, the 2D Materials world. Since its discovery in 2004, many researches have been done to study its properties and how it can contribute to more than Moore microelectronics, above its very promising properties in PV solar cells.

In this thesis, we have tried to remake a study that was done in late 2014 by Yawei Kuang and Yushen Liu from the *School of Physics and Electronic Engineering*, in *Changshu Institute of Technology*, China, where a Graphene/GaAs Schottky Junction Solar Cell was modeled and designed using SILVACO ATLAS (TCAD) simulation tool.

We have developed our own SILVACO ATLAS (TCAD) simulation program. Simulations were done under AM1.5 illumination, with different GaAs substrate thicknesses and different n-type doping concentrations, allowing us to obtain efficiencies near 9.54%.

Résumé

La découverte du Graphène a permis aux chercheurs d'accéder à un tout nouveau monde, le monde de Matériaux 2D. Depuis sa découverte en 2004, de nombreuses recherches ont été faites pour étudier ses propriétés et comment peuvent-elles contribuer à l'électronique moderne, notamment dans la photovoltaïque.

Dans cette thèse, nous avons essayé de refaire une étude menée en fin 2014 par Yawei Kuang et Yushen Liu de « l'École de physique et de génie électronique » de « *Changshu Institute of Technology* » en Chine, où une cellule solaire à base de Graphène / GaAs à jonction Schottky a été modélisée et conçue à l'aide de l'outil de simulation SILVACO ATLAS (TCAD).

Notre simulation a été effectuée sous éclairage AM1.5, avec différentes épaisseurs de substrat de GaAs et différentes concentrations de dopage de type n, ce qui nous permet d'obtenir des rendements proches de 9.54%.

ملخص

لقد مكّن اكتشاف "الغرافين" الباحثين من الولوج إلى عالم جديد في علوم المادة، ألا وهو عالم "المواد ثنائية الأبعاد". منذ اكتشافه عام 2004 قام الباحثون بعدة بحوث لدراسة خصائصه وكيفية تأثيرها على ميدان الإلكترونيك المعاصرة، خاصة في مجال الطاقة الشمسية.

لقد قمنا في هذه المذكرة بمحاولة إعادة إجراء دراسة قام بها الباحثان "ياوي كوان" و "يوشن لو" من معهد "شانغ شو" للتكنولوجيا بالصين، حيث قاما سنة 2014 بنمذجة خلية ضوئية مصنوعة من رقاقة من زرنيخيد الغاليوم "GaAs" مدعمة بأقطاب من "الغرافين"، باستعمال برنامج محاكاة أجهزة أشباه الموصلات SILVACO ATLAS (TCAD) .

لقد أجرينا المحاكاة تحت إشعاع AM1.5 مع تغيير سماكة رقاقة "GaAs" وتركيز النواقل السالبة فيها، ممّا مكننا من الحصول على مردود يقارب 9.54%

Acknowledgements

First, we would like to thank the two persons that Allah has blessed me with in our life; ***Our Parents*** who sacrificed their youth and energy, and gave us all their love and support to transform the lives they gave us into wonderful adventures. We are so glad and blessed to be able to wake up every day and see their smiles. We wish that we make them proud, and that they can finally pick up the fruits of their efforts.

Secondly, we would be more than glad to thank our advisor “Dr. Ahmed Tahraoui” for all the patience, time and efforts that he was so generous to give to us during the period of accomplishing this work. Despite him being very far from his homeland, which caused some difficulties in communication, and the fact that we knew very little about Solar Energy did not prevent him from believing in us and giving us opportunity to learn and work with him. This allowed us to gain valuable knowledge, experience, confidence and a strong will to accomplish this work and try to contribute to the field of Solar Energy. We wish him all the success in all the projects that he is working on.

Above that, we would like to thank “Dr. Abdelkader Hassein-Bey” for the efforts that he put into opening the branch of Nano-physics, which allowed us to access this amazing field of “Microsystems”. In addition to this, we thank him for the efforts that he put into teaching us for longer hours every day, several days a week, all of this to deliver us valuable information that we certainly found helpful in the work reported in this thesis. Furthermore, we should thank him for co-advising us and bringing valuable help by providing us with innovative solutions and encouraging us when facing problems.

We would address our acknowledgements to the members of the jury, starting with the president of the jury “Mr. A.Benhaffaf”, the examiner “Dr. H.Tahi”, and the advisors “Dr. A.Tahraoui” and “Dr. A.Hassein-Bey”, for giving us the honor to examine this work, and for the time and efforts that they have taken to read and correct this manuscript.

We will certainly not forget all the teachers that taught us through all these academic years.

At last, it is more than a pleasure to address our acknowledgement to our family members, friends and every person that gave us material and emotional support, just to push us to study and reach this level.

TABLE OF CONTENTS

Abstract 1
Acknowledgements 2
Table of Contents 4
List of Figures 7
List of Tables 8
I. GENERAL INTRODUCTION 10
II. BACKGROUND 12
1. INTRODUCTION 13
2. SEMICONDUCTOR BASICS 13
2.1. Atomic Structure and Quantum Theory 13
2.2. The Crystal Lattice 14
2.3. Energy Bands 16
2.4. Charge Carries 18
2.5. Doping 18
2.6. The P-N Junction 19
2.7. Metal/Semi-Conductor (Schottky) Junction 20
3. SOLAR CELL OPERATION 27
3.1. Origin of Solar Power 27
3.2. Solar Cell Characteristics 28
3.3. Solar Cell Input Power 29
3.4. Solar Cell Performance 32
4. CHAPTER SUMMARY 33
III. GRAPHENE AND GaAs PROPERTIES 34
III.I. GaAs MATERIAL PROPERTIES 35
1. INTRODUCTION 35
2. DEFINITION OF III-V SEMICONDUCTOR MATERIALS 35
2.1. Binary compounds 36
3. THE IMPORTANCE OF III-V COMPOUNDS IN OPTOELECTRONICS 37
4. GaAs MATERIAL PROPERTIES 38
4.1. Energy Band Structure 38
4.2. Mobility and Drift Velocity 41
4.3. Semi-Insulating GaAs 42
4.4. Crystal Defects 43
4.4.1. Point Defects 43
4.4.2. Dislocations 44
4.4.3. Impurities in GaAs 45

4.5. Thermal Characteristics ... 46
III.II. GRAPHENE: THE NEXT REVOLUTION IN 2D MATERIALS ... 47
1. INTRODUCTION ... 47
2. MATERIALS THAT SHOULD NOT EXIST ... 47
3. BRIEF HISTORY OF GRAPHENE ... 48
4. CARBON ATOM AND STRUCTURE OF GRAPHENE FROM THE CHEMICAL VIEWPOINT ... 49
5. GEOMETRY OF THE BAND STRUCTURE OF GRAPHENE'S HONEYCOMB LATTICE FROM THE PHYSICAL VIEWPOINT ... 55
5.1. Bloch Wave Function and Tight Binding Approach ... 56
5.2. Single Layer Graphene ... 61
5.2.1. The electronic structure of gapped single layer graphene ... 63
5.2.2. The experimental work of single layer graphene ... 64
5.2.3. Single layer graphene Nano-ribbons ... 66
5.3. Bilayer Graphene ... 69
IV. SILVACO (TCAD) SIMULATION AND RESULTS ... 73
IV.I. SILVACO (TCAD) simulation tool ... 74
1. INTRODUCTION ... 74
2. A BRIEF HISTORY ABOUT SILVAVCO ... 74
3. SILVACO (TCAD) SOFTWARE ... 75
4. ATLAS ENVIRONMENT ... 76
4.1. Atlas Operating Mode: ... 78
4.1.1. Syntax of an instruction: ... 78
4.1.2. Instructions' order: ... 79
4.2. Structure Specification: ... 80
4.2.1. MESHING ... 80
4.2.2. REGION ... 81
4.2.3. ELECTRODES ... 83
4.2.4. DOPING ... 84
4.3. Materials and Model Specification: ... 85
4.3.1. MATERIAL ... 85
4.3.2. MODELS ... 86
4.3.3. CONTACT ... 86
4.3.4. Numerical METHOD selection ... 87
4.4. Solutions Specification ... 87
4.4.1. Defining the light source ... 88
4.4.2. Obtaining solutions ... 88
4.5. Results' Analysis ... 91
IV.II. Simulation Results and Discussion ... 92

1. INTRODUCTION..92
2. THE GRAPHENE PARAMETERS OBTAINED AND USED IN THIS WORK.....92
2.1. The Densities of State (N_C and N_V)..92
2.2. The Refractive Index..93
2.2.1. Complex refractive index..94
2.3. Other properties..95
3. RESULTS AND DISCUSSION...96
3.1. Evaluating Solar Cell's Electrical and Optical Properties..............................96
3.1.1. The effect of GaAs substrate thickness...97
3.1.2. The effect of Graphene Work function...99
3.1.3. The effect of n-type doping...100
4. CHAPTER SUMMARY...101
V. GENERAL CONCLUSION..103
LIST OF SYMBOLS..105
REFERENCES..107

LIST OF FIGURES

Figure 2-1: The atomic structures for amorphous, crystalline, and polycrystalline materials [15] ... 14
Figure 2-2: The diamond lattice is shown with each black dot representing an individual atom and each solid line representing a bond between atoms. [15] ... 15
Figure 2-3: Inter-atomic distance is graphed against energy to show the formation of energy bands in a material. [16] ... 16
Figure 2-4: The relative bandgaps of insulators, semiconductors, and conductors are shown in Figures 4(a), 4(b), and 4(c) respectively. [16] ... 17
Figure 2-5: The junction between an n-doped and p-doped material forms a depletion region. Figure 5(a) shows majority carriers travelling across the junction due to the attraction caused by opposite charge carriers. The barrier caused by newly formed ions is shown in Figures 5(b) and 5(c). From [17] ... 19
Figure 2-6: Metal and semiconductor before contact; band diagram Schottky barrier height. ... 21
Figure 2-7: Metal and semiconductor in contact; band diagram of built-in potential. ... 21
Figure 2-8: Mirrored electric dipole potentials of the Schottky contact depletion region. ... 23
Figure 2-9: Schottky diode with energy band diagram showing the forward flow of electrical current through the diode. ... 24
Figure 2-10: Schottky diode with energy band diagram showing the reverse bias Va applied to the diode that increases the built-in potential ... 25
Figure 2-11: Power is delivered to an external load from a simple n on p solar cell (arrows denote electron flow). [20] ... 28
Figure 2-12: The typical I-V curve for a solar cell that graphs anode voltage against cathode current. V_{oc}, I_{sc}, I_{max}, and V_{max} are shown to display the limiting cases of the I-V curve and the maximum power point. [21] ... 29
Figure 2-13: Spectral irradiance of the AM0g and AM1.5g spectrums [25] ... 30
Figure 2-14: The spectral responses of gallium indium phosphide (GaInP), gallium arsenide (GaAs), and germanium (Ge) solar cells are graphed along with the AM0 spectrum. [21] ... 31
Figure 3-1: Part from the periodic table with III-V elements highlighted in red ... 36
Figure 3-2: Bandgap values for different III-V compounds in function of their lattice constant [28] ... 37
Figure 3-3: Unit cube of GaAs crystal lattice. ... 38
Figure 3-4: Energy band diagram for GaAs ... 40
Figure 3-5: Energy band structure of Si and GaAs. ... 40
Figure 3-6: Drift velocity of electrons in GaAs and Si as a function of the electric field ... 41
Figure 3-7: Energy band diagram for GaAs. ... 46
Figure 3-8: (a) Schematic representation of and bonds in graphene [75] ... 52
Figure 3-9: (a) Lattice structure of graphite as graphene multilayer ... 55
Figure 3-10: (a) Graphene honeycomb lattice structure with the two graphene sublattices ... 57
Figure 3-11: Energy dispersion in the honeycomb graphene lattice [94] ... 61
Figure 3-12: Optical microscope image of a graphene flake [108] ... 66

Figure 3-13: The finite-width honeycomb structure of graphene nanoribbons......68
Figure 3-14: (a) Schematic diagram of lattice structure of bilayer graphene 71
Figure 4-1: The Virtual Wafer Fabrication [138] 75
Figure 4-2: Inputs and outputs of Atlas [138]...76
Figure 4-3: DECKBUILD window...78
Figure 4-4: Order of groups of Atlas commands [138]......................................79
Figure 4-5: The structure of our Graphene/GaAs solar cell that we want to simulate in SILVACO TCAD 80
Figure 4-6: The mesh statements creating the mesh for the Graphene/GaAs solar cell are displayed along with a picture of the created mesh 81
Figure 4-7: The region statements creating the regions of the Graphene/GaAs solar cell are displayed along with a picture of the created regions. 82
Figure 4-8: A magnified section for areas with specific materials 83
Figure 4-9: The cathode and the anode are made together with the electrode identification code in the Graphene/GaAs solar cell. 84
Figure 4-10: Photogeneration data is displayed in different areas of the solar cell.89
Figure 4-11: The I-V curve of a silicon solar cell as it is displayed in Tonyplot. 91
Figure 4-12: The refraction of a red-light beam traveling between two materials with different refractive indices...95
Figure 4-13: Real and Imaginary refractive index of graphene versus Optical Wavelength [132].. 96
Figure 4-14: The Photogeneration rate in GaAs substrate under AM1.5 illumination versus different thicknesses..98
Figure 4-15: Current-Voltage curves of Graphene-GaAs solar cell versus different GaAs thicknesses...99
Figure 4-16: Current-Voltage curves of Graphene-GaAs solar cell versus different Graphene Work functions.. 101
Figure 4-17: Current-Voltage curves of Graphene-GaAs solar cell versus different n-type doping concentrations...102

LIST OF TABLES

Table 2-1: All possible values of all possible quantum numbers.....................15
Table 3-1: Parameters of the main III-V binary compounds [27] 38
Table 3-2: Room-temperature properties of GaAs 40
Table 4-1: The parameters of graphene that were used in the simulation........99
Table 4-2: Results of the simulation for different parameters 100

I. GENERAL INTRODUCTION

The discovery of "graphene", the first two-dimensional flat material, in which carbon atoms are arranged periodically in a honeycomb lattice, is the block for most of the allotropes of carbon except diamond and amorphous structures. Graphene has shown highly desirable properties such as high transparency, extremely high charge carrier mobility, thermodynamic stability and mechanical hardness [1].

Graphene in its primary stage of development has been a very good candidate for applications such as field-effect transistors [2], transparent electrodes [3], liquid crystal devices [4], ultra-capacitors [5], ultra-tough paper [6], gas molecule detection [7], Li ion battery [8], field electron emitters [9,10] and solar cells [11,12]

The high transparency accompanied with large conductivity favors graphene as a very suitable material for transparent conductive electrode for thin film solar cells. Another important aspect of graphene is its thickness dependent semiconducting property which may favor its application in forming Schottky junction with suitable metals. [13]

For all these reasons, graphene has attracted many researchers all around the world to work and develop new devices based on graphene.

For the scope of this work, we used SILVACO ALTAS (TCAD) software to simulate a Graphene/GaAs Schottky junction. The results show a net improvement in the efficiency of the cell compared to other GaAs Schottky solar cells reported in literature. For comparison sake, we compared the ITO/GaAs with Graphene/GaAs. The results show that Graphene/GaAs junction solar cell outperforms the ITO/ GaAs junction solar cells.

The second chapter describes the fundamentals of semiconductors and solar cells. In the third chapter, we explain in details the physical and properties of GaAs and Graphene materials.

In the first part of chapter four, we explain SILVACO atlas software language and show how we should deal with this software. The second part deals with the simulation results.

Finally, this work has a conclusion that presents our results and a proposal for future work.

Chapter II

BACKGROUND

1. INTRODUCTION

The use of **Graphene** to improve the efficiency of solar cells is investigated in this thesis. To understand how **Graphene Based Solar Cells** function, a basic understanding of semiconductor physics is required. The fundamental principles of semiconductor physics and solar cells are reviewed in this chapter.

2. SEMICONDUCTOR BASICS

Semiconductors are materials that can act either as an electrical insulator or conductor based on the conditions in which they operate. This behavior is due to the bonding properties of the individual atoms that form a bulk material and the interactions between their outer electrons. The individual atoms of semiconductors, like all other toms, have a set structure that determines how they will bond with other atoms.

2.1. Atomic Structure and Quantum Theory

An individual atom consists of positively charged protons, neutrons with no charge, and negatively charged electrons. It is held together by the attractive forces of the oppositely charged protons and electrons. The structure of an atom consists of a central nucleus composed of protons and neutrons that is orbited by a cloud of electrons. This electron cloud is made up of quantized shells that have an associated energy level. Every electron in this orbiting cloud must reside at a quantized energy level. An electron can move to a higher energy shell by absorbing energy or drop to a lower shell by releasing energy. This arrangement of electrons in the quantized shells is the most important determining factor in an atom's interactions with other atoms and, therefore, its electrical properties.

In every atom, each electron has a unique set of quantum numbers which describe its energy state in the atom. The four quantum numbers are represented by the letters n, l, m, and s. The first number n represents the shell that the electron occupies. Higher shell levels have electrons in higher energy states than lower shell levels. The l and m numbers denote subshells that appear within each shell and each can hold two electrons of4 opposite spin. The s number represents the spin of the electron and can either be a positive or negative value. The possible values of each of the quantum numbers are summarized in Table 1.

Table 2-1. All possible values of all possible quantum numbers

Quantum Number	Possible Quantum Number Values
N	$n = (1, 2, 3, ..., n)$ where n corresponds to the energy level of the outermost shell
L	$l = (0, 1, 2, ..., n-1)$
M	$m = (-l, -l+1, ..., l-1, l)$
S	$s = (-1/2, +1/2)$

2.2. Crystal Lattice

Every solid material is made up of individual atoms organized in a certain manner and can be classified as amorphous, crystalline, or polycrystalline based on their arrangement. The basic lattice structure of amorphous, crystalline, and polycrystalline materials is shown in Figure 2-1. The most abundant solids found naturally on the earth are usually amorphous, meaning their individual atoms have no ordered arrangement. Contrastingly, a crystalline material is a material that has a periodic arrangement of atoms, called a crystal lattice, which is repeated throughout the solid. Therefore, the solid appears the same when examined at the atomic level at any point. Materials that do not fall into either the amorphous or crystalline category are classified as polycrystalline. These materials are composed of different regions that each have a periodic arrangement of atoms, but the whole material is not uniform in its arrangement.

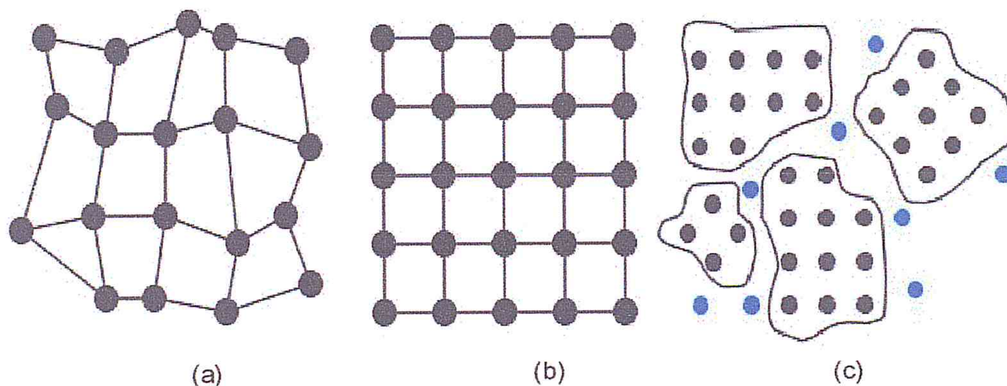

Figure 2-1: (a), 2-1(b), and 2-1(c) show the atomic structures for amorphous, crystalline, and polycrystalline materials respectively [15].

Crystalline solids, which are the most commonly used materials in solar cell applications, can be further classified based on the type of structure of their crystal lattice. Every lattice can be reduced to a unit cell, a small volume which is representative of the whole cell. This unit cell forms a geometry which can take many forms. The most common forms are the variations of the cubic and diamond lattices. An example of a diamond crystal lattice is given in Figure 2. A material can be thought of as a large object composed of large quantities of these unit cells put together as building blocks.

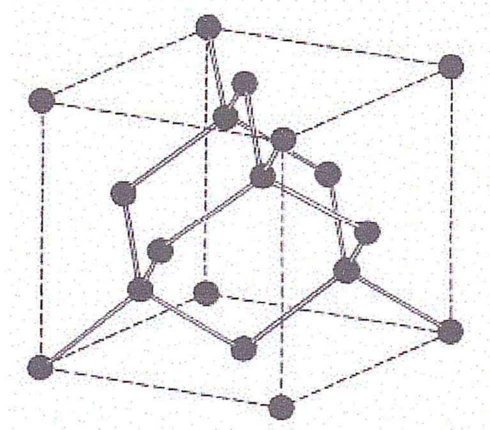

Figure 2-2: The diamond lattice is shown with each black dot representing an individual atom and each solid line representing a bond between atoms [15].

A semiconductor material's unit cell structure determines many of its important properties in solar and electrical applications. The numbers and types of bonds between atoms of the material determine the characteristics of the flow of charge carriers in the material, defining parameters such as resistivity and conductance. The arrangement of the atoms also determines whether certain materials can be grown in layers adjacent to one another to create a certain device. If two material lattice structures do not match in a certain manner, lattice mismatch will occur, a condition in which the lattices of two adjacent materials cannot create an appropriate electrical interface due to conflicting lattice structures. These properties governed by the crystal lattice combine with the properties and structure of the individual atoms to give every material unique properties.

2.3. Energy Bands

In much the same way that electrons can only reside at certain quantized energy levels in an individual atom, they are restricted to inhabiting energy bands in a solid. However, each of these energy bands is made up of a range of energy levels that each electron can occupy. This difference arises from the influence of all neighboring atoms on an electron. In the case of an individual atom, an electron resides in a quantized shell with an associated energy level. If two atoms are close enough to each other, their electrons and other attractive forces will influence each other, creating different energy states in specific bands of energy. In the band diagram in Figure 3, interatomic distance is graphed against electron energy. The band diagram shows that when atoms of the same element are infinitely far away from each other, they have the same quantized energy levels. However, when the atoms are closer together, the electrons of each atom interact, and the discrete energy levels diverge into a band of allowed energies shown by the grey portion of the graph in Figure 2-3.

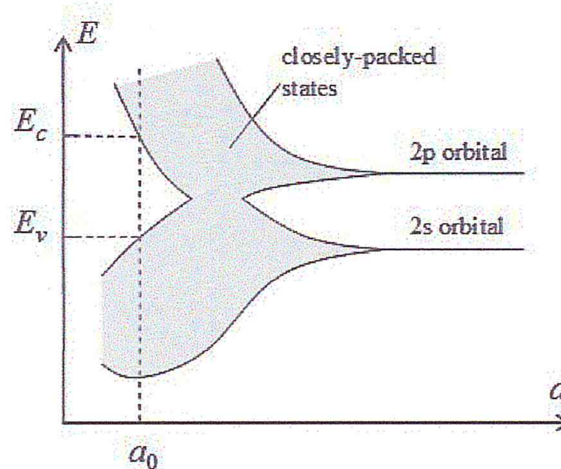

Figure 2-3: Inter-atomic distance is graphed against energy to show the formation of energy bands in a material [16].

The only energy bands of major concern in solar cell applications are the valence band and the conduction band. The valence band is the outermost energy shell of each atom. The electrons in this band are usually held in place by bonds between atoms. If an electron in the valence band receives energy greater than or equal to the difference in energy in the conduction and valence band, known as the bandgap, then it will move into the conduction band. When it moves into the

conduction band, the electron breaks away from its bond and becomes a free electron in the material. An electron can only move up to the conduction when gaining energy in the valence band because there are no allowable energy states for an electron to occupy within the bandgap.

A material's ability to conduct electricity is highly dependent on its bandgap. Insulators have a relatively large bandgap and take a large amount of energy to excite free electrons. Semiconductors have a relatively small bandgap, allowing them to act as an insulating or conducting material dependent on the level of energy in the material. Conductors have overlapping valence and conduction bands and, therefore, have free charge carriers without the addition of outside energy. The differences in bandgap among insulators, semiconductors, and conductors are shown in Figure 4. The bandgap decreases as conduction ability increases.

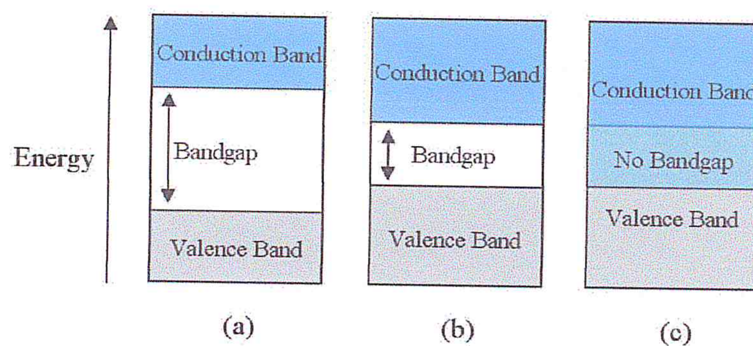

Figure 2-4: The relative bandgaps of insulators, semiconductors, and conductors are shown in Figures 4(a), 4(b), and 4(c) respectively [16].

Semiconductors have a moderate bandgap due to the unique conditions in their valence bands. All elemental or single element semiconductors have four electrons in the valence band of each atom. These elements are known as group IV elements. The atoms of these materials bond with each other to fill the outer shell of each of the surrounding atoms by the use of four covalent bonds with neighboring atoms. These covalent bonds can be broken by the introduction of energy, which frees charge carriers. Other semiconductors are made up of compounds in which the two element's valence electrons sum to eight. This can be achieved in many different elemental combinations to create effective semiconductor materials.

2.4. Charge Carries

When bonds are broken in a material due to the absorption of energy, two different types of charge carriers are created called electrons and holes. Electrons are simply the negatively charged elements of atoms and are considered free electrons when they break away from a bond. Holes are conversely the positive charge left behind by the broken bond of the free electron. Unlike free electrons, holes exist in the valence band. Holes are not physical particles but are merely positive charges created by the lack of necessary electrons for charge balance. Though holes are not physical particles with a mass, their flow is associated with a positive value of current while electron flow is associated with negative current.

Electrons and holes each have an associated mobility in every material based on how easily the free charge carriers can move through the material. Though electrons and holes are of equal charge, electrons have a higher mobility. A material's electron and hole mobility are dependent on many material characteristics such as the lattice structure, the size of the atoms in the material, and the orientation of the channel in which the charge carrier is travelling. The electron and hole mobility determine parameters such as the conductance and resistivity of a material, which are important factors in solar cells.

2.5. Doping

Doping is the process of purposefully introducing impurities into a semiconductor material for the purpose of manipulating its electrical characteristics. A pure, undoped semiconductor is called intrinsic, while a doped semiconductor is called extrinsic. A semiconductor can be doped with either p or n type material. The p type dopants, called acceptors, have three or less valence electrons. This type of dopant bonds with all the surrounding atoms but lacks enough electrons to fully fill its outer shell. Thus, it attracts electrons, inducing the generation of holes in the material. An n type dopant, known as a donor, has five or more valence electrons, allowing it to fully bond with all of the neighboring atoms while leaving an extra, unbonded electron. This electron can easily be excited into the conduction band because it is not bound by the energy of a covalent bond. The extra charge carriers created by doping can greatly increase charge carrier concentrations, allowing for

the fabrication of materials more suited to most applications than intrinsic semiconductors.

2.6. P-N Junction

Most of the applications of semiconductors, including solar cells, are possible due to the properties created by the junction between a p-type region and an n-type region. The region where these two materials meet is called a **p-n junction** and functions as a diode. In this region, excess electrons in the n region and excess holes in the p region diffuse across the border of the two regions to form a depletion region in which oppositely charged ions create a barrier that blocks charge flow. The formation of the depletion region from the junction of p-type and n-type materials is shown in Figure 2-5.

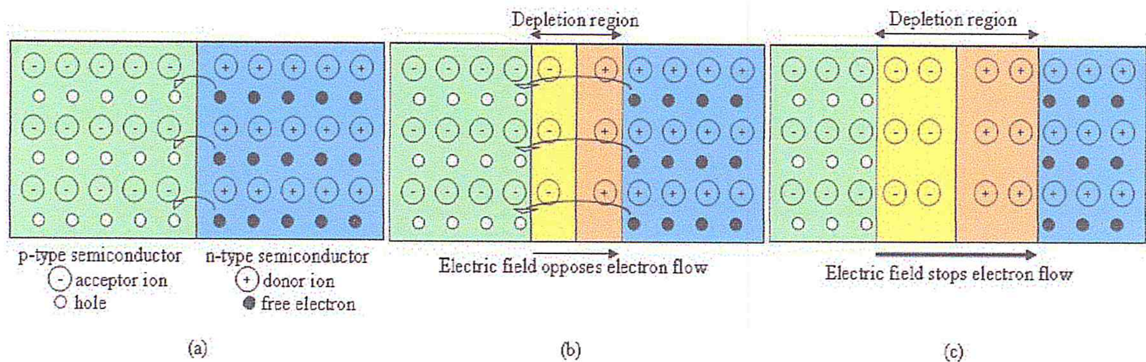

Figure 2-5: The junction between an n-doped and p-doped material forms a depletion region. (a) Shows majority carriers travelling across the junction due to the attraction caused by opposite charge carriers. The barrier caused by newly formed ions is shown in (b) and (c) [17].

The instant the materials meet, the excess carriers of each material border region move to the other side, attracted by the holes or electrons on the other side of the junction. These charges leave behind ions that then have a negative charge in the case of the p side and a positive charge in the case of the n side. This barrier then blocks charge flow because the electrons on the n side are repelled by the negative region on the edge of the n side and the opposite is true of the holes on the p side. If the junction is forward biased with a voltage greater than the potential of the depletion region potential, then the diode conducts current. If the diode is reversed biased, it acts as an insulator and the depletion region expands.

2.7. Metal/Semi-Conductor (Schottky) Junction

The *point contact* diode is one of the earliest solid-state semiconductor devices constructed. This type of diode is made by making contact between a *Metal* a *Semiconductor* surface. The point contact diode was later studied by *Walter H. Schottky* circa 1938 who formulated a theory as to why the diode worked; subsequently this device was named the *Schottky diode* to honor his contributions. Due to the fabrication simplicity of this device, the Schottky diode makes an excellent choice for testing experimental processes in semiconductor manufacturing.

This structure is the basis of a large number of some electronic structures that are more complex than the conventional ones.

The semiconductor material for this study will be *Gallium Arsenide* (**GaAs**) with n-type doping. The material that will mimic the metal that composes the other half of this device (conductor) will be *Graphene*, which always has a large abundance of free electron charge carriers.

All metals have a *work function* ϕ_m: the energy it takes to remove an electron from the atom to the vacuum level potential. The attributes of both metal and semiconductor while separated are illustrated in Figure 2-6. The potential energy needed to inject charge carriers from the metal into the semiconductor material is the *Schottky Barrier Height* measured in *electron volts* (**eV**). The Schottky Barrier Height value is the energy it takes to remove an electron from the metal minus the energy required to detach an electron from the n-type semiconductor material, which is the *electron affinity* χ creating electron flow from the semiconductor to the metal. The Schottky Barrier Height can be calculated for a Schottky diode by the following equation:

$$\phi_B = \phi_m - \chi \qquad (2.1)$$

The Schottky Barrier Height (often referred to as **SBH**) is a fixed amount of energy drop across the diode, this value is unique to the combination of metal and semiconductor, ideally this does not vary with forward voltage biasing or current flow. However, the phenomenon of *SBH lowering* may occur in reverse bias due to electric field crowding [18].

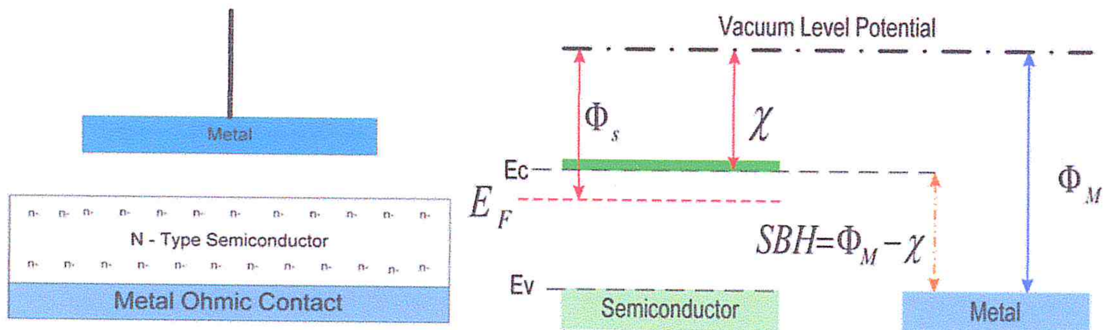

Figure 2-6: Metal and semiconductor before contact; band diagram Schottky barrier height.

When the metal contacts the semiconductor, there is an imbalance of Fermi energy states in the two materials and the charges migrate to reach equilibrium levels. To simplify this matter, some of the electrons in the n-type semiconductor migrate into the metal leaving behind a region of material with no free charge carriers. This area is called the depletion region, and the energy it takes to cross this region is known as the built-in potential. This concept is illustrated in Figure 2-7.

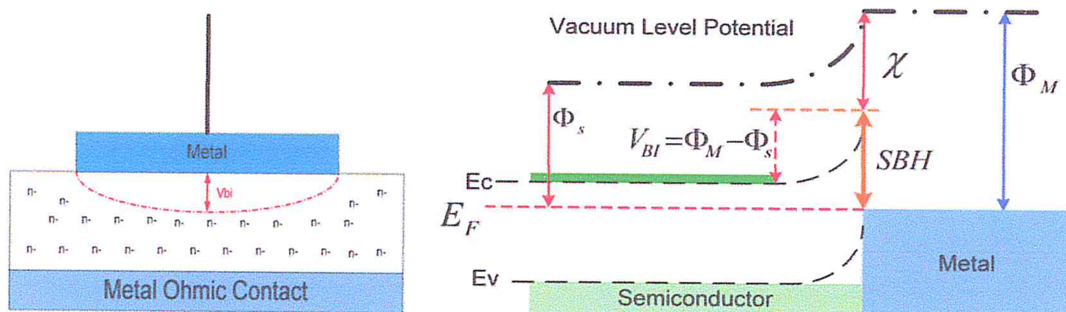

Figure 2-7: Metal and semiconductor in contact; band diagram of built-in potential.

The built-in potential V_{BI} also referred to as "*equilibrium contact potential*" (occurring when the Fermi levels have reached a balance) is the mechanism that prevents any further charge movement from the semiconductor conduction band to

the metal. This built-in potential V_{BI} is the difference in the work function of the metal and the work function of the semiconductor.

$$V_{BI} = \phi_m - \phi_s \tag{2.2}$$

The built-in potential V_{BI}, the applied voltage, and the doping concentration play a large role in the width of the depletion region. This depletion region is absent of charge carriers in the semiconductor essentially behaving as a layer of insulation. The width W of this depletion region is related to both the built-in potential and doping concentration. Where V_a is the applied biasing voltage with N_a and N_d being the acceptor/donor carrier concentrations, it is theorized that electrons (donors) in the n-material migrate into the metal and have a mirrored electric positive (acceptor) potential in the semiconductor opposite the depletion region. So that $N_a = N_d$ and the equation of 1.3 for p-n junctions may be used to model the Schottky diode [19].

$$W = \sqrt{\frac{2\varepsilon.(V_{BI} - V_a)}{q} . \left(\frac{N_a + N_d}{N_a . N_d}\right)} \tag{2.3}$$

The below illustration of Figure 2-8 helps to show why the doping concentration N_a may be considered equal to N_d because of the mirrored electric field in the metal [18]. This depletion width can be manipulated by applying voltage across the device, which will allow for passage of or resistance to the flow of electricity. When a forward biasing voltage V_a is applied to the Schottky diode the work function of the semiconductor material ϕs is reduced and thus the built-in potential is lowered as well.

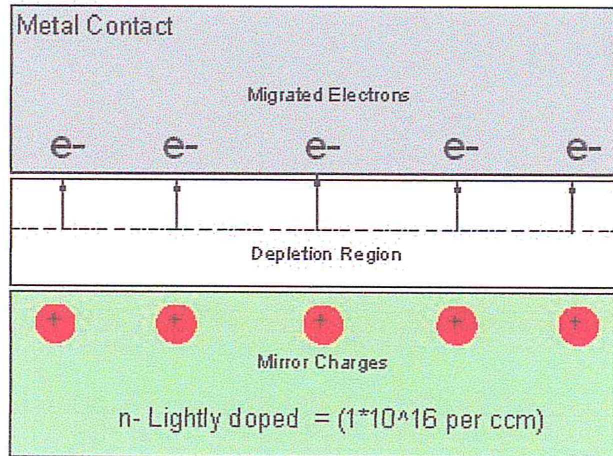

Figure 2-8: Mirrored electric dipole potentials of the Schottky contact depletion region.

The exponential current through the diode can be modeled by equation (2.4) below.

$$I_F = I_0\left(e^{\frac{qV_a}{kT}} - 1\right) \tag{2.4}$$

The forward current I_F through the diode depends exponentially on the applied voltage V_a. The initial current I_0 forms in the depletion region with both with currents both equal and opposite in equilibrium conditions, thus it can be factored out [19].

Figure 2-9 shows an illustration of the conducting diode and the accompanying energy band diagram. During forward bias with the depletion region reduced and the electrons migrating over the Schottky barrier and moving from the n-type semiconductor material to the metal contact. From the energy band diagram, the Fermi level of the semiconductor is raised by the value of the applied voltage. It should be noted that the metal at the bottom of the semiconductor has been prepared to be ohmic having a linear current voltage relationship and possess a very low value of resistance that does not play a role in the ideal analysis of the Schottky diode current [18].

During the reverse bias mode of the Schottky contact the applied voltage reinforces the built-in potential and creates a wider depletion region within the material. Because of the large negative value, the applied voltage the forward current term tends to zero leaving just the reverse initial current that no longer has an opposing forward bias equilibrium current.

$$I_R = -I_0 \quad (2.5)$$

The initial current I_0 of the device under thermal equilibrium can be approximated by knowing the SBH of the diode given equation 2.1 along with the charge of the electron and the thermal voltage [18].

$$I_0 \propto e^{\frac{-q\phi_B}{kT}} \quad (2.6)$$

During reverse bias with the depletion region widens and the only electrons that migrate over the Schottky barrier, those that existed in thermal equilibrium of the initial current I_0. Figure 2-10 shows a reverse bias diode illustration and the band diagram of the Fermi level of the semiconductor lowered by the value of the applied voltage.

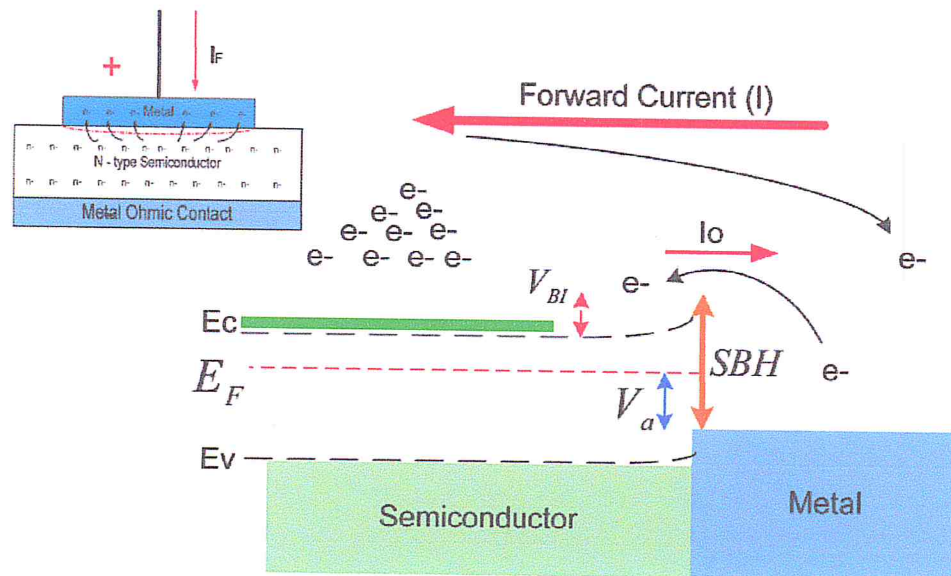

Figure 2-9: Schottky diode with energy band diagram showing the forward flow of electrical current through the diode.

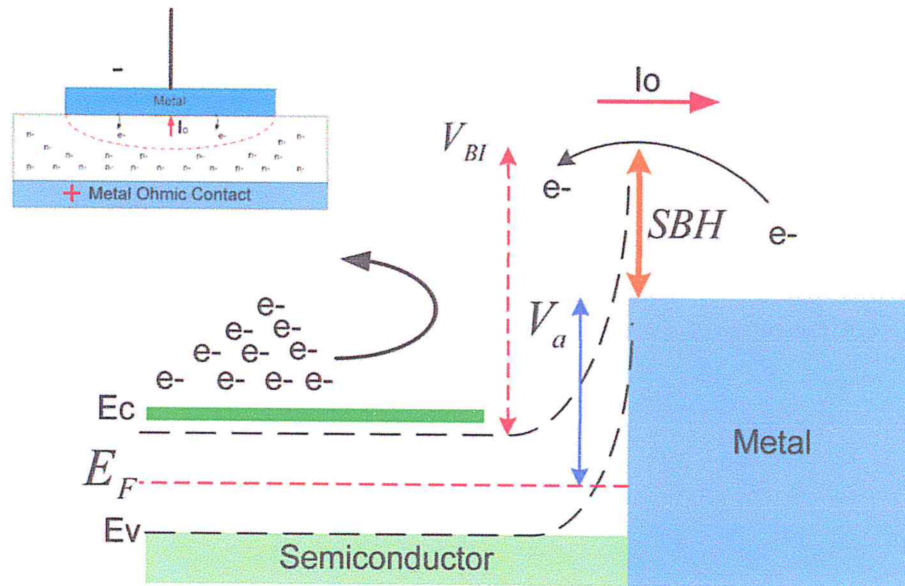

Figure 2-10: Schottky diode with energy band diagram showing the reverse bias V_a applied to the diode that increases the built-in potential.

Aspects that affect the magnitude of current through the ideal Schottky diode are the area (A) of the metal contacting the semiconductor, the temperature (T) of the material, and the Richardson's constant (A*) for the material which is a relation of current density and temperature. With these values known for the material, a more accurate and comprehensive formula for the Schottky diode contact current may be expressed by equation 2.7. This equation also accommodates deviation from ideal diode performance by a factor of n. This value is known as the ideality factor and for the ideal diode; this value should be nearly equal to one.

$$I_F = A.A^*.T^2 e^{\frac{-q\phi_B}{kT}}\left(e^{\frac{qV_a}{nkT}} - 1\right) \tag{2.7}$$

Now that a more accurate expression to describe the Schottky diode has been composed, it is necessary to discuss some of the aspects of the non-ideal Schottky diode. Various aspects of the material and fabrication will cause considerable deviation from the diode performance predicted by equation 2.7. Some of the ways in which variation from the ideal diode characteristics can occur are offset potentials and linearization due to resistance. While in the reverse direction carrier generation can cause a steadily increase current greater than that

of I_o and conduction of electrical current in reverse bias will occur due to Zener and avalanche breakdown [19].

Current linearization due to on resistance could be the cause of a poor quality ohmic contact or a poor quality Schottky contact interface. Both of these will contribute to a high series resistance within the diode. When large currents and voltages are applied to the diode the otherwise exponential I-V curve will become linear. At this point the linear part of the I-V curve may be evaluated with the help of equation 1.8 and the value for the total series resistance of the diode may be calculated by finding the change in voltage over the change in current [19].

$$R_s = \frac{\Delta V}{\Delta I} \tag{2.8}$$

In the reverse bias operation of a Schottky diode there are several mechanisms that create current flow through when the diode should be in a high resistance mode due the applied reverse polarity. Carrier generation in a neutral transition region occurs due to thermal activity and the nature of the semiconductor in regard to what carrier generation - recombination centers may be in the material. A significant aspect of the diode is the reverse breakdown voltage that occurs when the diode in the reverse bias mode begins to conduct electrical current exponentially. There are generally two mechanisms that contribute to reverse bias breakdown. These phenomena are known as avalanche multiplication and quantum mechanical tunneling. Neither of these two breakdown methods will destroy the diode, however heating of the diode could occur due to the high currents due to voltage breakdown which could result in permanent device failure [21]. Avalanche breakdown is created by impact ionization occurring when a large electrical potential is applied across the device and high energy electrons cross the barrier and trigger other electron hole pairs to form. *Zener* breakdown is attributed to a mechanism known as quantum mechanical tunneling which effectively allows the charge to penetrate the barrier of forbidden region. The applied reverse voltage at which these mechanisms of breakdown will occur can be estimated by the following equation of

2.9 that relates the breakdown electric field for the material E_c with the doping concentration N_d [14].

$$V_{RB} = \frac{\varepsilon_0 \varepsilon_m (E_c)^2}{2qN_d} \tag{2.9}$$

The best way to reduce currents resulting from the preceding phenomenon is to reduce the field intensity across the device. One of the most influential aspects to electric field intensity surrounding a Schottky contact is the physical shape of the metal in contact with the semiconductor forming the diode junction. Many techniques for design and construction of Schottky diode contacts implement varied contact geometries so that reverse breakdown voltages may be increased.

3. SOLAR CELL OPERATION

Due to the properties of the p-n junction and the ability of semiconductors to absorb energy via photons of light, solar cells are able to generate power. The basic concepts behind solar power and the important characteristics that can quantify a solar cells performance are explained in this section.

3.1. Origin of Solar Power

A basic solar cell consists of a p-n junction with metal contacts on both sides of the junction. In an n on p solar cell the top n layer is called the emitter, while the bottom p side is called the base. When placed in an environment with light, the solar cell absorbs photons, which generate electron hole pairs near the depletion region. To generate power, the metal contacts to the emitter and base are tied together via an external load as shown in Figure 2-11. Due to the field of the depletion region, charge carriers generated by photons are swept across the depletion region so that a photocurrent is generated in the reverse biased direction. However, when an external load is applied, the current induces a voltage across the load. This voltage induces a countering forward biased current that is less than the photocurrent but increases as the load reaches infinity. The net current in a solar cell is always in the reverse biased direction but decreases as the forward biased current increases with an increasing load. The power produced by the cell is the product of the net current and voltage across the load.

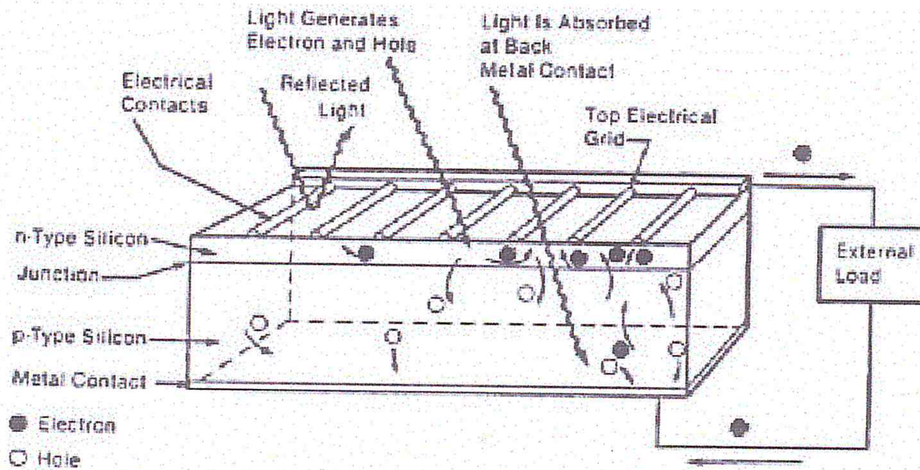

Figure 2-11: Power is delivered to an external load from a simple n on p solar cell (arrows denote electron flow) [20].

3.2. Solar Cell Characteristics

The most useful characteristic of a solar cell is its current-voltage (I-V) curve. This curve graphs the solar cell's net current per unit surface area in the y direction, against the associated load voltage in the x direction. A typical solar cell I-V curve is shown in Figure 2-12, which shows anode voltage plotted against cathode current. As discussed in the previous section, the value of load resistance affects both the load voltage and net current generated in the solar cell. The y intercept of the I-V curve is the limiting case in which there is no load resistance and a maximum value of current called the short circuit current (I_{sc}) occurs. In this case there is no induced voltage across the load, creating no forward biased current to counter the photon induced current. The x intercept represents the extreme case in which the load resistance is infinite, producing a maximum voltage known as the open circuit voltage (V_{oc}). In this case no current can flow due to the infinite resistance. Opposing charges are built up on both sides of the depletion region of the p-n junction, resulting in a maximum voltage across the infinite load. Though it is useful to know I_{sc} and V_{oc} for a solar cell, it is more useful to know the maximum power point (P_{max}). The maximum power current (I_{max}) and voltage (V_{max}) can then be determined. These values show the actual power capability of a solar cell, the most important factor in the cell's application. The parameters V_{oc}, I_{sc}, Imax, and V_{max} are shown in Figure 2-12 on an I-V curve.

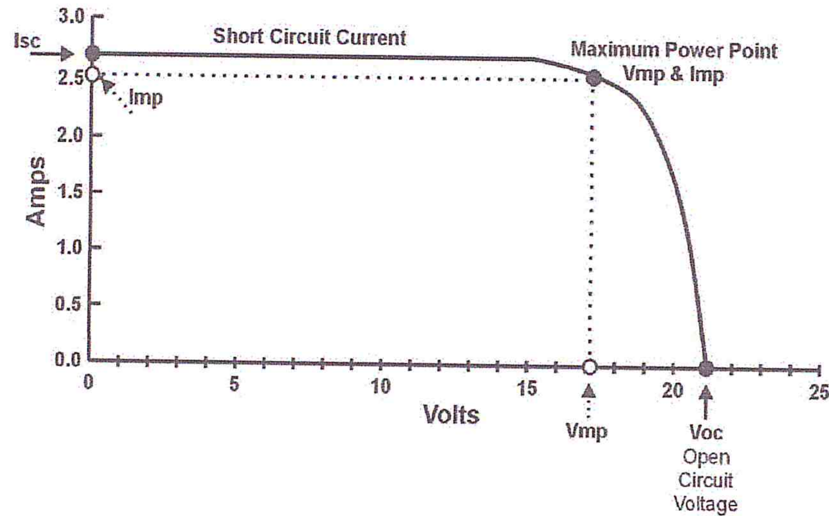

Figure 2-12: The typical I-V curve for a solar cell that graphs anode voltage against cathode current. V_{oc}, I_{sc}, I_{max}, and V_{max} are shown to display the limiting cases of the I-V curve and the maximum power point [21].

Once the I-V curve for a solar cell is determined, many parameters can be calculated which are useful in comparing the performance of different cells. Solar cell efficiency η is given by

$$\eta = \frac{P_{max}}{P_{in}} \times 100\% \qquad (2.10)$$

where P_{max} is the maximum achievable power of the solar cell and Pin is the input power from the light applied to the cell. The fill factor FF is given by

$$FF = \frac{P_{max}}{I_{sc}V_{oc}} \qquad (2.11)$$

where V_{oc} and I_{sc} are the open circuit voltage and short circuit current, respectively. The FF is a measure of how well a solar cell transfers its short circuit current and open circuit voltage properties into actual power. These two parameters are useful for comparing solar cells but are dependent upon the input power to the solar cell, which varies based upon the light source applied.

3.3. Solar Cell Input Power

The input power to a solar cell is dependent upon the light source in which the cell is operating. In this thesis, air mass 1.5 (**AM1.5**) is used. Solar panels do not generally operate under exactly one atmosphere's thickness: if the sun is at an angle to the Earth's surface the effective thickness will be greater. Many of the

world's major population centres, and hence solar installations and industry, across Europe, China, Japan, the United States of America and elsewhere (including northern India, southern Africa and Australia) lie in temperate latitudes. An AM number representing the spectrum at mid-latitudes is therefore much more common. "AM1.5", 1.5 atmosphere thickness, corresponds to a solar zenith angle of z=48.2°. While the summertime AM number for mid-latitudes during the middle parts of the day is less than 1.5, higher figures apply in the morning and evening and at other times of the year. Therefore, AM1.5 is useful to represent the overall yearly average for mid-latitudes. The specific value of 1.5 has been selected in the 1970s for standardization purposes, based on an analysis of solar irradiance data in the conterminous United States. [22] Since then, the solar industry has been using AM1.5 for all standardized testing or rating of terrestrial solar cells or modules, including those used in concentrating systems. The latest AM1.5 standards pertaining to photovoltaic applications are the ASTM G-173[10,11] and IEC 60904, all derived from simulations obtained with the SMARTS code.

Figure 2-13 shows the corresponding spectral irradiance for AM1.5 light beam compared with AM0 (full spectrum) spectral irradiance light beam.

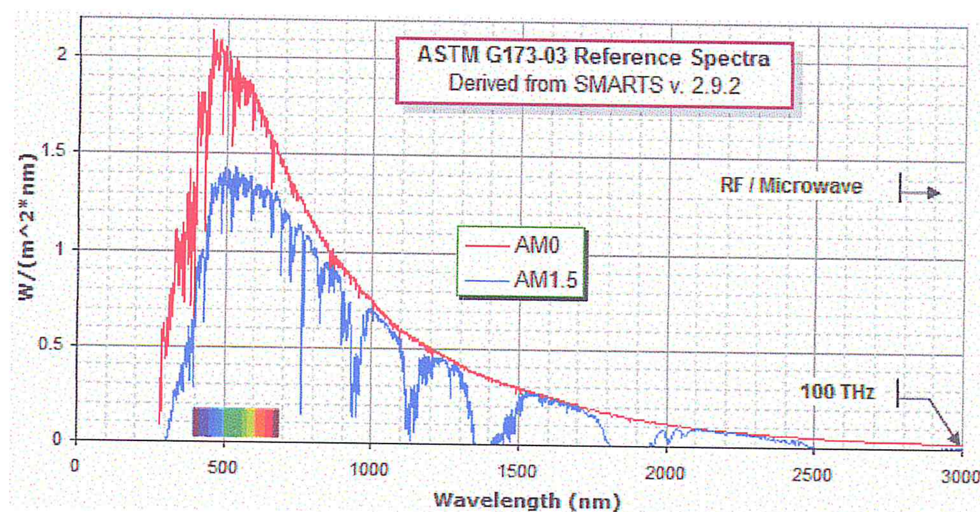

Figure 2-13: Spectral irradiance of the AM0g and AM1.5g spectrums [25].

Due to the properties of solar cells, only part of the solar spectrum can be converted into electrical power. This is caused by the different bandgaps and optical properties of materials. The bandgap of a material determines the minimum amount of energy required to generate an electron hole pair in the material. Any photon with

energy less than the bandgap will simply pass through the material without exciting an electron. The energy of a photon is dependent on its wavelength and is given by

$$E = \frac{1.24}{\lambda} \tag{2.12}$$

where E is in units of eV and λ is the wavelength of the photon in μm. The shorter the wavelength of a photon, the higher its energy and ability to generate electron hole pairs in higher band gap materials.

Though it would seem that lower band gap materials would have the ability to harness the widest range of photons, photons with energies much greater than the band gap of a material are not very efficient at generating electron hole pairs. To easily display a solar cell's response to photon energy, a spectral response curve graphs photon wavelength against the efficiency of charge carrier generation. The spectral response of three different commonly used solar cell materials is given in Figure 9. Different materials have different curves that are limited to a maximum wavelength based on the material band gap and a threshold at which photons have too much energy. In this thesis, the mid-level band gap material gallium arsenide (GaAs) is used. GaAs has a spectral response which indicates efficient charge carrier generation by photons ranging in wavelength from 0.6µm to 0.9µm as seen in Figure 2-14.

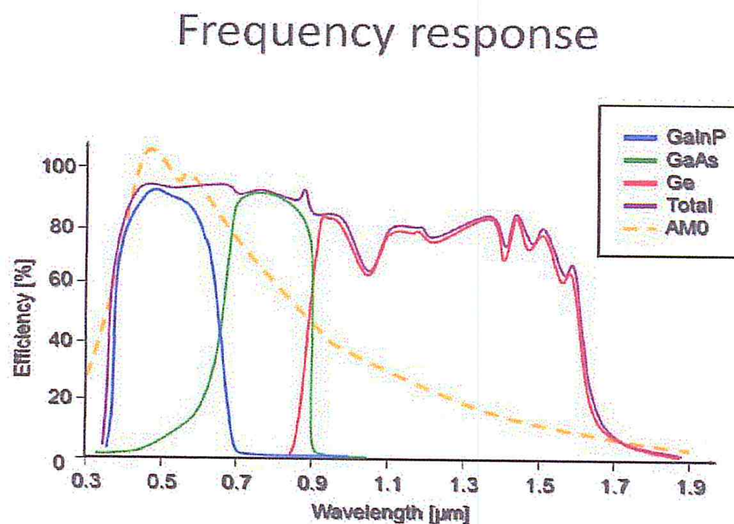

Figure 2-14: The spectral responses of gallium indium phosphide (GaInP), gallium arsenide (GaAs), and germanium (Ge) solar cells are graphed along with the AM0 spectrum [21].

3.4. Solar Cell Performance

Though solar cell performance is largely dominated by a material's spectral response and I-V characteristics, there are many other factors that influence a solar cell's performance. The more important factors that affect solar cell performance are:

- The reflection of light off the surface of a solar cell limits the amount of input power into the cell. The optical properties of different materials cause a portion of the photons hitting the solar cell to be reflected off the surface. This can cause a 35% loss in the theoretical efficiency of a solar cell without the use of antireflective techniques [21].
- Photons with energy much higher than the band gap generate electron hole pairs, but the excess energy is dissipated as heat in the crystal lattice of the solar cell. Low energy photons that do not generate charge carriers also bombard the atoms in the crystal lattice and create heat. This heating causes a loss in the voltage of a solar cell. A solar cell loses 2mV/K in voltage, which can drastically lower the efficiency of a solar cell [21].
- Recombination of electrons and holes can cause the charge carriers generated by photons to meet in the lattice and cancel each other out. When this happens, a free electron meets with a hole in the valence band and occupies that space, no longer contributing to the number of charge carriers in the solar cell [21].
- Material defects in the solar cell can create traps which create more recombination. Cheaper, less pure materials can have significant defects that negate much of the generated current [21].
- The resistance of the bulk material causes a voltage drop within the solar cell that reduces the efficiency. When charge carriers are generated, they have to travel to the contacts of the solar cell to be harnessed as energy. The distance travelled through the lattice is often relatively great for each charge carrier, creating a high resistance seen by each of the charge carriers. This decreases the net voltage seen at the contacts [21].
- Shading from the top electrical contact completely blocks light to portions of the solar cell. The optimal top contact grid usually covers 8% of a solar cell.

This 8% of the solar cell surface receives no photons to generate charge carriers and does not contribute to the power production of the solar cell [20].

The problems of internal resistance and shading in solar cells are addressed in this thesis through the use of Graphene. With a net reduction in the resistance seen by each of the charge carriers and a reduction in the percentage of the solar cell surface covered by the top contact, the efficiency of any solar cell can be increased. The improved conductivity on the surface of a solar cell that could be provided by a Graphene layer could be used as an electrode which collect current. These lines could, therefore, be made thicker, reducing losses from resistance in the grid lines, further increasing the efficiency of a solar cell.

4. CHAPTER SUMMARY

The background in semiconductor physics and solar cells necessary to understand the research in this thesis was provided in this chapter. The basic properties of semiconductors the theory and operations of the Schottky junction were shown to be optimal for generating solar power. The ability to generate electron hole pairs by the absorption of photons with energy greater than the bandgap allows solar cells to deliver power to a load. The producible power was shown to be dependent on both the material of the solar cell and the spectrum of input light. The power was also shown to be limited by factors inherent in the real properties of fabricated solar cells.

The structure and properties of Graphene is covered in the next chapter to provide the basic knowledge necessary in understanding photovoltaic Graphene applications.

Chapter III

Graphene and GaAs Properties.

III.I GaAs MATERIAL PROPERTIES

1. INTRODUCTION

In the set of materials, semiconductors constitute a well-defined class, with particular physical properties that are sources of interest in terms of fundamental knowledge and applications. These two unseparated factors make the importance of these materials, despite the limited number of elements and semiconductor compounds.

Mainly remarkable for their electronic properties, semiconductors are used in almost all electronic and optical equipment. The biggest part of the components (transistors, diodes, and so-called chip in general) are made of silicon, which plays a preponderant role, its technology and its theoretical knowledge have reached unmatched levels.

In fast electronics and optoelectronics, the properties of silicon are insufficient (mobility of relatively small carriers and indirect electronic transitions at the optical absorption threshold). In such applications, the III-V semiconductor compounds are preferable. The properties of these materials are very advantageous for the performances of these devices.

Among these semiconductors, we find mainly the gallium-indium nitride (InGaN) which is at the center of this work. This material is a semiconductor belonging to the category of III-nitrides, that is to say, composed of nitrogen and elements of column III of the Mendeleev table, namely boron, aluminum, Gallium, indium and thallium, see Figure 1.1. Gallium-indium nitride is an alloy between gallium nitride (GaN) and indium nitride (InN). Therefore, we will mainly define the III-V semiconductors and then describe the properties of these two binary alloys (GaN) and (InN), and then describe the properties of the InGaN resulting from them.

2. DEFINITION OF III-V SEMICONDUCTOR MATERIALS

III-V semiconductor materials are compound bodies formed from an element of column III and an element of column V of the table of the Mendeleev periodic table (figure 3-1). Thus, many binary, ternary and quaternary compounds can be produced.

Figure 3-1: Part from the periodic table with III-V elements highlighted in red

2.1. Binary compounds

Of all the possible binary compounds, not all have the same potential interest. The study of their properties, and in particular of the band structure, shows that the lighter elements give compounds of which the band gap is broad and indirect, and in which the effective mass of the electrons is high. Compounds containing boron, aluminum or nitrogen fall into this category; They generally have little interest in fast electronics [26], which requires semiconductors with high carrier mobility or for optoelectronics or a direct band structure is required for optical transitions to be effective [27]. At the other end, heavy elements such as Thallium or Bismuth give compounds based on Gallium (GaAs, GaSb) or Indium (InP, InAs, InSb) whose properties are most interesting. Table 3-1 summarizes some parameters for different III-V family materials.

Table 3-1: Parameters of the main III-V binary compounds [27].

Composé III-V	Eg (ev)	m^*/m_0	μ (cm²/VS)	a (A°)
BN	7,5			3,6150
AlP	2,45			5,4510
AlAs	2,16			5,6605
AlSb	1,58	0,12	200	6,1355
BP	2,0			4,5380
GaN	3,36	0,19	380	a=3,189 (b=5,185)
GaP	2,26	0,82	110	5,4512
GaAs	1,42	0,067	8500	5,6533
GaSp	0,72	0,042	5000	6,0959
InP	1,35	0,077	4600	5,8686
InAs	0,36	0,023	33000	6,0584
InSp	0,17	0,0145	80000	6,4794

3. IMPORTANCE OF III-V COMPOUNDS IN OPTOELECTRONICS

III-V compound semiconductors (SC) have played a crucial role in the development of optoelectronic devices for a broad range of applications. Major applications of InP or GaAs based III-V compound SC are devices for optical fiber communications, infrared and visible LEDs/LDs and high efficiency solar cells. GaAs based compounds are extremely important for Photovoltaic Solar Cell applications. We review its parameters later in this thesis.

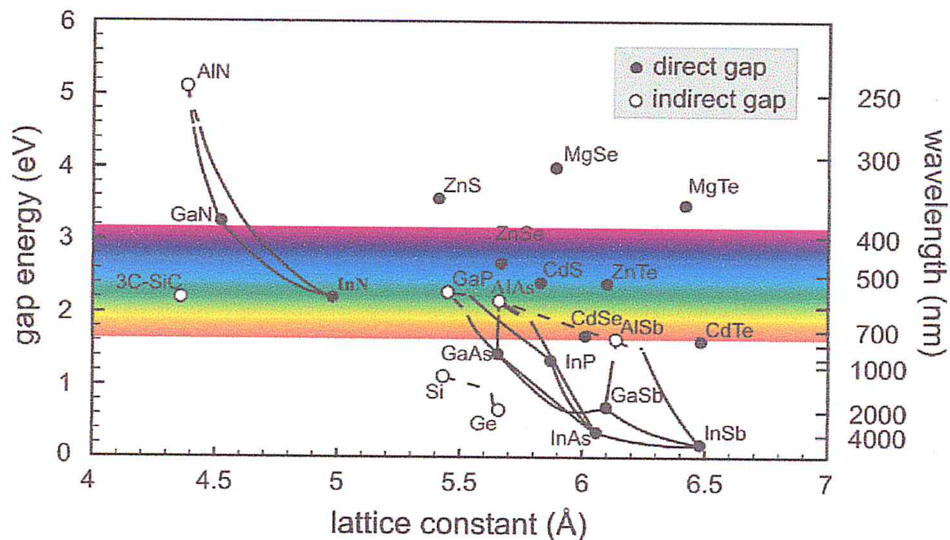

Figure 3-2: Bandgap values for different III-V compounds in function of their lattice constant [28].

4. GaAs MATERIAL PROPERTIES

GaAs is a III–V compound semiconductor composed of the element gallium (Ga) from column III and the element arsenic (As) from column V of the periodic table of the elements. GaAs was first created by Goldschmidt and reported in 1929, but the first reported electronic properties of III–V compounds as semiconductors did not appear until 1952 [29].

The GaAs crystal is composed of two sublattices, each face centered cubic (fcc) and offset with respect to each other by half the diagonal of the fcc cube. This crystal configuration is known as cubic sphalerite or zinc blende. Figure 3-1 shows a unit cube for GaAs and Table 3-2 provides a listing of some of the general material characteristics and properties.

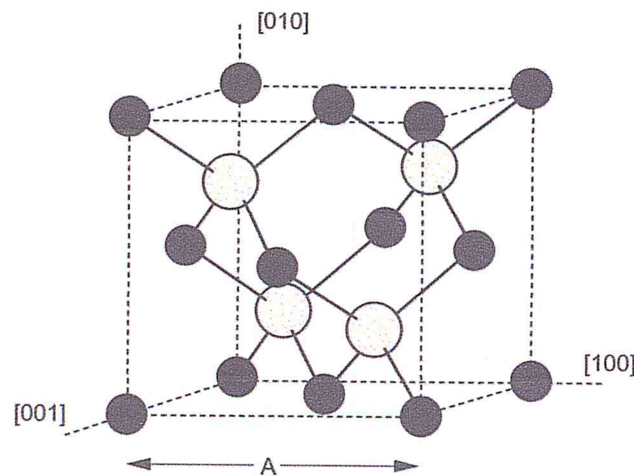

Figure 3-3: Unit cube of GaAs crystal lattice.

4.1. Energy Band Structure

As a result of the laws of quantum mechanics, electrons in isolated atoms can have only certain discrete energy values. As these isolated atoms are brought together to form a crystal, the electrons become restricted not to single energy levels, but rather to ranges of allowed energies, or bands called the valance and conduction bands (Figure 3-4). These two bands are separated by an energy band gap, which is a very important characteristic of the semiconductor material. At zero kelvin, all the electrons are confined to the valance band and the material is a perfect insulator. Above zero kelvin, some electrons have sufficient thermal energy to make a transition to the conduction band where they are free to move and conduct current

through the crystal. The probability of an electron having enough energy to make the transition is given by the Fermi distribution function. The Fermi level shown on Figure 3-2 is the energy level at which the probability function is equal to one-half. For pure semiconductors, the Fermi level is approximately in the center of the band gap. Note, though, that no electron actually has an energy of E_F, since they are not permitted to exist at energies in the band gap. The amount of energy required for an electron to move from the valance band to the conduction band (energy band gap) depends on the temperature, the semiconductor material, and the material's purity and doping profile. For undoped GaAs, the energy band gap at room temperature is 1.42 eV. The energy band diagram is usually referenced to a potential called the vacuum potential. The electron affinity, $q\chi$, is the energy required to remove an electron from the bottom of the conduction band to the vacuum potential. For GaAs, $q\chi$ is approximately 4.07 eV [30,31].

Table 3-2: Room-temperature properties of GaAs.

Property	***Parameter***
Crystal structure	*Zinc blende*
Lattice constant	*5.65 Å*
Density	$5.32\ g/cm^3$
Atomic density	$4.5 \times 10^{22}\ atoms/cm^3$
Molecular weight	*144.64*
Bulk modulus	$7.55 \times 10^{11}\ dyn/cm^2$
Sheer modulus	$3.26 \times 10^{11}\ dyn/cm^2$
Coefficient of thermal expansion	$5.8 \times 10^{-6}\ K^{-1}$
Specific heat	*0.327 J/g-K*
Lattice thermal conductivity	*0.55 W/cm-°C*
Dielectric constant	*12.85*
Band gap	*1.42 eV*
Threshold field	*3.3 kV/cm*
Peak drift velocity	$2.1 \times 10^7\ cm/s$
Electron mobility (undoped)	$8500\ cm^2/V\text{-}s$
Hole mobility (undoped)	$400\ cm^2/V\text{-}s$
Melting point	*1238°C*

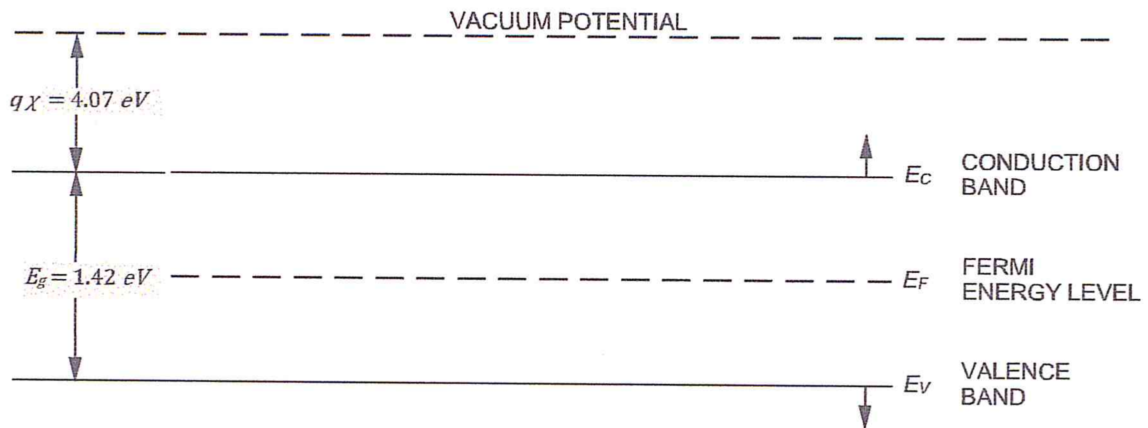

Figure 3-4: Energy band diagram for GaAs

GaAs is a direct band gap semiconductor, which means that the minimum of the conduction band is directly over the maximum of the valance band (Figure 3-5). Transitions between the valance band and the conduction band require only a change in energy, and no change in momentum, unlike indirect band-gap semiconductors such as silicon (Si). This property makes GaAs a very useful material for the manufacture of light emitting diodes and semiconductor lasers, since a photon is emitted when an electron changes energy levels from the conduction band to the valance band.

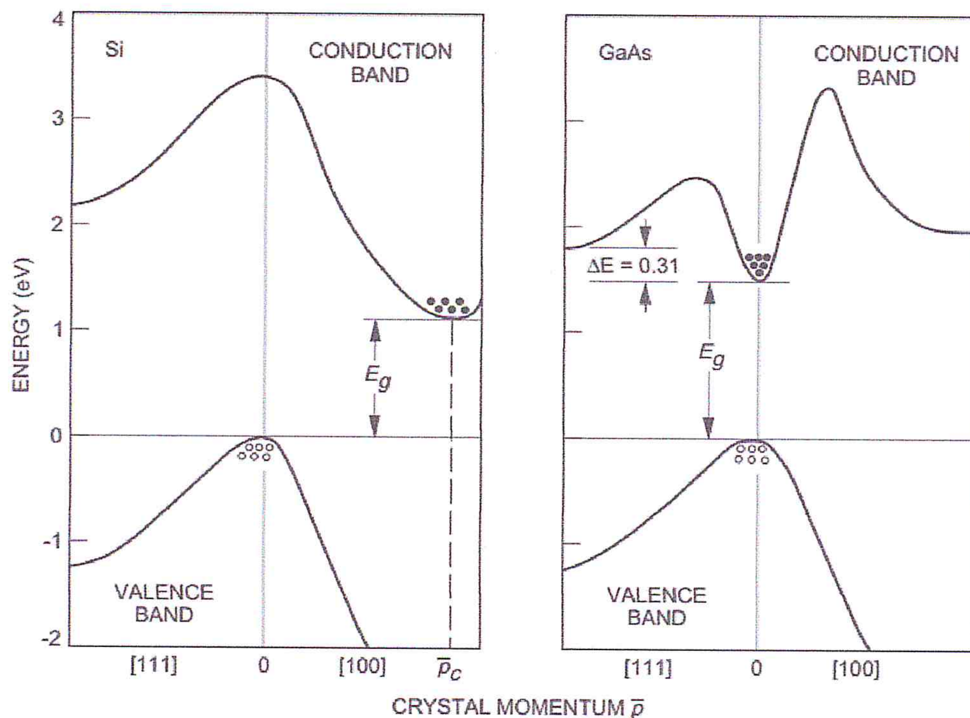

Figure 3-5: Energy band structure of Si and GaAs.

Alternatively, an incident photon can excite an electron from the valence band to the conduction band, allowing GaAs to be used in photo detectors.

4.2. Mobility and Drift Velocity

GaAs has several advantages over silicon for operation in the microwave region—primarily, higher mobility and saturated drift velocity and the capability to produce devices on a semi-insulating substrate.

In a semiconductor, when a carrier (an electron) is subjected to an electric field, it will experience a force ($F = -qE$) and will be accelerated along the field. During the time between collisions with other carrier ions and the semiconductor lattice, the carrier will achieve a velocity that is a function of the electric field strength. This velocity is defined as the drift velocity (ν). From the conservation of momentum, it can be shown that the drift velocity (ν) is proportional to the applied electric field (Figure 3-6) and can be expressed as

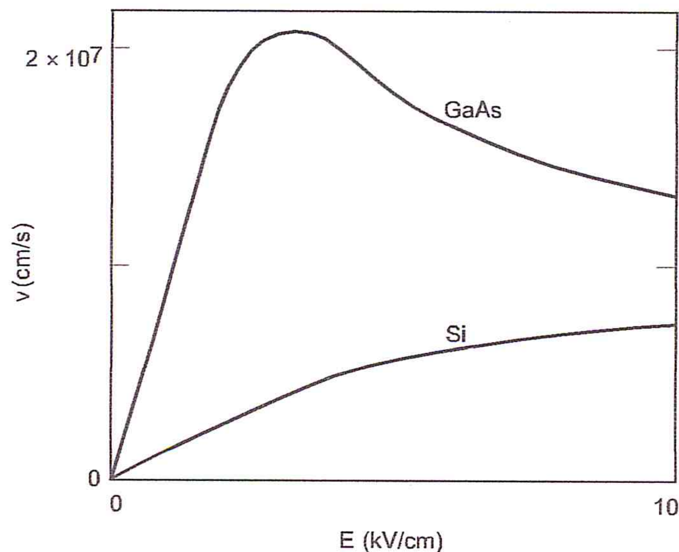

Figure 3-6: Drift velocity of electrons in GaAs and Si as a function of the electric field.

$$\nu = -\left(\frac{q\tau_c}{m^*}\right) E \tag{3.1}$$

The proportionality factor depends on the mean free time between collisions (τ_c) and the electron effective mass (m^*). The proportionality factor is called the electron mobility (μ) in units of $cm^2/V\text{-}s$.

Mobility is an important parameter for carrier transport because it describes how strongly the motion of an electron is influenced by an applied electric field. From the equation above, it is evident that mobility is related directly to the mean free time between collisions, which in turn is determined primarily by lattice scattering and impurity scattering. Lattice scattering, which is a result of thermal vibrations of the lattice, increases with temperature and becomes dominant at high temperatures; therefore, the mobility decreases with increasing temperature. Impurity scattering on the other hand, which is a result of the movement of a carrier past an ionized dopant impurity, becomes less significant at higher temperatures [30].

Although the peak mobility of GaAs in the linear region can be as much as six times greater than that of silicon (Si) at typical field strengths, the advantage of GaAs may be only as much as a factor of two [32]. This still translates to the fact that GaAs devices can work at significantly higher frequencies than Si. The exact increase in the speed of operation depends on factors such as the circuit capacitance and the electric field regime in which the device operates.

4.3. Semi-Insulating GaAs

The importance of semi-insulating GaAs is based on the fact that devices made of it by direct ion implantation are self-isolating, so that it is ideally suited to integrated circuit fabrication. Moreover, the semi-insulating substrate provides greatly reduced parasitic capacitances, thus faster devices, and allows for integration and the implementation of monolithic microwave integrated circuits (MMIC).

Semi-insulating GaAs must meet the following requirements to provide semiconductor quality material:

(1) Thermal stability during epitaxial growth or anneal of ion-implanted active layer.

(2) Absence of undesirable substrate active layer interface effects, such as back-gating and light sensitivity.

(3) No degradation of active layer properties by out-diffusion of impurities from substrate during thermal processing.

(4) Lowest possible density of crystalline defects, such as dislocations, stacking faults, and precipitates.

To achieve some of these requirements, buffer layer technology was developed. A buffer layer is a relatively thick, high-resistivity epitaxial layer grown on the semi-insulating substrate. Another epitaxial layer is then grown on the buffer layer and used for the active layer. The buffer layer provides a physical barrier for undesirable substrate impurities and imperfections.

GaAs bulk resistivity can range from 10^{-6} Ω-cm to about 10^{22} Ω-cm, with the practical range being 10^{-3} Ω-cm to 10^{8} Ω-cm. This high resistivity is about six orders of magnitude greater than that of silicon and provides excellent isolation and substrate insulation. Undoped GaAs can be made semi-insulating by the addition of either oxygen or chromium to the melt. The resistivity of the semiconductor can be controlled by counter doping with a deep-level impurity that has a conductivity type opposite to that of the impurities introduced during growth.

4.4. Crystal Defects

No semiconductor crystalline material is perfect, and GaAs crystals, in spite of the efforts to control crystal growth, contain a number of crystal defects, dislocations, and impurities. These defects can have either desirable or undesirable effects on the electronic properties of GaAs. The natures of these defects and the observed effects are determined by the method of their incorporation into the material and the general growth conditions.

4.4.1. Point Defects

Localized defects of atomic dimensions, called point defects, can occur in an otherwise perfect crystal lattice. These point defects can include vacancies, interstitials, misplaced atoms, intentionally introduced dopant impurities, and

impurities introduced inadvertently during the material growth process. The study of point defects is important because of the effect these defects have on the electronic properties of the material and the strong relationship between diffusion and the number and type of defects in the crystalline material. The electrical properties of a semiconductor can be manipulated by the deliberate insertion of chemical defects (impurities) into the material during the growth and processing steps. However, intrinsic defects present in the material also play an important role in the electronic behavior of GaAs.

Many intrinsic defects are observed in GaAs. The concentration and effect of these defects are determined by the manner in which the material is grown. Intrinsic defects in GaAs include both arsenic and gallium vacancies, their concentration being determined by the overpressure of arsenic during processing. The effect of these vacancy defects has been observed to be neutral [33], deep donor-like, and deep acceptor-like [34].

EL2, an important defect in GaAs, is present in material grown from an arsenic-rich melt. This defect is donor-like in character and is located at the middle of the energy gap [35]. It is thermally very stable and can withstand processing temperatures up to 900°C, and acts as an electron trap. The importance of this defect lies in its ability to convert p-type GaAs to semi-insulating material, and its thermal stability.

4.4.2. Dislocations

A dislocation is a one-dimensional array of point defects in an otherwise perfect crystal. It occurs when the crystal is subjected to stresses in excess of the elastic limit of the material. Dislocations interact with chemical and other point defects. This interaction exists between the localized impurity atoms and the strain field near the dislocations. The presence of a dislocation is usually associated with an enhanced rate of impurity diffusion leading to the formation of diffusion pipes. This effect translates to the introduction of trapping states in the band gap, altering the etching properties of the wafer, and, most importantly, altering the electrical properties of the devices. Studies have shown detrimental effects of dislocations

and dislocation densities on the source drain current and threshold voltage of field-effect transistors FETs [36,37], carrier concentration, and sheet resistance [38].

Dislocations generally are introduced as a result of a temperature gradient present during crystal growth. Modern crystal growth methods can routinely produce 7.6-cm (3-in.) wafers with dislocation densities of 10^4 to 10^5 cm^{-2} for the Liquid Encapsulated Czochralski (LEC) and 8000 to 25,000 cm^{-2} for Horizontal Bridgeman (HB) techniques.

4.4.3. Impurities in GaAs

Chemical point defects (doping impurities) can be introduced to the crystalline material either deliberately or inadvertently as contamination during processing. In general, substitutional impurities are electronically active, whereas many contaminants are interstitial in nature and are electronically inactive. Dopants are classified as either donors or acceptors. A donor has one more electron than the atom it is replacing in the crystal. This extra electron is easily removed or donated to the conduction current. An acceptor, on the other hand, has one less electron than the atom it is replacing. Thus, an acceptor can easily capture an electron and prevent it from adding to the conduction current. Regardless of the type or character of the impurity, the electrical properties of the semiconductor are altered.

Figure 3-7 shows the energy band diagram of Figure 3-4 with the addition of impurities. Shallow donor or acceptor impurities have energy levels within $3kT$ of the conduction and valance band, respectively. Since the energy required for an electron to transition from these impurity energy levels to the nearest band edge is very small, they are typically fully ionized at room temperature. The Fermi level shifts from the band center towards the impurity levels to reflect this. In other words, for donor impurities, the Fermi level shifts towards the conduction band, and V_{CF} decreases as the donor doping concentration increases. A similar description can be made of acceptor impurities. It is these shallow impurities that are used for doping purposes. Impurities with energies in the center of the band gap are called deep impurities. Deep impurities generally degrade device performance by reducing the carrier lifetime.

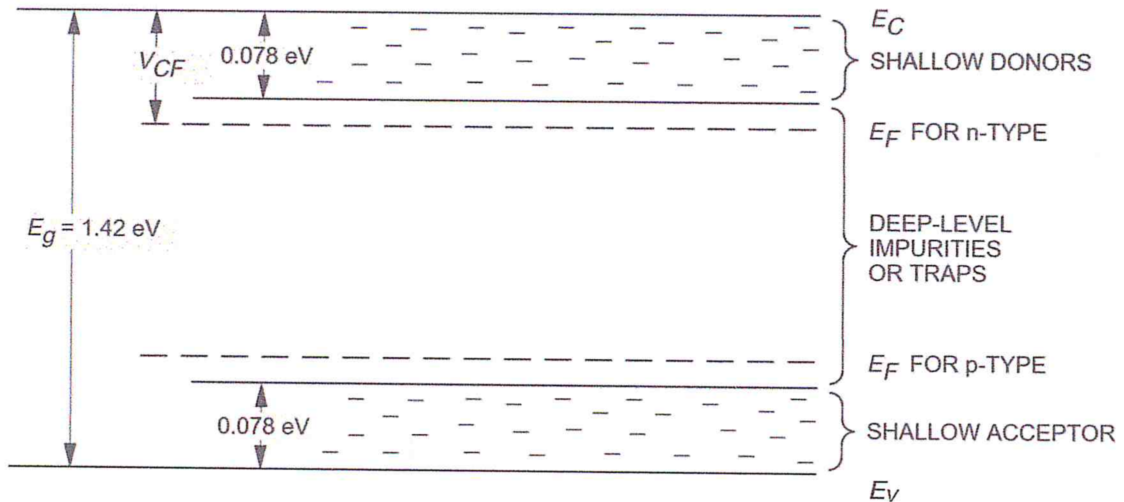

Figure 3-7: Energy band diagram for GaAs.

Both impurity types, deep and shallow, are present in GaAs in the form of complexes with gallium or arsenic. One of the most common is silicon. This group IV element can be used to give either p-type GaAs by incorporating it at low temperatures, or n-type GaAs by processing it at high temperatures. Another group IV element, carbon, is also used extensively to provide p-type GaAs. Chromium (Cr) behaves as an acceptor, with an impurity level close to the center of the energy gap. This property makes it very useful for counter doping n-type GaAs to make it semi-insulating. Other elements such as copper, oxygen, selenium, and tin are also used in GaAs processing to provide the desired n- or p-like behavior.

4.5. Thermal Characteristics

GaAs has a thermal conductivity of 0.55 W/cm-°C, which is about one-third that of silicon and one-tenth that of copper. As a consequence, the power handling capacity and therefore the packing density of a GaAs integrated circuit is limited by the thermal resistance of the substrate. The reliability of GaAs devices is directly related to the thermal characteristics of the device design, the mounting technique used for the die, and the materials used for that interface.

The thermal conductivity of GaAs is related to the temperature of the material over a wide temperature range and varies approximately as $1/T$, where T is the temperature in kelvin. However, thermal conductivity can be considered linear over a very short temperature range [39].

The power handling capabilities, reliability, and performance of semiconductor devices are directly related to the junction temperature of the device during operation. While GaAs has a higher thermal resistivity than silicon, this is somewhat offset by the higher band gap of GaAs, allowing higher operating temperatures. Nevertheless, thermal considerations are extremely important in device design, packaging, and application.

III.II GRAPHENE: THE NEXT REVOLUTION IN 2D MATERIALS

1. INTRODUCTION

Photovoltaic technology today is facing many obstacles; some of them are the limits of silicon and the conducting materials. The need for a new material is more than urgent to ensure the continuity of the technological development. To this point, **2D materials** seem to be the perfect solution for this dilemma.

2. MATERIALS THAT SHOULD NOT EXIST

More than 70 years ago, Landau and Peierls argued that strictly 2D crystals were thermodynamically unstable and could not exist [47,48]· Their theory pointed out that a divergent contribution of thermal fluctuations in low-dimensional crystal lattices should lead to such displacements of atoms that they become comparable to interatomic distances at any finite temperature [49]. The argument was later extended by Mermin [50] and is strongly supported by an omnibus of experimental observations. Indeed, the melting temperature of thin films rapidly decreases with decreasing thickness, and the films become unstable (segregate into islands or decompose) at a thickness of, typically, dozens of atomic layers [51,52]. For this reason, atomic monolayers have so far been known only as an integral part of larger 3D structures, usually grown epitaxially on top of monocrystals with matching crystal lattices [51,52]. Without such a 3D base, 2D materials were presumed not to exist, until 2004, when the common wisdom was flaunted by the experimental discovery of graphene [14] and other free-standing 2D atomic crystals (for example, single-layer boron nitride and half-layer BSCCO) [31]. These crystals could be obtained on top of non-crystalline substrates [44-46], in liquid suspension [14,53] and as suspended membranes [54].

Importantly, the 2D crystals were found not only to be continuous but to exhibit high crystal quality [14–46,53,54]. The latter is most obvious for the case of graphene, in which charge carriers can travel thousands of interatomic distances without scattering [14–46]. With the benefit of hindsight, the existence of such one-atom-thick crystals can be reconciled with theory. Indeed, it can be argued that the obtained 2D crystallites are quenched in a metastable state because they are extracted from 3D materials, whereas their small size (<<1 mm) and strong interatomic bonds ensure that thermal fluctuations cannot lead to the generation of dislocations or other crystal defects even at elevated temperature [59,60]. A complementary viewpoint is that the extracted 2D crystals become intrinsically stable by gentle crumpling in the third dimension [54,55] (for an artist's impression of the crumpling, see the cover of this issue). Such 3D warping (observed on a lateral scale of ≈10 nm) [54] leads to a gain in elastic energy but suppresses thermal vibrations (anomalously large in 2D), which above a certain temperature can minimize the total free energy [55].

3. BRIEF HISTORY OF GRAPHENE

Before reviewing the earlier work on graphene, it is useful to define what 2D crystals are. Obviously, a single atomic plane is a 2D crystal, whereas 100 layers should be considered as a thin film of a 3D material. However, how many layers are needed before the structure is regarded as 3D? For the case of graphene, the situation has recently become reasonably clear. It was shown that the electronic structure rapidly evolves with the number of layers, approaching the 3D limit of graphite at 10 layers [56]. Moreover, only graphene and, to a good approximation, its bilayer has simple electronic spectra: they are both zero-gap semiconductors (they can also be referred to as zero-overlap semimetals) with one type of electron and one type of hole. For three or more layers, the spectra become increasingly complicated: Several charge carriers appear [33,57], and the conduction and valence bands start notably overlapping [33,56]. This allows single-, double- and few- (3 to <10) layer graphene to be distinguished as three different types of 2D crystals ('graphene'). Thicker structures should be considered, to all intents and purposes, as thin films of graphite. From the experimental point of view, such a definition is also sensible. The screening length in graphite is only ≈5 Å (that is, less

than two layers in thickness) [57] and, hence, one must differentiate between the surface and the bulk even for films as thin as five layers [57,58].

Earlier attempts to isolate graphene concentrated on chemical exfoliation. To this end, bulk graphite was first intercalated [59] so that graphene planes became separated by layers of intervening atoms or molecules. This usually resulted in new 3D materials [59]. However, in certain cases, large molecules could be inserted between atomic planes, providing greater separation such that the resulting compounds could be considered as isolated graphene layers embedded in a 3D matrix. Furthermore, one can often get rid of intercalating molecules in a chemical reaction to obtain a sludge consisting of restacked and scrolled graphene sheets [60–62]. Because of its uncontrollable character, graphitic sludge has so far attracted only limited interest.

There have also been a small number of attempts to grow graphene. The same approach as generally used for the growth of carbon nanotubes so far only produced graphite films thicker than ≈100 layers [50]. On the other hand, single- and few-layer graphene have been grown epitaxially by chemical vapor deposition (CVD) of hydrocarbons on metal substrates [64,65] and by thermal decomposition of SiC (refs 66–70). Such films were studied by surface science techniques, and their quality and continuity remained unknown. Only lately, few-layer graphene obtained on SiC was characterized with respect to its electronic properties, revealing high-mobility charge carriers [68,69]. Epitaxial growth of graphene offers probably the only viable route towards electronic applications and, with so much at stake, rapid progress in this direction is expected. The approach that seems promising but has not been attempted yet is the use of the previously demonstrated epitaxy on catalytic surfaces [64,65] (such as Ni or Pt) followed by the deposition of an insulating support on top of graphene and chemical removal of the primary metallic substrate.

4. CARBON ATOM AND STRUCTURE OF GRAPHENE FROM THE CHEMICAL VIEWPOINT

The nature of chemical bonds, and the forms and shapes of structures are responsible for determining most of the properties of materials. Consequently, we have studied the electronic and optical properties of the element carbon and in

various forms and allotropes, but the most important studies relate to the two-dimensional single layer of graphite, which is known as graphene. Carbon is non-metallic and one of the best-known and most familiar materials for more than 400 years, when the British first used carbon pencils for writing. It is the sixth element of the periodic table and is the basis of all organic molecules. The electronic structure of one atom of carbon is based on 6 electrons, i.e., $1s^2$, $2s^2$, $2p^2$, where $1s^2$ represents the two electrons near the nucleus, which occupy the inner orbitals and do not contribute to chemical reactions. The four electrons ($2s^2$, $2p^2$), however, which occupy the external orbitals of the carbon atom are mixed together to contribute in three potential types of hybridization (sp, sp^2 and sp^3) in order to enhance the binding energy of the carbon structure with near neighboring atoms, forming the tight-bonded ı-bonds. The fourth electron is associated with the (π and $-\pi$) bands, as shown in Figure 3-8(a). The angles of the sp^2-hybridized orbitals are 120° like the angles of an equilateral triangle, as in Figure 3-8(b). [71-74].

Carbon is the basis of all organic molecules. Pure carbon in the form of graphite is made of single atomic layer thick crystals sp^2 of hybridized atoms, which are arranged in the two-dimensional honeycomb lattice structure of the carbon allotrope called graphene (Figure 3-8(c)) and tend to develop into other types of structure such as graphite, fullerene, and nanotubes. Graphite is thus a three-dimensional (3D) structure composed of a number of graphene layers of hexagonally structured carbon material. In graphite, the graphene layers are weakly bonded to each other due to van der Waals forces, with a distance between layers of about 3.35 Å [48]. It is graphene that represents the basic building block for the graphitic structure. The structure of the hexagonal lattice, with each hexagon defined by six carbon atoms, one in each corner, is shown in Figure 3-8(d).

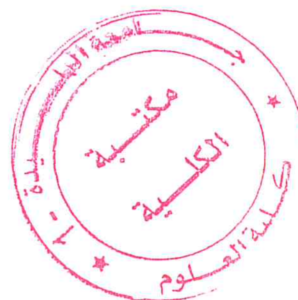

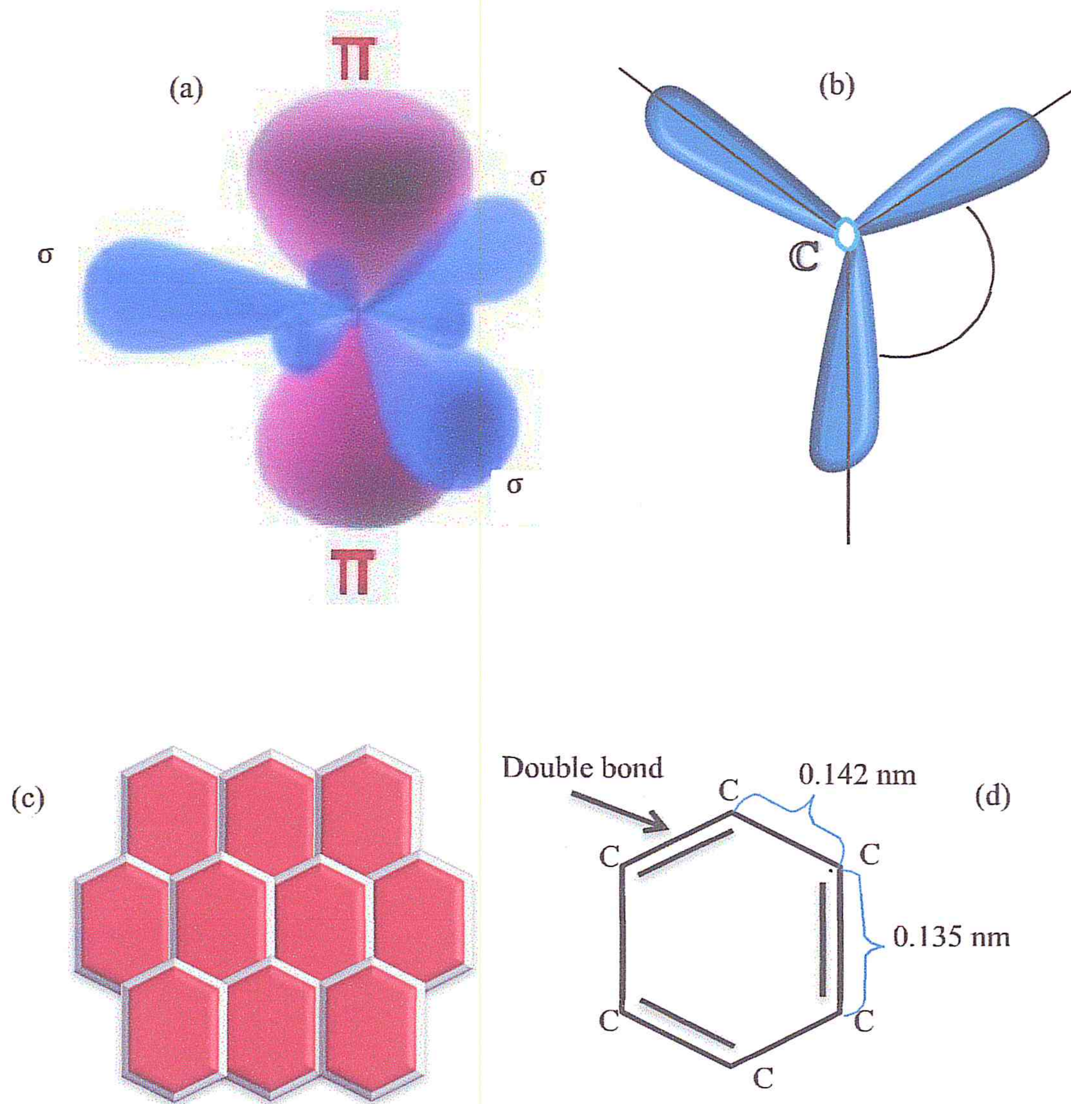

Figure 3-8: (a) Schematic representation of σ and π bonds in graphene [75]; (b) schematic view of hybridization of carbon atom; (c) graphene is a carbon allotrope with a two-dimensional honeycomb lattice structure; (d) typical hexagon from the graphene lattice surrounded by six carbon atoms with one carbon atom in each corner.

In addition, the carbon atoms are connected with each other by 6 covalent bonds: there are 3 single bonds represented as C-C, and 3 double bonds lie between them and are represented by C=C, with the distance between the atoms 0.147 nm and 0.135 nm respectively [71].

Different layers of graphene may be stacked together and held by the weak van der Waals covalent forces, to form a larger covalent structure, which is then called graphite (Figure 3-9(a)). Graphite may be a good conductor of electricity due to the vast delocalization of electrons within the weak bonds in graphite, where the delocalized electrons are free to move and are able to conduct electricity [71].

On the other hand, fullerene is another carbon allotrope; it is a zero-dimensional material, which has a similar composition to graphite but is made of hexagonal and pentagonal structures joined together (in a design that resembles a football or soccer ball (see Figure 3-9(b)). Fullerene is produced by using an electric arc between two graphite rods in a helium atmosphere to vaporize the carbon and takes the form of a hollow sphere, ellipsoid, tube or ring. Fullerene remained in hiding until the late twentieth century, unlike graphite and some other forms of carbon [73].

Carbon nanotubes (CNTs) are one of the most interesting materials due to their unique physical properties, which have attracted the attention of scientists and researchers since their discovery. They constitute a one-dimensional allotrope of carbon and, consist of graphene sheets rolled up into cylindrical tubes with Nano-scale diameters, as shown in Figure 3-9(c). The electronic properties of the nanotube depend on how the graphene sheet is rolled up [75]. Their thermal conductivity, mechanical and electrical properties, and the strength of their sp^2 carbon bonds endow CNTs with exciting mechanical, optical, and electronic properties and give them significant potential for applications [76-80].

CNTs can be "metallic or semiconducting depending on their structural" characteristics [81]. The first experiments with CNTs were conducted by using Raman spectroscopy [81,82], where "Theoretical predictions for the dependence of the transition energies on the nanotube diameter were used to narrow the possible nanotube types in the sample" [81,82]. Resonant Raman spectroscopy was also very important and useful for giving a description of the structure and electronic

properties of CNTs [81,82]. CNTs can be categorized in three structures as follows: Single-wall Nanotubes (SWNT) [84,85], Multi-wall Nanotubes (MWNT) [86], and Double-wall Nanotubes (DWNT)) [87,88].

Diamond is one of the oldest known carbon allotropes and was discovered in India at least 3000 years ago. Diamond consists of a lattice of carbon atoms in the form of a cubic structure (2-face-centred-cubic (2fcc)) of carbon atoms. The well-known diamond hardness is due to the strength of the connections between the covalent bonds in the diamond structure, which is also characterized by high thermal conductivity compared to other materials. The electronic structure of diamond is based on hybridization [89,90,71] (see Figure 3-9(d)).

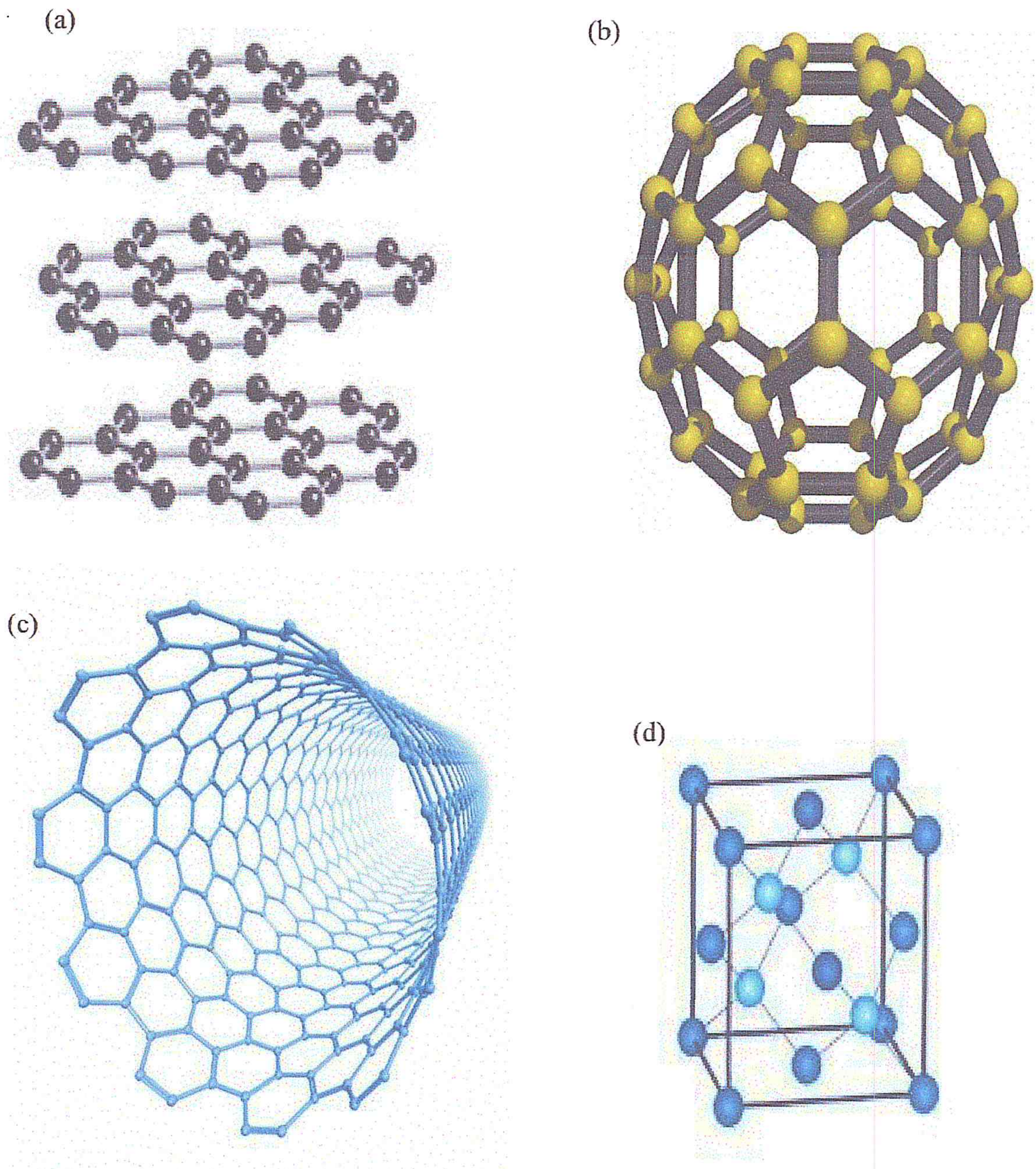

Figure 3-9: (a) Lattice structure of graphite as graphene multilayer. (b) Fullerenes (C60) are molecules consisting of wrapped graphene. (c) Carbon nanotube as a rolled-up graphene layer. (d) Unit cell of the diamond cubic crystal structure.

5. GEOMETRY OF THE BAND STRUCTURE OF GRAPHENE'S HONEYCOMB LATTICE FROM THE PHYSICAL VIEWPOINT

The graphene structure has fascinating features, which is a good reason for analyzing it and studying its optical and electronic properties. The honeycomb structure of graphene is made up of carbon atoms and takes the form of a hexagonal configuration with two sublattices (2 carbon atoms per unit cell [113,91]), which can be represented by two triangles in one lattice, as shown in Figure 3-10(a). According to this Figure, the graphene structure is not a Bravais lattice because two neighboring sites are not equivalent [98,99,120], but it is suitable to arrange a new triangular Bravais lattice with two primitive sublattice vectors (a_1 and a_2) as the A-A or B-B sublattices, (see Figure 3-10(a)), which are represented in the Cartesian x-y coordinate system as follows:

$$\vec{a_1} = \frac{a}{2}(3, \sqrt{3}) \quad \vec{a_2} = \frac{a}{2}(3, -\sqrt{3}) \tag{3.2}$$

Where ($a = 0.142\ nm$) is the carbon-carbon distance of the bond length in the graphene lattice. In addition, each point on the lattice of unit cells can be found by using the real space graphene honeycomb lattice translation vectors [93]:

$$\vec{R} = m\vec{a}_1 + n\vec{a}_2 \tag{3.3}$$

Where m and n are two integers. In addition, Figure 3-10(a) shows the reciprocal lattice with primitive unit vectors of hexagonal symmetry as

$$\vec{b}_1 = 2\pi\frac{a_2 \times a_z}{a_1.(a_2 \times a_z)} = 2\pi\left(\frac{1}{\sqrt{3}a}, \frac{1}{a}\right) \tag{3.4}$$

$$\vec{b}_2 = 2\pi\frac{a_z \times a_1}{a_1.(a_2 \times a_z)} = 2\pi\left(\frac{1}{\sqrt{3}a}, -\frac{1}{a}\right)$$

Where a_z is the unit vector in the z direction, so, there are six points in the corner of the graphene Brillion zone (see Figure 3-10(b)), which contains two groups of inequivalent points (K and K'). These are called Dirac points [113,91] and are very important for describing the physical properties associated with the graphene structure. Their positions can be expressed in this form:

$$K = \frac{2\pi}{a}\left(\frac{1}{\sqrt{3}a}, \frac{1}{a}\right) \qquad K' = \frac{2\pi}{a}\left(\frac{1}{\sqrt{3}a}, -\frac{1}{a}\right) \tag{3.5}$$

The three nearest neighbor vectors which connect the A and B sublattices (A-B), and hence the vectors δ_i for an A-sub lattice atom are given by:

$$\delta_1 = \frac{a}{2}\ (1, \sqrt{3}) \qquad \delta_2 = \frac{a}{2}\ (1, -\sqrt{3}) \qquad \delta_3 = -a\ (1, 0)$$

While the vectors δ_i' for a B-sublattice atom are the negatives of these.

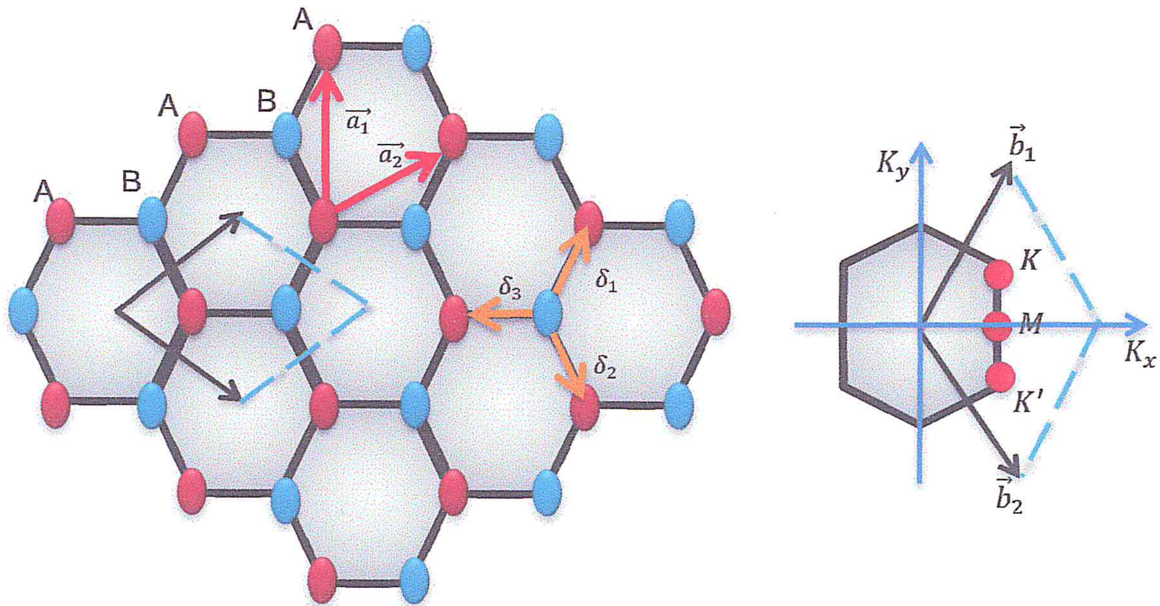

Figure 3-10: (a) Graphene honeycomb lattice structure with the two graphene sublattices, and primitive unit vectors and other unit cells as defined above. (b) Hexagonal structure of graphene with reciprocal lattice vector and the first Brillouin zone

5.1. <u>Bloch Wave Function and Tight Binding Approach</u>

The unusual band structure of carbon monolayer sheets has been calculated approximately by using one of the quantum mechanical approaches for solid material, which is the tight binding model. This model describes the electronic properties of graphene sheet between nearest neighbor carbon atoms in the honeycomb lattice and includes only the $2p_z$ state [72]. Theoretical studies based on the tight binding model have provided significant analytical results and can be combined with experimental studies, which will give good results. From 1928, Bloch succeeded in establishing the first theory to explain the electronic states in a periodic crystal lattice, which contributed to the building up of the wave functions of the

electronic band structure. The main problem in the tight-binding model, however, is to build a wave function that is in the form of a combination of Bloch's wave functions for the two sublattices (A-B sublattices), while maintaining the atomic structure [94,73]. In vibrational tight binding, the total wave function for two atoms per unit cell can defined from the Bloch wave functions by using Fourier transform analysis and can be written as:

$$\Psi_K(r) = C_A \Psi_A^K + C_B \Psi_B^K \tag{3.6}$$

Here C_A and C_B are complex function coming from the A and B sublattices, respectively, Ψ_A^K and Ψ_B^K are the wave functions on the A and B sublattices, respectively, and can be written in terms of the above-mentioned atomic wave functions as

$$\Psi_A^K(r) = \frac{1}{\sqrt{N}} \sum\nolimits_{r_A} e^{i\vec{K}.\vec{r_A}} \varphi_A(r - r_A)$$

$$\Psi_B^K(r) = \frac{1}{\sqrt{N}} \sum\nolimits_{r_B} e^{i\vec{K}.\vec{r_B}} \varphi_B(r - r_B) \tag{3.7}$$

Where N is the number of atoms in the honeycomb lattice, φ_A and φ_B are the real atomic orbitals related to the $2p_z$ orbitals in the two different atoms per unit cell, K is the quasi-momentum, and r_A and r_B identify the locations of all atoms in A and B, respectively. In addition, each sub-lattice atom in the graphene sheet is connected to three nearest neighbors, and the angles between them are 120° with respect to each other. Furthermore, to satisfy Bloch's theorem in terms of the atomic structure and to describe the electronic band structure of the graphene monolayer, the total wave function can be rewritten as follows:

$$\Psi_j^K(r + R_j) = \frac{1}{\sqrt{N}} \sum\nolimits_{r_j, R_j} e^{i\vec{K}.\vec{r_j}} \varphi_i(r + R_j - r_j) \tag{3.8}$$

Here, $j =$ the A or B sublattice, and R_j is a Bravais lattice vector. The difference between the two Bravais lattice vectors can be written in general form as follows:

$$\Psi_{j,n}^K(r + R_j) = \frac{e^{i\vec{K}.\vec{R_j}}}{\sqrt{N}} \sum\nolimits_{r_j, -R_j, n=1,\dots,ni} e^{i\vec{K}.(\overline{r_{j,n}} - R_j)} \varphi_i(r - (r_{j,n} - R_j)) = e^{i\vec{K}.\vec{R_j}} \Psi_{Aj}^K(r) \tag{3.9}$$

The band structure determining the graphene properties requires understanding and calculating the time-independent Schrödinger's equation. Therefore, the solution of this equation can be achieved by defining the Hamiltonian equation around each point of the sublattice in the honeycomb structure, which participates in three ($1s, 2s_x$ and $2p_y$) orbitals of the electronic band structure and may be written in matrix form as a two-dimensional lattice [71,72]:

$$H = \begin{pmatrix} H_{AA} & H_{AB} \\ H_{BA} & H_{BB} \end{pmatrix} = H^* \tag{3.10}$$

Where the AA and AB terms represent the integrals between the orbitals of the A atoms in the sublattice units and between the A and B sublattices, respectively, while H is the Hamiltonian equation. In the absence of the two back scattering terms, the Hamiltonian depends on two terms, H_{AA} and H_{BB} and can be rewritten in the form below:

$$H_{AA} = \langle \Psi_A^K(r) | H | \Psi_A^{K^*}(r) \rangle = E_{2p}$$

$$H_{BB} = \langle \Psi_B^K(r) | H | \Psi_B^{K^*}(r) \rangle = E_{2p}$$

Here $\Psi_{A,B}^K$ and $\Psi_{A,B}^{K*}$ include the two spinor components of the energy band. The term is the approximate energy of the 2p orbital, and $H_{AA} = H_{BB} = E_{2p}$. The solution of the overlap equation can be easily obtained from the matrix equation

$$S_k = \begin{pmatrix} \Psi_A^{K^*} & \Psi_A^K & \Psi_A^{K^*} & \Psi_B^K \\ \Psi_B^{K^*} & \Psi_A^K & \Psi_B^{K^*} & \Psi_B^K \end{pmatrix} = S_k^* \Rightarrow \begin{pmatrix} 1 & \Psi_A^{K^*} & \Psi_B^K \\ \Psi_B^{K^*} & \Psi_A^K & 1 \end{pmatrix} \tag{3.11}$$

Where

$$\Psi_A^{K^*}\Psi_A^K = \Psi_B^{K^*}\Psi_B^K = 1$$

Then, from the overlap equation and by substitution into the characteristic equation, we may obtain the eigenvalues of the Schrödinger equation, as follows:

$$det[H_k - E_k S_k] = 0. \tag{3.12}$$

E_k describes the energy dispersion of the band structure, and it has two solutions, i.e. two energy bands per unit cell as electron–hole symmetry, Therefore:

$$E_k^{\pm} = E_{2p} \pm \sqrt{H_{AB}(k)\, H_{AB}^*(k)} \tag{3.13}$$

$$E_k = \pm\gamma_0\sqrt{1 + 4\cos\left(\frac{3}{2}k_x a\right)\cos\left(\frac{\sqrt{3}}{2}k_y a\right) + 4\cos^2\left(\frac{3}{2}k_x a\right)} \tag{3.14}$$

Where k_x and k_y are the components of the wave vector k at the corner of the Brillion zone, and $3\gamma \approx 3\ eV$ is the nearest neighbor hopping energy of the graphene honeycomb. The signs + and - indicate the highest energy state within the valence band and the lowest energy state within the conduction band, respectively. Figure 3-11(a) shows the electronic disposition and energy bands of the graphene monolayer sheet in 3D, and Figure 3-11(b) shows a section of the energy band in 2D, which is connected in two Dirac points, and all characteristic lines ($K \rightarrow \Gamma \rightarrow M \rightarrow K$).

Finally, to calculate the two components of the spinor wave function of the Hamiltonian for monolayer graphene, and solve the Eigen functions around the corner of the Brillouin zone (Dirac point), we can use the Schrödinger equation $H_k \Psi_A^K(r) = E_k \Psi_A^K(r)$, which may be rewritten in matrix form by substituting the Hamiltonian equation and energy band structure in the graphene lattice as mentioned above, with multiplication of the Schrödinger equation by Ψ_A^{K*}. The result can be written as follows:

$$\Psi_A^{K*}(r) H_k \Psi_A^K(r) = \Psi_A^{K*}(r) E_k \Psi_A^K(r) \tag{3.15}$$

Then, the total wave function of the two atoms per unit cell, as shown in Figure 3-10(a), can be rewritten as

$$\Psi_k(r) = \alpha_k \Psi_A^K(r) + \beta_k \Psi_A^K(r) \tag{3.16}$$

Where α_k and β_k are the two complex spinor components of the quasi-momentum. Both of them are factors in the Bloch function as in the form below

$$\Psi_k(r) = \sum_{m=1}^{n} e^{i\vec{k}.\vec{r}_j} \begin{pmatrix} \alpha_k \\ \beta_k \end{pmatrix} \tag{3.17}$$

Finally, the Schrödinger equation for monolayer graphene, which includes all the electronic characteristics and describes the electronic transitions in the honeycomb structure, can be written in the following form:

$$(\alpha_k^* \quad \beta_k^*)\, H_k \begin{pmatrix} \alpha_k \\ \beta_k \end{pmatrix} = E_k (\alpha_k^* \quad \beta_k^*) \begin{pmatrix} \alpha_k \\ \beta_k \end{pmatrix} \tag{3.18}$$

The first significant feature of this equation, which describes all photon processes between the two energy bands (the valence and conduction bands) and around each Dirac point in the monolayer graphene lattice, is that it also describes the electronic transitions and important structure of this two-dimensional allotrope of carbon. This equation gives good results in many cases and may be compared with other results, such as experimental results or results from another theoretical model. Also, the use of new methods in the various branches of quantum mechanics can achieve substantial convergence with the results that have been presented and thus allow access to new theories to explain the electronic and optical properties, such as the ab- initio model. Therefore, the realization and control of the unique properties of graphene material can open up new horizons in the field of optoelectronic devices.

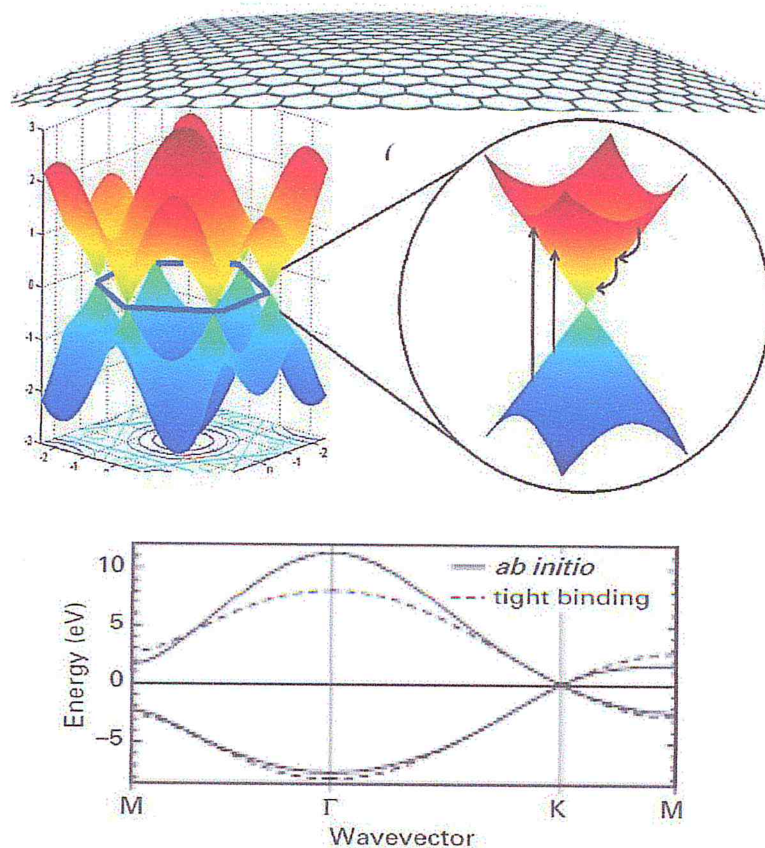

Figure 3-11: Energy dispersion in the honeycomb graphene lattice. (a) Left, the energy bands of a graphene monolayer sheet in 3D. Right, the energy dispersion of graphene at the K-point, which is known as the Dirac cone. (b) Comparison of ab-initio model and tight banding model of graphene, showing good agreement at low energies [94].

5.2. Single Layer Graphene

Graphene is a single-atomic-layer, two-dimensional system composed solely of carbon atoms arranged in a hexagonal honeycomb lattice. It can be considered as the basic building unit for other forms of carbon materials. Electronically, single layer pure graphene is a zero band-gap semiconductor with two energy bands, the conduction and valence bands, which meet at the Dirac point, as shown in Figure 3-10 (a) (left). Only a brief account of the structure of the graphene monolayer will be given here, because much of this has been already covered in detail, where the energy band dispersion and wave function have been calculated by using a branch of quantum mechanics, the tight-binding model, and also in terms of Bloch's theory in order to satisfy the theoretical details. The energy dispersion approximation near the k and k' points in graphene single layer can be rewritten as

$$E_k = \pm \hbar v_f |K| \tag{3.19}$$

Where $v_f = 3\gamma_0\, a/2\,\hbar \cong 10^6\ m.s^{-1}$ is the Fermi velocity, and $\gamma_0 = 3\ eV$ is the hopping parameter. This energy around the k and k' points takes the shape of two cones, where the one in the upper half of the dispersion is the conduction (π^*) band and the other one in the lower half is the valence (π) band, with the two dispersions touching each other at the zero-energy point (Dirac point). Such an arrangement is called a Dirac cone (see Figure 3-11(a)). For the case of zero carrier density, the point where the two bands cross the Fermi level coincides with the zero energy at the K and K′ points of the first Brillouin zone, whose wave vectors are given by

$K = (4\pi/\sqrt{3}\,a)(1/\sqrt{3}, 1)$ and $K = (4\pi/\sqrt{3}\,a)(3/2\sqrt{3}, -1/2)$ [95].

The effective low energy Dirac Hamiltonian equation of two-dimensional single layer graphene describes the charge carriers close to the Dirac point and also can be written as a 2 × 2 square matrix, taking into account the relative Weyl fermion equation, as follows:

$$H = \hbar v_f \begin{pmatrix} 0 & k_x + ik_y \\ k_x - ik_y & 0 \end{pmatrix} = \hbar v_f \hat{\sigma}.K \tag{3.20}$$

Then, the Schrödinger equation can be revised in quite reasonable form by using the Hamiltonian equation as above for spinless graphene carriers around the Dirac point, which can be defined by

$$-\hbar v_f \sigma . \nabla \Psi = E\, \Psi \qquad \text{(near K point)}$$

$$-\hbar v_f \sigma^* . \nabla \Psi' = E\, \Psi' \qquad \text{(near K' point)}$$

Here, ∇ is the gradient with respect to the position (r), and $\hat{\sigma}$ is the operator of the general Pauli matrices on the spinor $\Psi_K = (\Psi_A, \Psi_B)$, which is expanded into two dimensions, those of the x and y axes, and is given as

$$\hat{\sigma} = (\sigma_x, \sigma_y) \;,\quad \hat{\sigma}^* = (\sigma_x^*, -\sigma_y^*)$$

$$\sigma_x = \begin{pmatrix} 0 & 1 \\ 1 & 0 \end{pmatrix} \;,\quad \sigma_y = \begin{pmatrix} 0 & -i \\ i & 0 \end{pmatrix} \;,\quad \sigma_z = \begin{pmatrix} 1 & 0 \\ 0 & -1 \end{pmatrix} \qquad (3.21)$$

From these procedures, we reach the well-known Schrödinger equation of single layer graphene, which will be reduced to the general form by modelling the previously mentioned relations with the Dirac Hamiltonian equation around the K point in the low energy system. Note that the particles behave as massless only around this point, and the result therefore will be

$$\hbar v_f \begin{pmatrix} 0 & k_x + ik_y \\ k_x - ik_y & 0 \end{pmatrix} \begin{pmatrix} \alpha_k \\ \beta_k \end{pmatrix} = E_k \begin{pmatrix} \alpha_k \\ \beta_k \end{pmatrix}$$

This equation involves the two component spinors and describes a particle with finite mass in the graphene lattice. It thus can be easily solved to yield the eigenvalues and eigenfunctions, which are given by

$$E_k = \pm \hbar v_f \sqrt{k_x^2 + k_y^2}$$

$$\Psi_k(K) = \frac{1}{\sqrt{2}} \begin{pmatrix} e^{-i\theta_k/2} \\ \lambda e^{i\theta_k/2} \end{pmatrix} \qquad \text{where} \quad H_k = \hbar v_f \sigma . K$$

$$\Psi_{k'}(K) = \frac{1}{\sqrt{2}} \begin{pmatrix} e^{i\theta_k/2} \\ \lambda e^{-i\theta_k/2} \end{pmatrix} \qquad \text{where} \quad H_{k'} = \hbar v_f \sigma^* . K \qquad (3.22)$$

Here, $\lambda = 1\ (-1)$ indicates the K and K' valley, respectively, and $\theta_k = \arctan(k_y/k_x)$ is defined by the direction of the wave vector in k space [113,100,119,122]. The rotation of K in both the k_x and the k_y planes by 2π, will result in a change in phase by π, with the new phase called a Berry's phase. That change in phase by π is one feature that describes the two spinors of the wave function.

5.2.1. Electronic structure of gapped single layer graphene

All the above discussion describes the electronic structure of single layer graphene under gapless (zero band-gap) conditions, so it is important to address another form of the energy bands, that is, a gap between the energy bands at the Dirac point. The arrangement of the two sub-lattices of carbon atoms is responsible for the zero energy between the bands. Consequently, a breaking of the symmetry between the A and B sub-lattices at the Dirac point would cause a gap to open up [96]. Furthermore, the possible ways to break the symmetry and to open up the gap include, for example, strain engineering [97, 98], graphene-substrate interaction [99,100], confinement [101], and chemical modification of graphene [102]. The absence of the energy gap in graphene blocks the development of many optical and electronic applications.

Therefore, we will follow the same steps as in the gapless case to calculate the eigenvalues and eigenfunctions with a band gap, and then the Hamiltonian equation around the k point at low energy can be written in the form below:

$$H = \hbar v_f \begin{pmatrix} \frac{\Delta_\varepsilon}{2} & k_x + ik_y \\ k_x - ik_y & -\frac{\Delta_\varepsilon}{2} \end{pmatrix} \tag{3.23}$$

Here, Δ_ε and $-\Delta_\varepsilon$ represent the energy bands at the Dirac point.

The eigenvalue is given by substituting the Hamiltonian equation for the energy gap condition into the characteristic equation as follows:

$$E_{k,\Delta} = \mp\sqrt{(\Delta_\varepsilon)^2 + v_f^2|k|^2} = \pm\sqrt{(\Delta_\varepsilon)^2 + v_f^2(k_x^2 + k_y^2)} \tag{3.24}$$

The equation above describes the energy spectrum around the K point below the band gap. In addition, with an energy gap in single layer graphene, there is the clear fact that the charge carrier has a finite mass, so that the behavior of this energy equation is not linear in the low energy regime. But on the other hand, the behavior of the electrons cannot be obtained without destroying the linear behavior and breaking the symmetry of the graphene single layer structure [103]. In addition, the wave function for two compound spinors in this system can be calculated by substituting the Hamiltonian matrix as above into the Schrödinger equation and is given as follows [96]:

$$\Psi_k(\Delta) = \frac{1}{\sqrt{2}} \begin{pmatrix} e^{i(k_x - k_y)} \\ \lambda \sqrt{\frac{|E_{k,\Delta}| - \lambda\Delta}{|E_{k,\Delta}| - \lambda\Delta}} e^{i\theta} e^{i(k_x - k_y)} \end{pmatrix} \tag{3.25}$$

The density of states for gapped graphene can be defined by

$$D_\varepsilon = \frac{g_v g_s |E_{k,\Delta}|}{2\pi\hbar v^2} \theta(|E_{k,\Delta}| - \Delta) \tag{3.26}$$

Where $g_s = 2$ and $g_V = 2$ are the degrees of freedom associated with the spin and the valley, respectively, and θ is a step function [103, 104]. Finally, to control the semiconducting properties and tune the Fermi level of graphene, we can use doping, chemical modification, and electrostatic field tuning [105].

5.2.2. Experimental work of single layer graphene

The discussion above is concerned with the theoretical expression of the graphene structure in two forms, with and without a band gap. Therefore, it is worthwhile to compare the theoretical results with the experimental results to achieve a comprehensive understanding of the electronic structure of the honeycomb lattice of carbon atoms in 2D. Therefore, in this section we will address briefly the most important experimental studies under the framework of this topic. Since the isolation of single layers of graphite in 2004 [106], several exciting experimental studies on single layer graphene have been conducted. In addition, a number of efforts were combined from 1990 to 2004 to attempt fabrication of thin films of graphite. Unfortunately, these attempts did not succeed, however, except in obtaining films several tens of layers thick, amounting to about 50 to 100 layers until 2004, when a group of scientists succeeded (the first experimental establishment) in the fabrication of single-atom-thick two-dimensional graphene crystalline material [107] (as shown in Figure 3-12(a-d)). After that, these isolated samples were taken and placed over a thin layer of SiO_2 on a silicon wafer. The layer of Si under the SiO_2 was used as a "back gate" electrode to change the charge density in the honeycomb lattice over a wide range [108]. The first observation of the unique properties of graphene by using the micromechanical cleavage technique was of the Anomalous Quantum Hall Effect. That validated the theoretical results and predicted a π-shifted Berry's phase of massless Dirac fermions in graphene [109]. Recently, monolayer graphene films have been achieved by chemical vapour deposition on a thin substrate of nickel layers and silicon wafer covered by a layer

of silicon oxide. In addition, this offered different methods of modelling the films for the synthesis of large-scale graphene films [110,111], which have provided a clear explanation of the typical Quantum Hall Effect for single layer graphene. As has proved important, using monolayer graphene films is better than multilayered due to their higher trans-conductance and optical transparency [111,112]. "Hence, epitaxial graphene reproduces the unique features observed in exfoliated graphene, but is certainly a system which allows for more systematic development of graphene devices, with rich perspectives for science and technology" [112].

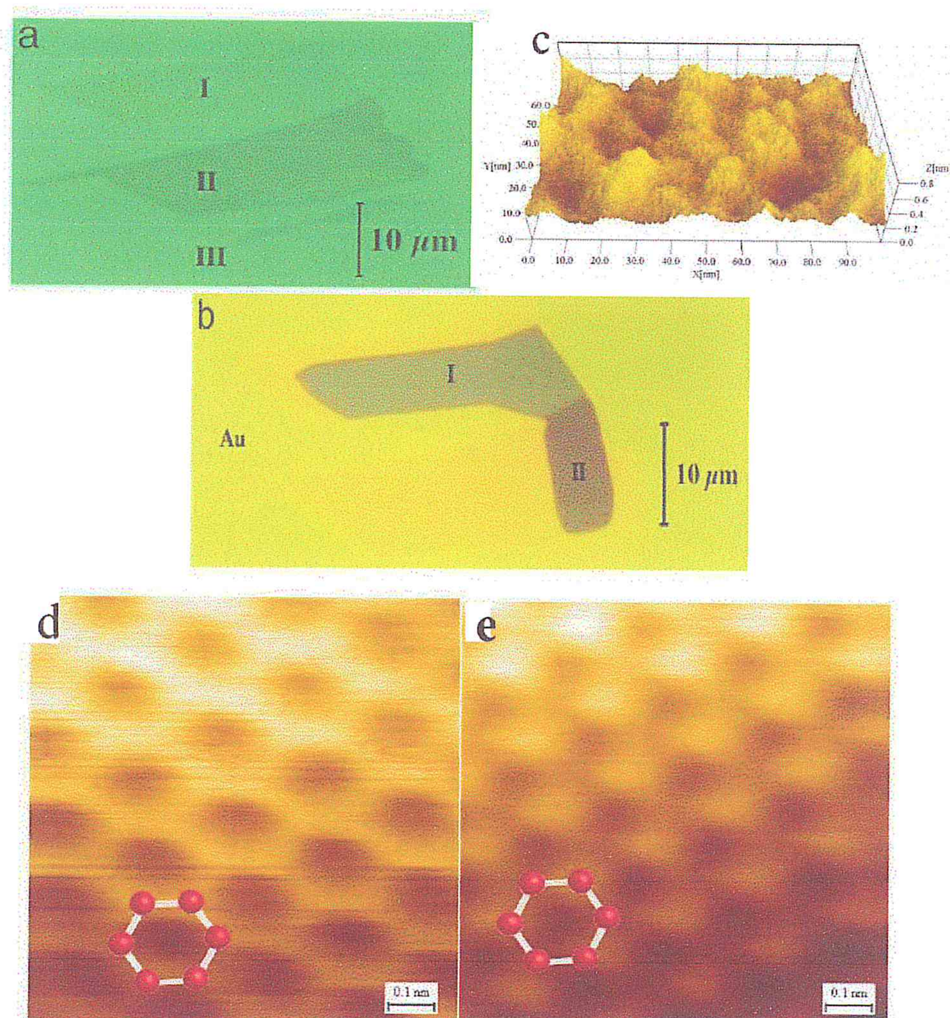

Figure 3-12: Optical microscope image of a graphene flake: (a) Three regions can be identified: I. single-layer graphene; II. Multilayer graphene and III. The silicon-dioxide-coated substrate. (b) Image of the same flake after the deposition of an 18-nm layer of gold. (c) STM image of a single-layer graphene film on the silicon dioxide surface. (d) The full hexagonal symmetry expected of an isolated single layer graphene sheet. (e) Image of the multilayer portion of the sample [108].

5.2.3. Single layer graphene Nano-ribbons

Understanding the electronic structure of the graphene honeycomb requires a microscopic view to fully elucidate the structure of the $2sp$ carbon constituents. Their electronic structure actually remained unknown for a long time until K. Nakada et al. was able to provide a study of nanometer-scale graphite networks by using the model of graphene ribbons with various edge shapes, which also provided mathematical details on the features of the states at the edge and the localized states close to the Fermi level in the honeycomb structure with zigzag and armchair edge functions [114]. Hence, studying graphene nanoribbons and their surface (edges) is a very significant and plays an effective role in determining the characteristics of graphene. There are two types of edges that represent the final borders, or semifinal in the graphene sheet, and these are the ZIGZAG and ARMCHAIR edges as shown in Figure 3-13(a, b).

The nature of the edges in the graphene sheet is responsible for the spectrum and the structural axis of graphene sheets. As shown in Figure 3-13 (a), the zigzag edges are represented along the x-axis, whereas the armchair edges are represented along the y- axis. The nanoribbons of graphene can be described by narrow rectangles made from the honeycomb structure, which have widths up to 10 nanometers, and are therefore classified under the category of nanoscale materials. These can possess the characteristics of a semiconductor, which gives us an opportunity to study their optical and electronic properties due to the significant changes in these properties from quantization. Theoretically, the calculations of the general band structure of the graphene nanoribbons (GNR) are obtained from the Hamiltonian equation by using wave mechanics based on the tight-binding model or some other method [115].

"The energy band structures of armchair nanoribbons can be obtained by making the transverse wavenumber discrete, in accordance with the edge boundary condition, as in the case of carbon nanotubes. However, zigzag nanoribbons are not analogous to carbon nanotubes, because in zigzag nanoribbons, the transverse wavenumber depends not only on the ribbon width, but also on the longitudinal wavenumber." [116].

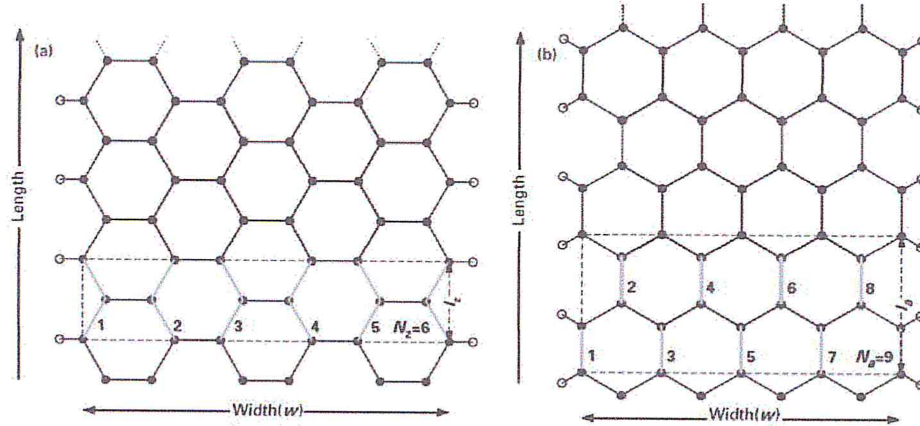

Figure 3-13: The finite-width honeycomb structure of graphene nanoribbons: (a) zigzag edge of graphene nanoribbons; (b) armchair edge of graphene nanoribbons.

The Dirac Hamiltonian equation of the GNR band structure around the K and K' points is calculated as described previously for the general band structure of the graphene honeycomb. The spinor wave function of GNR can obtained, however, by assuming that the edge of the graphene sheet is parallel to the x direction as in a zigzag nanoribbon (see Figure 3-13(a)) and to the y direction as in an armchair nanoribbon (see Fig. 1.6(b)), which can be expressed by

$$\Psi_{k(zig)}(K) = e^{ik_x x}\begin{pmatrix}\phi_A(y)\\ \phi_x(y)\end{pmatrix} \qquad \text{zigzag nanoribbons}$$

$$\Psi_{k(arm)}(K) = e^{ik_y y}\begin{pmatrix}\phi_A(x)\\ \phi_x(x)\end{pmatrix} \qquad \text{armchair nanoribbons}$$

The boundary condition of the GNR at the zigzag edge and armchair edge can be provided as follows:

$$\Psi_{(A,B)}(y = L) = 0 \ , \ \Psi_{(A,B)}(y = 0) = 0$$

$$\Psi_{(A,B)}(x = L) = 0 \ , \ \Psi_{(A,B)}(x = L) = 0$$

$$\phi_{(A,B)}(L) = 0 \ , \ \phi'_{(A,B)}(L) = 0$$

Here, L is the ribbon width. Under these conditions, and to satisfy the Bloch theorem, the two-compound spinor wave function can be rewritten from the envelope function as follows:

$$0 = e^{iKx}e^{ik_x x}\phi_A(L) + e^{-iKx}e^{ik_x x}\phi'_A(L) \qquad \text{zigzag}$$

$$0 = e^{iKx}e^{ik_x x}\phi_B(L) + e^{-iKx}e^{ik_x x}\phi'_B(L) \qquad \text{zigzag}$$

$$0 = e^{ik_y y}\phi_{A,B}(0) + e^{ik_y y}\phi'_{A,B}(0) \qquad \text{armchair}$$

$$0 = e^{iKL}e^{ik_y y}\phi_B(L) + e^{-iKL}e^{ik_y y}\phi'_B(L) \qquad \text{armchair}$$

Then, by following a similar method to that used to calculate the eigenvalues, the eigenfunctions and the band structure of general pure graphene can be found by using the Schrödinger equation [113,91]. The energy dispersion spectrum for armchair and zigzag nanoribbons is given respectively by [116]:

$$E_k(aGNR) = \lambda\sqrt{1 + 2(2\cos(p))\cos\left(\frac{k}{2}\right) + (2\cos(p))^2}$$

$$E_k(zGNR) = \lambda\sqrt{1 + \left(2\cos\left(\frac{k}{2}\right)\right)^2 + 4\cos\left(\frac{k}{2}\right)\cos(p)} \qquad (3.27)$$

The energy gap plays an important role, which is related to the width of the edge of the graphene ribbon, where the energy gap for zigzag ribbons (at $= 0$) and the energy gap for armchair ribbons (at $k = 2\pi/3$) increases as a result of a decrease in the width of the graphene ribbons [116]. The great challenge, however, remains control of the energy gap. Finally, to achieve a really good description of the graphene nanoribbon, it is necessary to know the number of armchair (a) and zigzag (z) chains that are present in the length and width directions, as shown in Figure 3-13(a, b), which shows "how to count the number of chains for a 9-aGNR and a 6-zGNR. The width of the GNRs can be expressed in terms of the number of lateral chains" [94]:

$$aGNR, \omega = \frac{N_a - 1}{2}a$$

$$zGNR, \omega = \frac{3N_z - 2}{2\sqrt{3}}a \qquad (3.28)$$

Here $a = 2.46$ Å is the lattice constant of the honeycomb lattice. The lengths of the primitive unit cells are $l_a = \sqrt{3}a$ and $l_a = a$ for armchair and zigzag nanoribbons, respectively. Numerical calculations are used to calculate the band structure of the graphene nanoribbons and are based on the first principles of the

intrinsic graphene and the tight binding approximation, which is described in the previous section. All these features mentioned above may lead to the development of electronic devices.

5.3. Bilayer Graphene

The isolation of individual graphene flakes in 2D by using mechanical exfoliation was one of the biggest events in the world of modern physics. Hence, a comprehensive review has been provided in the above sections of studies of monolayer graphene, which has been the subject of great attention and attracted scientists to study its unique characteristics. Here, we will review a brief study of two stacked layers of graphene, called bilayer graphene, which is believed to exhibit more important features than the single layer due to the Anomalous Integral Quantum Hall Effect (IQHE) [117,118,119], and also provides a greater opportunity to open a tunable gap between the band energies [120,121,122,123,124] and to examine the trigonal warping phenomenon [125,126].

The tight-binding model for graphite can be easily be extended to bilayer graphene by using the theoretical study of single layer graphene and developing the Hamiltonian equation to involve the electronic transitions between the two layers, which is needed to understand the binding energy for both layers. Taking into account the four atoms per unit cell, there are two sublattices A and B for each layer, as shown in Figure 3-14(a, b). The Hamiltonian equation for the nearest neighbors labeled as $j = A1, B1, A2, B2,$ under low energy and around the k point, can be obtained by

$$H(k) = \begin{pmatrix} \epsilon_{A1} & -\gamma_0 f(k) & \gamma_4 f(k) & -\gamma_3 f^*(k) \\ -\gamma_0 f^*(k) & \epsilon_{B1} & \gamma_1 & \gamma_4 f(k) \\ \gamma_4 f^*(k) & \gamma_1 & \epsilon_{A2} & -\gamma_0 f(k) \\ -\gamma_3 f(k) & \gamma_4 f^*(k) & -\gamma_0 f^*(k) & \epsilon_{B2} \end{pmatrix} \quad (3.29)$$

Where $\gamma_0, \gamma_1, \gamma_3, \gamma_4$ are the parameters of plane hopping between the two layers and can be defined by [127]

$$\gamma_0 = -\langle \emptyset_{A1} | H | \emptyset_{B1} \rangle = -\langle \emptyset_{A2} | H | \emptyset_{B2} \rangle$$

$$\gamma_1 = \langle \emptyset_{A2} | H | \emptyset_{B1} \rangle$$

$$\gamma_3 = -\langle \emptyset_{A1}|H|\emptyset_{B2}\rangle$$

$$\gamma_4 = \langle \emptyset_{A1}|H|\emptyset_{A2}\rangle = \langle \emptyset_{B1}|H|\emptyset_{B2}\rangle$$

The function $f(k)$ represent nearest-neighbor hopping and is written as follows:

$$f(k) = e^{ik_y a/\sqrt{3}} + e^{ik_y a/\sqrt{3}} \cos(k_x a/2). \quad (3.30)$$

The Hamiltonian matrix presented above can be described accurately by splitting it into four regions; the upper-right and lower-left 2 × 2 squares represent the interlayer coupling. Factor is the coupling between orbitals on sites B1 and A2, and factor γ_4 is the interlayer coupling between orbitals A1 and B2. Factor is the interlayer coupling between orbitals A1 and A2 or B1 and B2. On the other hand, the upper-left and lower-right 2 × 2 squares represent the intralayer coupling and also represent a description of the transitions that occur in the monolayer. In addition, the parameters $\epsilon_{A1}, \epsilon_{B1}, \epsilon_{A2}$ and ϵ_{B2} describe the energies of bilayer graphene on sites A1 and A2 or B1 and B2 respectively. Here, the factor $\gamma_0 = 3.033\ eV$ represents the nearest-neighbor hopping energy within a single layer [127,128] and $\gamma_0 f(k) = v(ik_x - k_y)$ where $v = 3\gamma_0 a/2$ is the velocity.

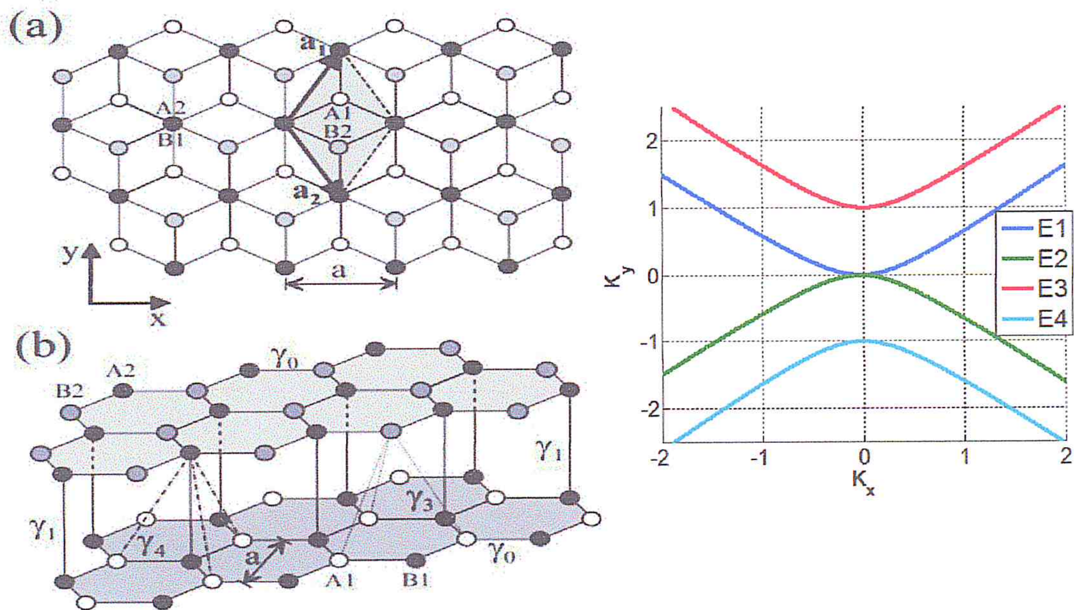

Figure 3-14: (a) Schematic diagram of lattice structure of bilayer graphene in (a) a plane and (b) a side view of the crystal structure [127]. (c) Schematic of low energy bands around K points.

The overlap integral equation for bilayer graphene can be written in matrix form:

$$S(k) = \begin{pmatrix} 1 & s_0 f(k) & 0 & 0 \\ s_0 f^*(k) & 1 & s_1 & 0 \\ 0 & s_1 & 1 & s_0 f(k) \\ 0 & 0 & s_0 f^*(k) & 1 \end{pmatrix} \quad (3.31)$$

This equation mirrors $H(k)$. Where $s_0 = \langle \emptyset_{A1} | \emptyset_{B1} \rangle = \langle \emptyset_{A2} | \emptyset_{B2} \rangle$, describing the orthogonally of orbitals on sites A1 and B1 or A2 and B2.

Also $s_1 = \langle \emptyset_{A1} | \emptyset_{B1} \rangle = \langle \emptyset_{A2} | \emptyset_{B2} \rangle$, describing the orthogonality of orbitals on sites A1 and B2 or A2 and B1.

From the Hamiltonian equation, four energy bands can be obtained, as shown in Figure 3-14(c) and substituted into the characteristic equation as follows [127]:

$$\epsilon_{A1} = 1/2(-U + \eta_{AB}) \qquad \epsilon_{B1} = 1/2(-U + \eta_{AB})$$

$$\epsilon_{A2} = 1/2(U + 2\Delta' + \eta_{AB}) \qquad \epsilon_{B2} = 1/2(-U + \eta_{AB})$$

Where $U = \frac{1}{2}[(\epsilon_{A1} - \epsilon_{B1}) - (\epsilon_{A2} + \epsilon_{B2})], \Omega = \frac{1}{2}[(\epsilon_{B1} - \epsilon_{A2}) - (\epsilon_{A1} + \epsilon_{B2})]$,

and $\eta = \frac{1}{2}[(\epsilon_{A1} - \epsilon_{A2}) - (\epsilon_{B1} + \epsilon_{B2})]$.

Under the tight-binding model, the Bloch function of the bilayer graphene wave function can be obtained by substituting into the Schrödinger equation to obtain the four solutions of the wave function, as [129]:

$$\Psi_{A1} = \frac{1}{\sqrt{N}} \sum_j \exp(ik.a_j) \Psi_0(a_j - r)$$

$$\Psi_{B1} = \frac{1}{\sqrt{N}} \sum_j \exp(ik.a_j) \Psi_0(a_j + a - r)$$

$$\Psi_{A2} = \frac{1}{\sqrt{N}} \sum_j \exp(ik.a_j) \Psi_0(a_j + a - r)$$

$$\Psi_{B2} = \frac{1}{\sqrt{N}} \sum_j \exp(ik.a_j) \Psi_0(a_j + c + a - r)$$

Here, a_j is the lattice vector, N is the number of unit cells, and the vectors a and c represent the links between the nearest atoms in the same layer and the nearest atoms in the neighbouring layer, respectively. Basically, electrons in bilayers behave qualitatively differently than in single layers. The low energy bilayer graphene (BLG) exists in different forms, depending on the coupling terms between the layers, so it is important to know the nature of the coupling to determine the form of the electronic band structure and move forward to calculate the eigenvalues, the eigenfunctions, and the energy band structure.

Chapter IV

SILVACO ATLAS (TCAD) Simulation and Results

IV.I. SILVACO ATLAS (TCAD) SIMULATION TOOL

1. INTRODUCTION

In our work, we used technological simulation software **SILVACO (TCAD)**, to simulate the electrical and optical characteristics of a **Schottky junction Graphene/GaAs (SM/SC) solar cell**. First, we should learn some basic notions about simulation in general and this software and particularly using examples illustrating the work, and then we would proceed to our simulation and discuss the results that we obtained from our work.

The Role of Simulation

The simulation offers a link between the experimental world and the theoretical one, as it complements theory and experiment and builds physical reality in the presence of certain constraints or the presence of an impossible mathematical analysis.

2. A BRIEF HISTORY ABOUT SILVACO

SILVACO (Silicon Valley Corporation) is an American company, headquartered in Santa Clara, California. It is a leading provider of professional chains of finite element simulation and computer-aided design software for the Technology Computer Aided Design (TCAD) technology. These tools are used by microelectronics companies in the field of research, development and design of devices

Historically the company was founded in **1984** by **Dr. Ivan Pesic** to meet the needs of integrated **IC** designers for increasingly accurate and linear Simulated Programming with Integrated Circuit Emphasis (SPICE) models.

The entry of **SILVACO** into **TCAD** technology took place in **1989,** and was based on a research of the Department of Physical Devices of Stanford University, thus appear in **SILVACO "Athena"** as process simulator and **"Atlas"** As a simulator of the devices (2D and 3D).

SILVACO has not been designed to meet a single semiconductor component. By including more general models of semiconductor physics, it allows for more extensive simulations by scanning a whole range of electronic components.

3. SILVACO (TCAD) SOFTWARE

The VWF: (virtual wafer Fab):

Among the various software that it forms the VWF are the two most famous used ATHENA and ATLAS, these tools are divided into two main categories.

- **Main Tools** and **Auxiliary tools**

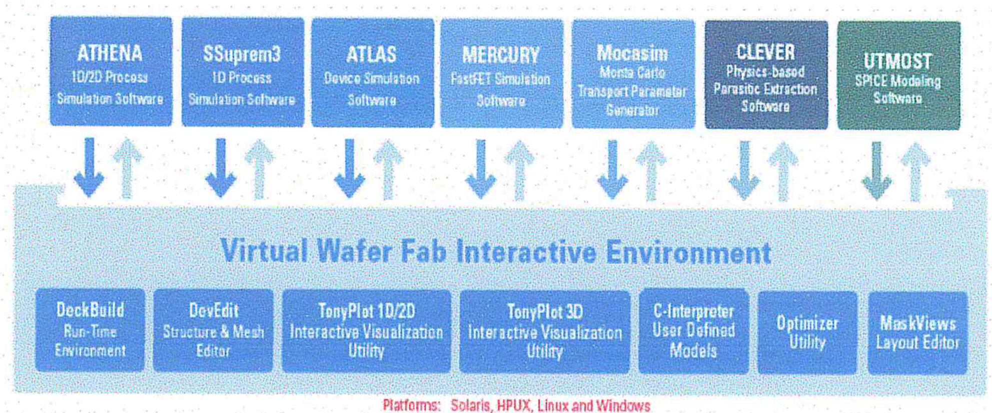

Figure 4-1: The Virtual Wafer Fabrication [138]

ATLAS is an electronic simulator capable of predicting the electrical characteristics of most semiconductor components in continuous, transient or frequency regime. In addition to the "external" electrical behavior, it provides information on the internal distribution of variables such as carrier concentrations, electric field or potential, etc., all important data for the design and optimization of technological processes.

This is accomplished by numerically solving the Poisson's equation and the continuity equations of the two-dimensional electrons and holes in a finite number of points forming the mesh of the structure defined by the user or by another program.

ATLAS has been designed so that it can be used with other tools that facilitate or supplement its use.

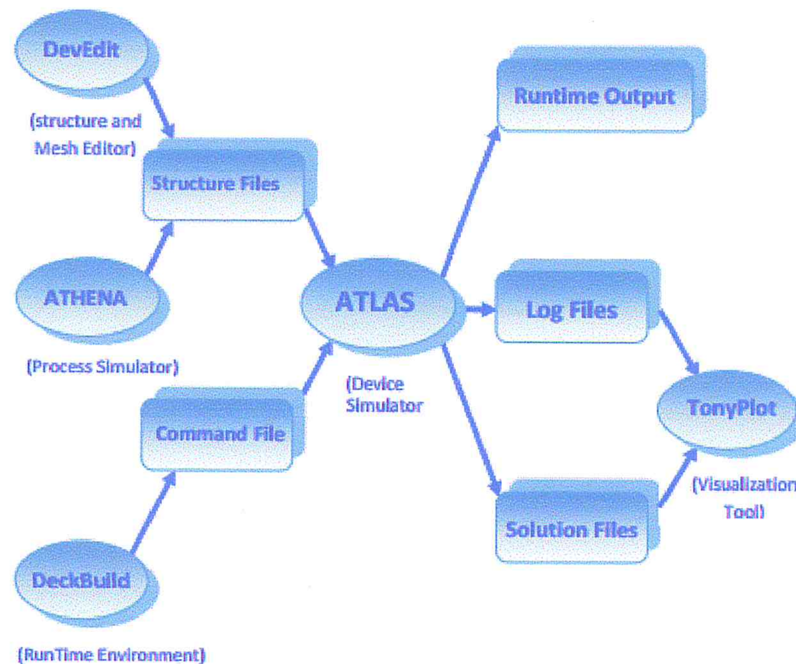

Figure 4-2: Inputs and outputs of Atlas [138].

4. ATLAS ENVIRONMENT

ATLAS is an electronic simulator capable of predicting the electrical characteristics of most semiconductor components in continuous, transient or frequency regime. In addition to the "external" electrical behavior, it provides information on the internal distribution of variables such as carrier concentrations, electric field or potential, etc., all important data for the design and optimization of technological processes.

This is accomplished by numerically solving the Poisson's equation and the continuity equations of the two-dimensional electrons and holes in a finite number of points forming the mesh of the structure defined by the user or by another program.

This simulator consists of two parts:

- A Digital Processing Part (method of integration, discretization ...),
- A part formed of the physical models of the most recent semiconductor components: models of recombination, impact ionization, mobilities, temperature and statistics of Fermi-Dirac and Boltzmann in particular.

The diagram in Figure 4.2 shows the different types of information that circulate at "**Atlas**" inputs and outputs. Most simulations carried out under "Atlas" use two input files. The first file is a text file containing commands for "**Atlas**" to run (represented by "Command File"). The second file is a "structure file" containing the structure of the device to be simulated defined in "**Athena**" or "**DevEdit**".

At the "Atlas" output, we have three types of files. The first of these files is the "**Runtime**" output, which gives progress, errors and warning messages during the simulation. The second type of file is the "**log**" file, which stores all voltage values and currents from the analysis of the simulated device (this is the file of the electrical behavior). The third output file is the "**Solution File**", this file stores the 2D or 3D data concerning the values of the solutions variables at a given point of the device.

ATHENA is a simulation software including in SILVACO and is used for simulating the manufacturing process of the different constituents of an electronic device, and also treats ion implantation and diffusion of impurities and oxidation and other technological processes of manufacturing. It is generally used to simulate simultaneously With Atlas.

DEVEDIT is an environment where the structure (dimension, doping, ...) and its mesh are drawn.

DECKBUILD is an environment where the simulation program is defined as shown in Figure 4-3.

TONYPLOT is an environment where the simulation results are displayed (structure of the component, distributions of various quantities in it, electrical characteristics ...).

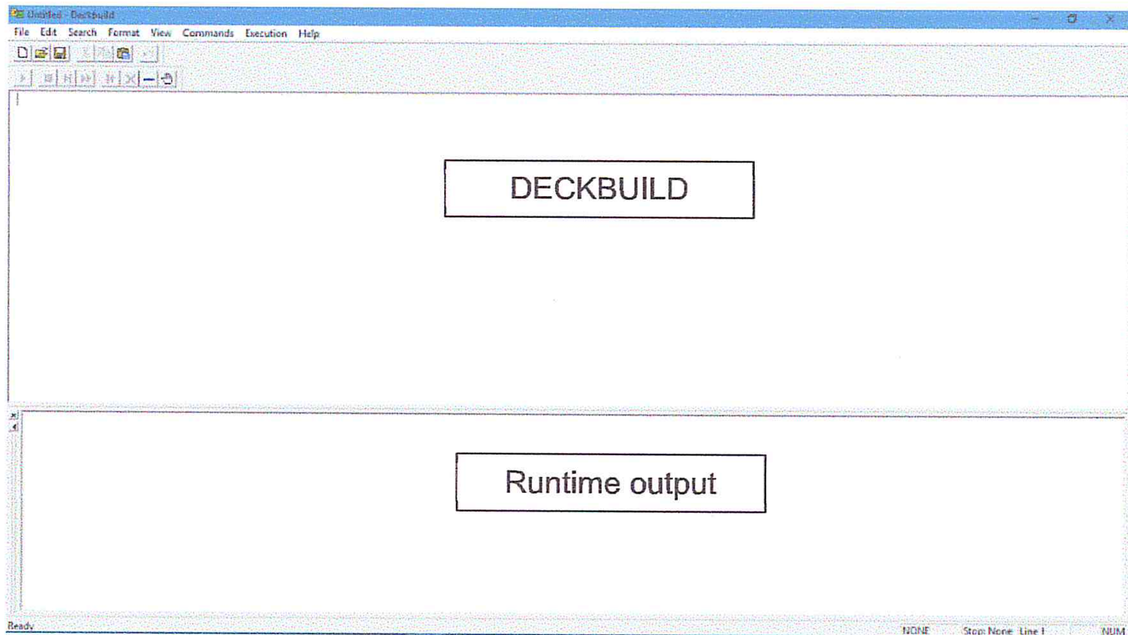

Figure 4-3: DECKBUILD window.

4.1. Atlas Operating Mode:

The command is entered in DECKBUILD by **go atlas.**

4.1.1. Syntax of an instruction:

An instruction takes the following general form:

```
<Instruction> <parameter> = <value>
```

There are 04 types for values (real, integer, logic, character)

The order of parameters is not mandatory; abbreviation is possible but requires no overlap with other instructions.

To write a comment that is not executed by the compiler, we use the symbol **#**.

ATLAS can read **256** characters in a line, but it is better to separate the lines with a backslash at the end of the line in a long statement so that the instructions can be read in a clear way.

It does not differentiate between a capital letter and a lowercase letter.

4.1.2. Instructions' order:

After the presentation of the **"Atlas"** simulation tool of **SILVACO TCAD**, its internal composition and its functioning we will now present the order of Commands specific to Atlas programming logic. Thus, there are five groups of commands, these groups must be organized correctly (Figure 4.2). If the order is not respected, an error message appears and the program does not execute correctly. For example, if the parameters or material models are not placed in the proper order, the simulator does not consider them.

Group	Command
1. Structure specification	MESH REGION ELECTRODE DOPING
2. Models and material	MATERIAL MODELS CONTACT INTERFACE
3. Method selection	METHOD
4. Solution specification	LOG SOLVE LOAD SAVE
5. Results analysis	EXTRACT TONYPLOT

Figure 4-4: Order of groups of Atlas commands (The associated basic commands) [138].

ATLAS is a powerful tool, its instructions are very numerous and its documentation is voluminous that it is difficult to explain everything about it in this thesis.

In order to better explain the ATLAS tool quickly and easily, we have judged in our framework to illustrate the functioning of this tool through concrete examples. Therefore, we're going to give example of the simulation of a **Schottky junction Graphene/GaAs solar cell**, by explaining the process of building its structure in **DECKBUILD** and putting it under sun's illumination with **AM1.5,** and studying its **I-V characteristics.**

The instructions will be illustrated in the rest of this chapter, as well as the results of our simulation.

The following figure represents the structure of the Graphene/GaAs solar cell that we want to simulate in ATLAS.

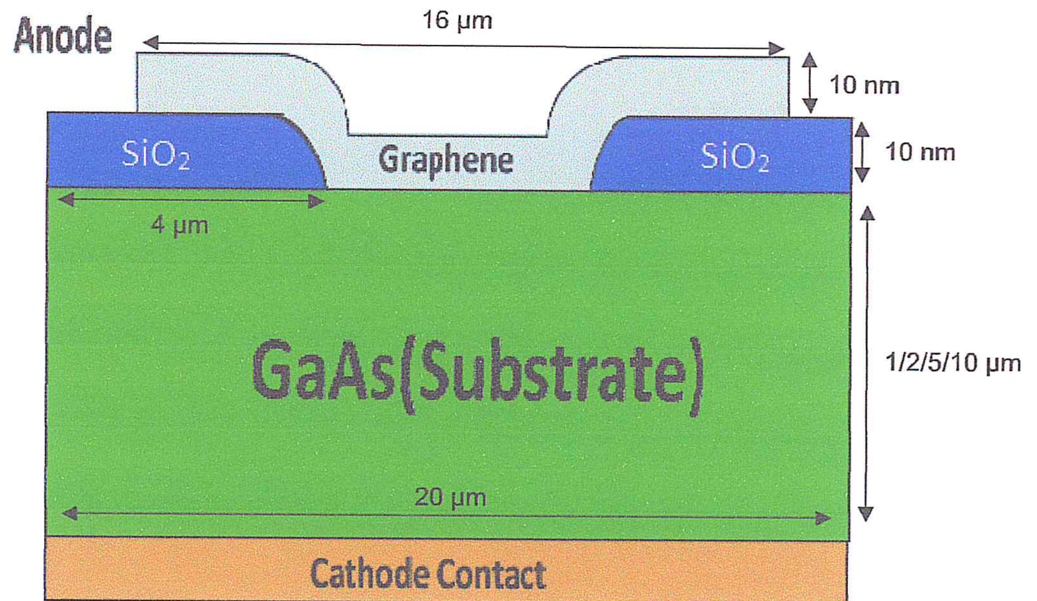

Figure 4-5: The structure of our Graphene/GaAs solar cell that we want to simulate in SILVACO TCAD.

4.2. Structure Specification:

The specification of the structure is obtained by identification of **mesh, regions, electrodes and the doping.**

4.2.1. MESHING

The first section of structure defining statements in the Deckbuild program is the meshing section. This section specifies the two-dimensional grid that is applied to the device with mesh statements.

The following instruction is used to define the meshing:

```
x.mesh location=<value> spacing=<value>
```

The ATLAS device simulator can more easily solve the differential equations at each grid point if there are no abrupt changes between adjacent points. Mesh statements have two parts called location statements and spacing statements.

The location statement, "`loc`", specifies the x or y value in the structure to which the following "`spacing`" statement is applied.

The spacing statement, "`spac`", specifies the spacing between grid lines at that specific location.

The Figure 4-6 represents the meshing that we have created for our structure and its respective instructions entered in DECKBUILD.

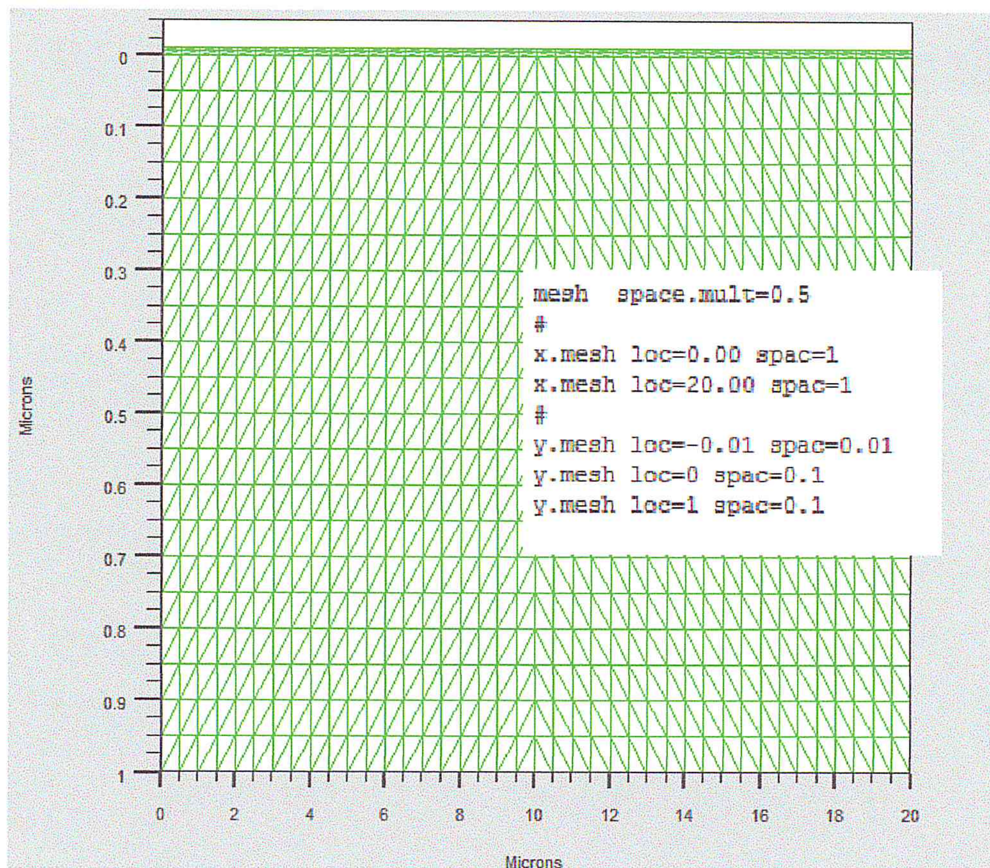

Figure 4-6: The mesh statements creating the mesh for the Graphene/GaAs solar cell are displayed along with a picture of the created mesh

4.2.2. REGION

The region statements include a region number, a material specification, and the region boundaries. The region number is arbitrary but is used in later structure specification sections to apply characteristics to certain regions.

The instruction for defining regions is as follows:

```
REGION    number=<integer>    material=<material_type>    /
<position_parameters>
```

Every region must have a different number as the program produces an error if a statement applies to two different regions.

The material specification statement specifies that the whole region consist of the stated material. This statement gives that whole region default parameters and characteristics of that specified material, which are stored in the **ATLAS material library**. These values include parameters such as the bandgap, electron and hole mobility, and optical properties such as the index of refraction.

P.S: These parameters can be used or changed in another section of the structure defining code if the user wishes to modify a material's original properties.

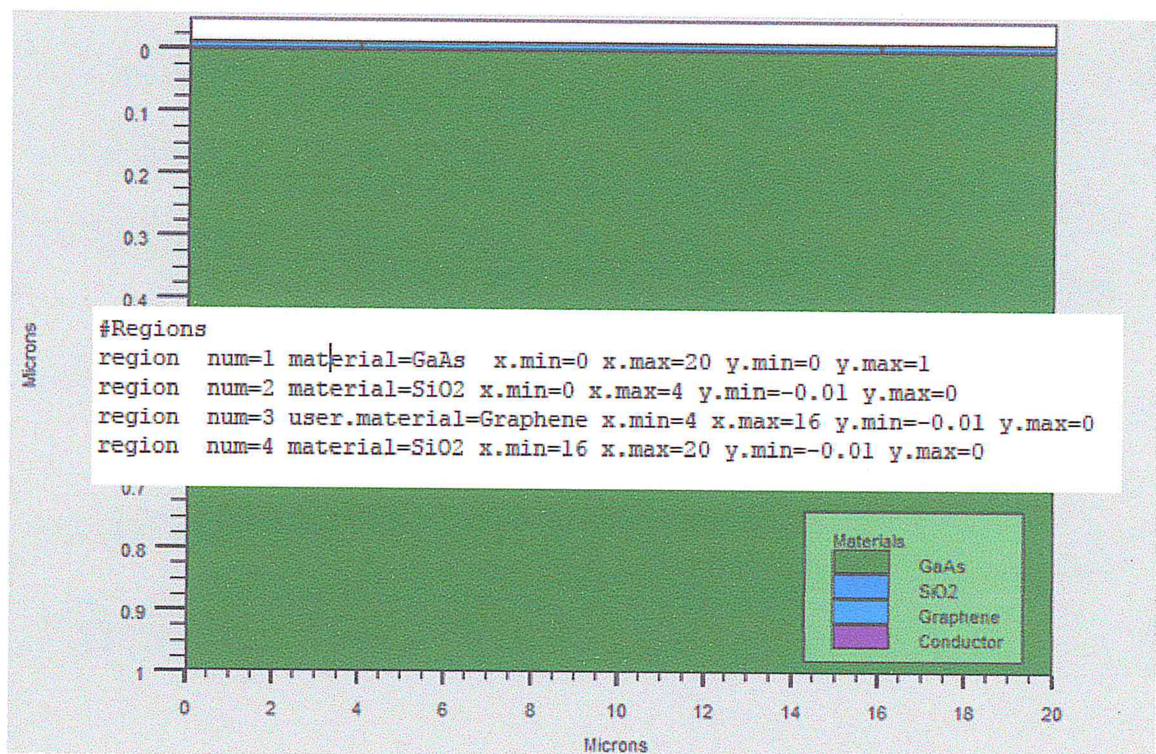

Figure 4-7: The region statements creating the regions of the Graphene/GaAs solar cell are displayed along with a picture of the created regions.

Graphene, as a material, is not included in ATLAS material library, so to define it, we used the statement "`user.material`", which is used to define materials unknown to ATLAS, and we allocated it to its respective region with the position parameters.

The color code is used to identify the materials (each material corresponds to a color), while vertical and horizontal lines mark the boundaries of each region.

There are four specific areas. Each area is defined by a color, and its boundaries are represented with a thick dark line. Figure 4-8 represents the color-code that defines the areas of our Graphene/GaAs soar cell.

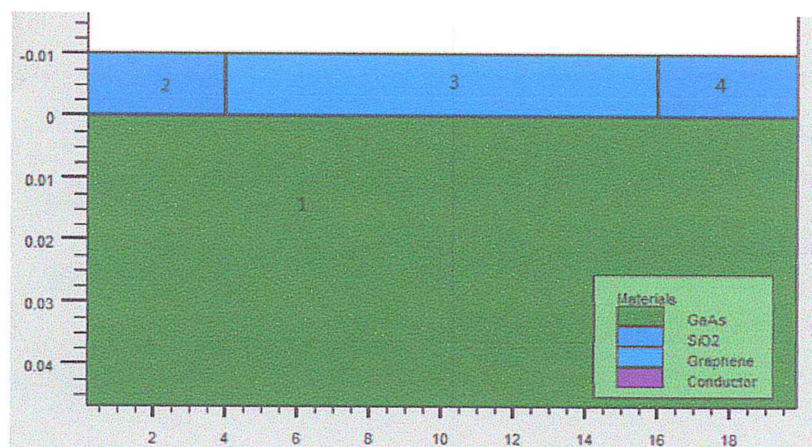

Figure 4-8: A magnified section for areas with specific materials

4.2.3. ELECTRODES

The definition of electrodes is as follows:

```
Electrode Name=<Electrode Name><position_parameters>
```

The user has the ability to determine any number of electrodes with different metal properties. Each electrode definition statement usually has three parts. The user must first name each pole. The name can be followed by the "`material`" statement, which is used to determine the type of contact metal that is used as electrode, which can be one of the materials registered in ATLAS Material Library, or a user-defined material, like in our case where we used Graphene as Anode.

The statement for the definition of an electrode uses maximum and minimum limits of x and y values to set the limits of each electrode. The positions of the electrodes are located by the following instructions:

`X.MIN`: Specifies the starting point of the electrode.

`RIGHT`: the position of the electrode is located to the right of the structure (inverse: `LEFT`).

`TOP`: the position of the electrode is at the top of the structure (inverse: `BOTTOM`).

It is also possible to name the electrode only and identify it as covering the top or the bottom of solar cells.

In our example two anodes at the top of the structure with a length of 2 μm each, and a cathode at the bottom of the structure translated by the following instructions in Figure 4-8

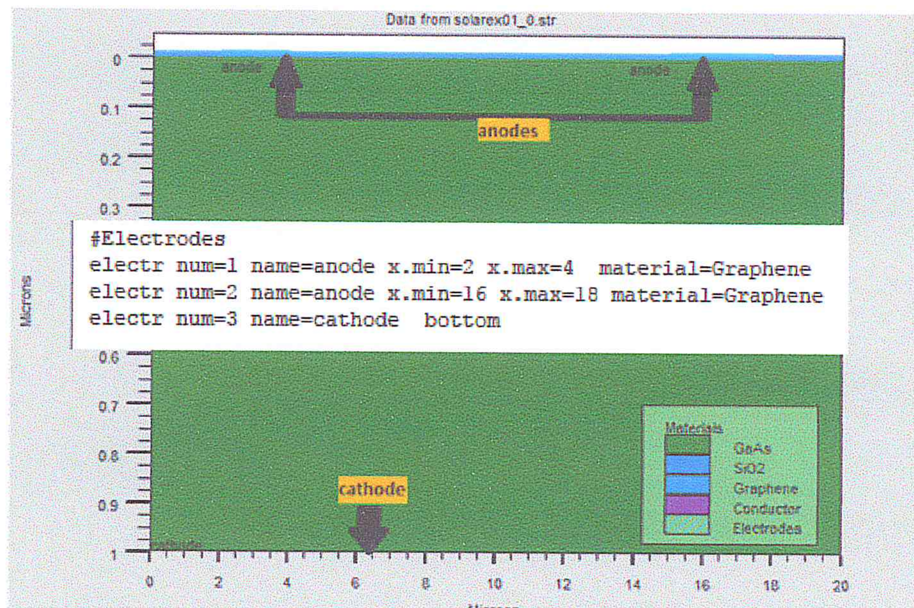

Figure 4-9: The cathode and the anode are made together with the electrode identification code in the Graphene/GaAs solar cell.

4.2.4. DOPING

The last aspect of structure specification that needs to be defined is doping. The format of the Atlas statement is as follows:

```
DOPING <distribution type> <dopant_type> <position parameters>
```

In our work, we used a doping with a uniform n-type distribution and different donor concentrations. For example, the instructions of a donor concentration of 1.e16 cm^{-3} with a uniform distribution for the GaAs substrate is given by:

```
Doping n.type conc=1.e16 uniform region=1
```

Once the structure defined, it can be saved in a **.str** file. This can be accomplished by the following statement:

```
save outf=Graphene_GaAs.str
```

On the other hand, we can view the design of the structure using the **Tonyplot** tool using the following statement:

```
Tonyplot Graphene_GaAs.str
```

4.3. Materials and Model Specification:

After specifying the mesh and doping, we can easily modify the characteristics of the materials used (electrodes, substrate) and change their parameters that ATLAS takes them by default and define our choice of the physical model that will be used during the simulation. These actions are accomplished by the following instructions: MATERIAL, CONTACT, and MODELS.

4.3.1. MATERIAL

The material defining statements that follow the definition of the device structure allow the user to alter the properties of given materials or to input new materials into the device. The statements alter the material properties of a specified metal, semiconductor, or insulator, to simulate more accurately a device that uses materials that do not match the given default values of the ATLAS software and the format for the material statement is as follows:

```
MATERIAL <localization> <material_definition>
```

Different parameters can be defined with different material statements. Examples include the bandgap at room temperature (`EG300`), electron and hole mobilities (`MUN` and `MUP`), recombination parameters (`TAUN` and `TAUP`), etc.

In our example, we used Graphene and GaAs as basic materials in building the structure. The following statements are used to define their properties.

```
Material material=Graphene user.group=semiconductor /
user.default=4H-SIC

Material material=GaAs EG300=1.42 NC300=4.35e17 /
NV300=8.16e18 MUN=8000 MUP=400
```

As a user-defined material, it is necessary to identify to which material group Graphene does belong. Therefore, for its material definition statement, we specified that Graphene does belong to the “semiconductor” material group, using Silicon Carbide (4H-SiC) as a reference material, to be able to alter its properties and transform it to Graphene [136].

For GaAs, we have overridden its ATLAS Material Library parameters and gave it different ones, to obtain results that are more accurate.

4.3.2. MODELS

The physical models fall into five categories: mobility, recombination, carrier statistics, impact-ionization, and tunneling. The syntax of the model statement is as follows:

```
MODELS <model flag> <general_parameter> /
<model_dependent_parameters>
```

The choice of model depends on the materials chosen for simulation. The example below activates several models.

```
MODELS CONMOB FLDMOB SRH
```

CONMOB is the model for the concentration dependent mobility.

FLDMOB is the model of Dependence of the electric field.

SRH is the Shockley-Read-Hall model.

4.3.3. CONTACT

Contact determines the physical attributes of an electrode: anode, cathode, drain, etc. The syntax for contact is as follows:

```
CONTACT NUMBER=<n> |NAME=<name>|ALL
```

Here is our example of a contact statement:

```
contact name=anode workfunction=4.8
```

4.3.4. Numerical METHOD selection

After the materials model specification, the numerical method selection must be specified. There are various numerical methods to calculate solutions to semiconductor device problems. There are three types of solution techniques used in SILVACO ATLAS:

- Decoupled (GUMMEL)
- Fully coupled (NEWTON)
- BLOCK

The **GUMMEL** method solves for each unknown by keeping all other unknowns constant. The process is repeated until there is a stable solution. Newton's method solves all unknowns simultaneously. The **BLOCK** method solves some equations with the **GUMMEL** method and the others with the **NEWTON** method.

The **GUMMEL** method is used for a system of equations that are weakly coupled and where there is linear convergence. **NEWTON** method is used when the equations are strongly coupled with quadratic convergence. In our example, we used the following **Method** order

```
METHOD GUMMEL NEWTON BLOCK
```

In this example, equations are resolved by a GUMMEL method. If the convergence cannot be reached then NEWTON helped solve some of the equations and the others were solved by BLOCK.

4.4. Solutions Specification

So far, we have created the structure, allocated the materials to their specific regions, gave them their properties, specified the physical models, and selected the numerical method for the calculations to be done. The next step is to specify solutions.

To evaluate a solar cell created in DECKBUILD or any other structure defining program, the user can simulate the actual conditions in which a solar cell would operate. This includes variables such as a light beam with its associated optical intensity and angle of incidence, different voltage conditions on the electrodes, and

temperatures, to then extract and study the important optical-electrical parameters such as:

- The Current-Voltage curve (I-V curve)
- The Short Circuit Current (I_{sc})
- The Open Circuit Voltage (V_{oc})
- The Fill Factor
- The Efficiency η (%)

4.4.1. Defining the light source

In simulating solar cells, the user must specify a **beam of light**, which shines upon the device, and can then use any number of electrode conditions and solve statements to gather the desired characteristics of our Graphene/GaAs solar cell.

In this work, the light beam and the electrodes are utilized to set the environment for obtaining solutions of solar cell simulations.

BEAM: In DECKBUILD, the `BEAM` statement, which is used in obtaining solar cell solutions, comes after all of the structure defining statements and before the following solve statements. The light beam defining statement in this work is the following:

```
Beam num=1 x.o=10 y.o=-1 AM1.5
```

In this statement, we specified a light beam of AM1.5 spectral irradiance and the origin of the light beam that is located 1 µm above the center of our Graphene/GaAs solar cell.

4.4.2. Obtaining solutions

Before inputting statements that obtain all of the pertinent solutions for a device, files must be created to store all of the following solutions. These files can be of two types: **.log** and **.str** (structure) files.

LOG: allows all final simulation characteristics to be saved in a .log file (saves a file of .log extension). Any type of data, whether I-V, transient or C-V, generated by the `SOLVE` command is saved after the `LOG` command (thus the saved information is of the electrical type and is, for example, dependent on the voltage Polarization

or light source). If in the program there are several `LOG` commands, each time the log file that was opened before is closed, and a new log file is opened.

The following shows an example of the `LOG` statement.

```
LOG outfile=myoutputfile.log
```

The example saves the current-voltage information into `myoutputfile.log`, which can be viewed graphically in Tonyplot, which allows the user to specify the specific parts of the solution to a graph, as many solutions are all contained in one file and cannot be graphed simultaneously.

Structure files can be saved after a specific solve statement. This file stores all of the data from the solution and allows it to be viewed visually on the device structure. An example of the resulting structure file following a solve statement is given in Figure 23. Tonyplot can convert the numerical data saved into the structure file into a visual representation within the device. Photogeneration rates in the solar cell were stored into the structure file in shown in Figure 4-11. Red and orange regions represent higher photogeneration rates while yellow regions show the lowest photogeneration rates.

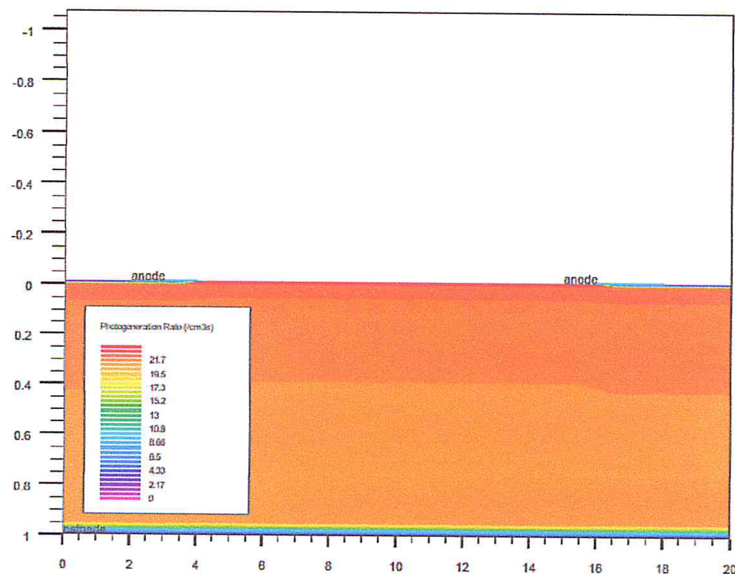

Figure 4-10: Photogeneration data is displayed in different areas of the solar cell.

After defining a log file in which all solutions are to be stored, ATLAS software does an initial solving of the doping profile and the potential at every mesh point in the zero-electrode bias case. This initial solution is obtained when there is no initial

reference zero bias solution but can be specified by the statement `solve init`. After this initial solve statement, the conditions for the specific solve statements can be set. In simulating the operation of a solar cell.

SOLVE: The `SOLVE` statement follows the `LOG` statement. SOLVE performs a solution for one or more bias points. The following `SOLVE` statement is the one that was used in our study to obtain the solutions.

```
SOLVE b1=1.0
```

This statement applies the equivalent of **one sun** from the earlier defined light source (in `BEAM` statement) and solves the pertinent quantities, such as photogeneration rates and optical intensities, at each mesh point as well as the electrode currents.

After the beam of light has been applied, solutions at different electrode voltages can be obtained to create the solar cell's I-V curve.

```
solve vanode=0 name=anode vstep=0.1 vfinal=0.7
```

This statement is to obtain solutions for the illuminated solar cell at a range of anode voltages. It declares an initial anode voltage of 0 V and obtains solutions in the range from 0 V to 0.7 V in increments of 0.1 V.

By sweeping across anode voltages from 0 V to V_{oc} for the solar cell, the I-V curve is obtained. The results can later be displayed in Tonyplot in the form of a graph.

LOAD AND SAVE: The LOAD statement enters previous solutions from files as initial guess to other bias points. The SAVE statement enters all node point information into an output file.
The following are examples of LOAD and SAVE statements:

```
save outf=Graphene_GaAs.str
```

In this case, `Graphene_GaAs.str` has information saved after a `SOLVE` statement. Then, in a different simulation, `Graphene_GaAs.str` can be loaded as follows:

```
load infile=Graphene_GaAs.str
```

4.5. Results' Analysis

Once a solution has been found for a semiconductor device problem, the information can be displayed graphically with TonyPlot. Additionally, device parameters can be extracted with the `EXTRACT` statement, which can be written manually in DECKBUILD, or selected from the "Insert Extract" menu from the "Commands" button in DECKBUILD's menu bar.

In the example below, the `EXTRACT` statement obtains the current and voltage characteristics of a solar cell. This information is saved into the `IVcurve.dat` file, then, TonyPlot displays the information in the IVcurve.dat file in the form of a graph.

```
    EXTRACT   NAME="iv"   curve(v."anode",   i."cathode")   /
OUTFILE="IVcurve.dat"
    TONYPLOT IVcurve.dat
```

The following figure is an example of a solar cell's I-V curve displayed in Tonyplot using a simulation script of a silicon solar cell, which came pre-installed with SILVACO (TCAD).

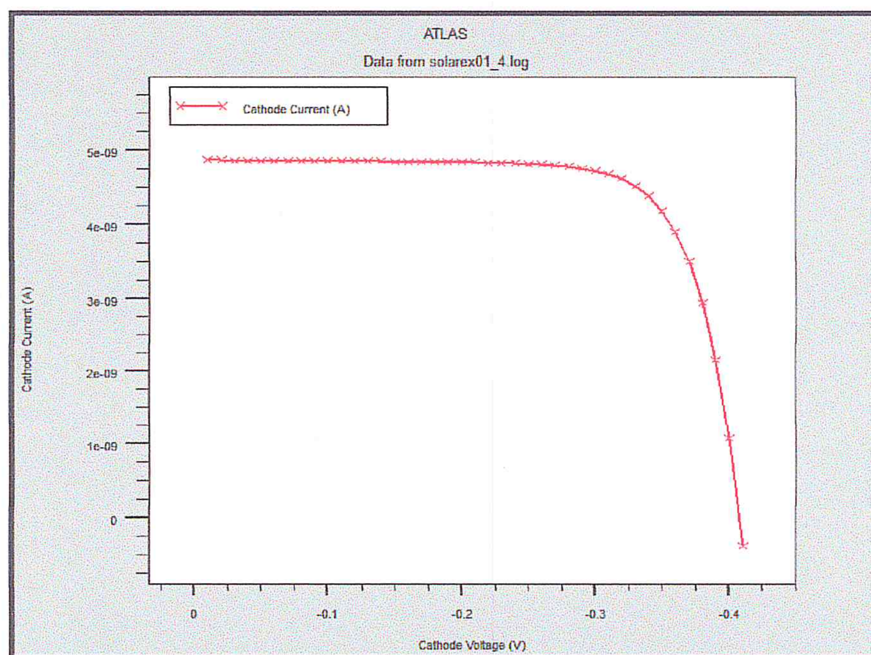

Figure 4-11. I-V curve of a silicon solar cell as it is displayed in Tonyplot.

IV.I. SIMULATION RESULTS AND DISCUSSION

1. INTRODUCTION

In this chapter, we are going to talk about the results that we have gathered from the simulation. The variations of GaAs thickness, doping, and Graphene work function are applied to observe their effect on the value of Efficiency, Fill Factor, V_{oc} and J_{sc}. The results are then compared with the results from article Ref.1. Therefore, we tried to replicate the one that was studied in article Ref.1.

The structure was obtained easily, but the results couldn't be obtained due to the fact that many parameters were not mentioned in the article including:

- The densities of state (N_C and N_V)
- The recombination parameters
- The Dielectric permittivity of Graphene
- The optical parameters, including the refractive index that was used to obtain the optical transmittance of Graphene

Efforts were put to obtain these parameters, through calculations and research.

2. GRAPHENE PARAMETERS OBTAINED AND USED IN THIS WORK

Silicon Carbide (4H-SiC) was used as a base material for modeling graphene. The main parameters that were modified to give 4H-SiC partly metallic as well as semiconductor properties are the electron and hole mobilities (μ_n and μ_p respectively) and the bandgap.

2.1. Densities of State (N_C and N_V)

To calculate these parameters, we had to use the value of graphene's sheet resistance R_{SH} that was obtained in previous experimental studies [131]. The relation that allowed such parameters to be obtained is the following:

$$R_{SH} = \frac{\rho}{t} \tag{4.1}$$

Where t is graphene's thickness equal to $10\ nm$, R_{SH} is the sheet resistance, and ρ is the semiconductor resistivity given by:

$$\rho = \frac{1}{q(\mu_n n + \mu_p p)} \quad (4.2)$$

Where q is the electron charge, n and p are the concentrations of electrons and holes respectively, which are equal to each other in the case of intrinsic semiconductor, as well as the values of N_C and N_V. The following equation was used to calculate the two densities of state:

$$n = p = \sqrt{N_C N_V}.\, e^{\frac{-E_g}{2kT_L}} \quad (4.3)$$

In this work, the used bandgap value of graphene is near zero ($E_g \approx 0$) which leaves us with the following relation:

$$n = N_c = N_V \quad (4.4)$$

To get the concentration value n, both mobilities μ_n and μ_p were set to be equal to $15\,000\ cm^2/V.s$ [130]. After a numerical application, we would the following results

$$N_c = N_V = 1.94 \times 10^{16}\ cm^{-3} \quad (4.5)$$

2.2. Refractive Index

One of the important optical parameters is the Refractive Index. It is to determine how much light is bent, or refracted, when entering a material. It is described by Snell's law of refraction:

$$n_1 \sin\theta_1 = n_2 \sin\theta_2 \quad (4.6)$$

Where θ_1 and θ_2 are the angles of incidence and refraction, respectively, of a light beam crossing the interface between two media with refractive indices n_1 and n_2.

The refractive indices also determine the amount of light that is reflected when reaching the interface, as well as the critical angle for total internal reflection and Brewster's angle.

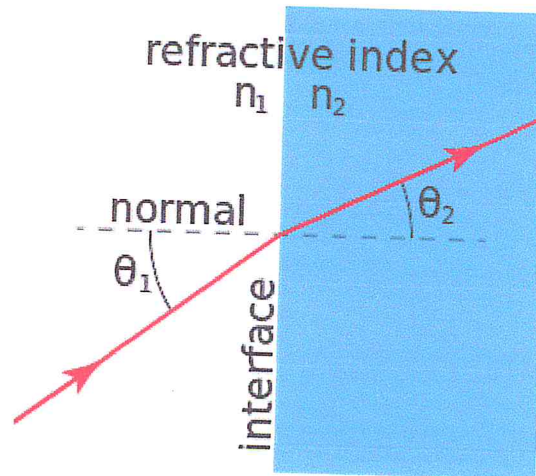

Figure 4-12: The refraction of a red-light beam traveling between two materials with different refractive indices.

2.2.1. Complex refractive index

When light passes through a medium, some part of it will always be attenuated (absorbed). This can be conveniently taken into account by defining a complex refractive index,

$$\underline{n} = n + i\kappa \tag{4.7}$$

Here, the real part n is the refractive index and indicates the phase velocity, while the imaginary part κ is called the extinction coefficient — although κ can also refer to the mass attenuation coefficient and indicates the amount of attenuation when the electromagnetic wave propagates through the material.

In the case of graphene, a small part of the light passing through it is attenuated. Thus, it's refractive index is represented in a complex from.

It is important to know that, unlike other studies, the values of graphene's refractive index that were introduced in this work are **Wavelength dependent,** which gives us the following relation of graphene's refractive index

$$\underline{n}(\lambda) = n(\lambda) + i\kappa(\lambda) \tag{4.7}$$

The following graphs represents the values of graphene's refractive index depending on the optical wavelength [132]:

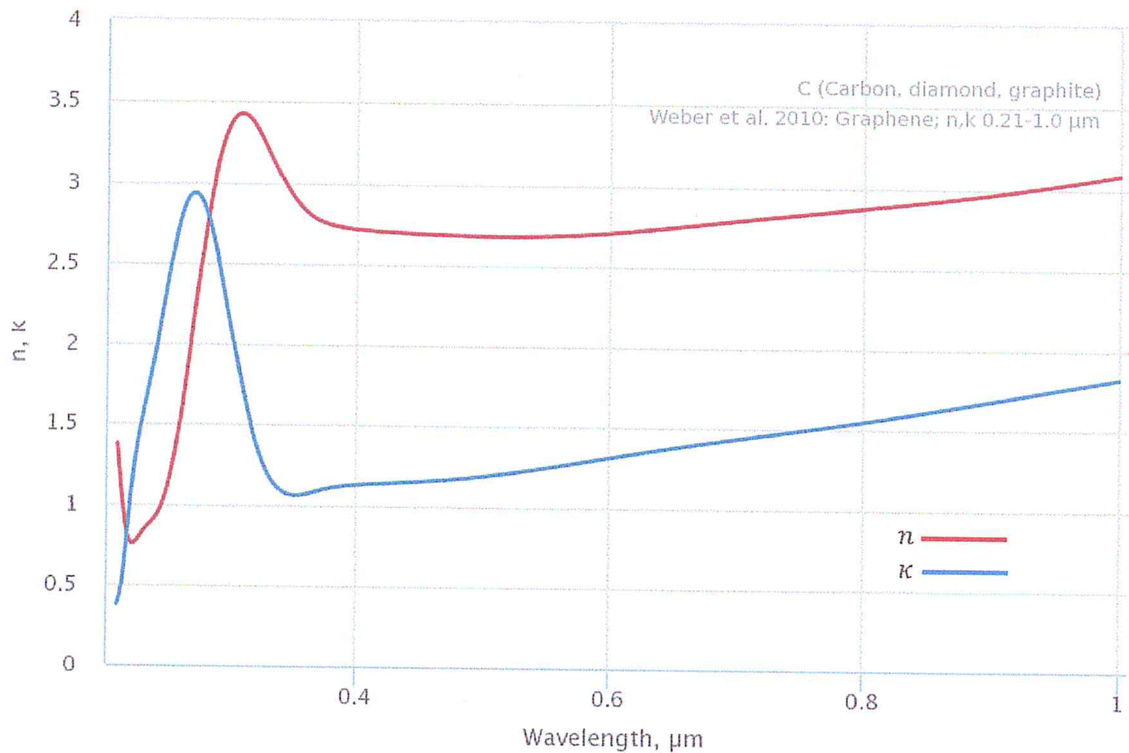

Figure 4-13: Real and Imaginary refractive index of graphene versus Optical Wavelength [132].

These values were introduced to our simulation, which allowed us to obtain results that are close to reality.

2.3. Other properties

Table 4-1 contains the values that were given to other properties to graphene [132-135].

Table 4-1. The parameters of graphene that were used in the simulation

Parameter type	ATLAS Identifier	Value
Band parameters	Bandgap (E_g)	0.026
	Permittivity (ε)	5.6
	Work function	4.4, 4.55, 4.8
Recombination parameters	taun0,taup0	0
	nsrhn,nsrhp	0
	ksrhcn,ksrhcp	0
	ksrhtn,ksrhtp	0
	ksrhgn,ksrhgp	0
	augn,augp	0
	augkn,augkp	0

	kaugcn,kaugcp	0
	kaugdn,kaugdp	0
	Etrap	0
	Copt	0

3. RESULTS AND DISCUSSION

3.1. Evaluating Solar Cell's Electrical and Optical Properties

To evaluate the solar cell's performance, the thickness of the undoped GaAs substrate was varied. The different GaAs thicknesses that were used are: $1\mu m, 2\mu m, 5\mu m$ and $10\mu m$.

After this, instead of varying the thickness of GaAs substrate, it was set to be constant at $5\mu m$ and an n-type doping was applied to the GaAs substrate and varied from $1e14\ cm^{-3}$ to $1e16\ cm^{-3}$.

The effect of varying graphene's Work function was studied too. Different values were used including: 4.4, 4.55, and 4.8 (for the case n-type doped GaAs).

To obtain the electrical and optical characteristics of our solar cell, a sun illumination of 1.5 AM is simulated upon the structure of our solar cell. A forward bias current is then applied to its electrodes.

The important data, figures and graphs are stored into .log and .str files, then extracted and plotted using the "*extract*" command and "*Tonyplot*".

All obtained results of this work are summarized in the following table:

Table 4-2. Results of the simulation for different parameters.

Thickness µm	Workf	Doping	Jsc (mA/cm^2)	Voc (v)	FF	η (%)
1	4,55	None	6.10	1.00	0.51	3.29
2	4,55	None	6.10	0.97	0.51	5.03
5	4,55	None	6.10	0.94	0.49	4.74
10	4,55	None	6.10	0.93	0.45	4.58
5	4,4	None	6.08	0.92	0.36	3.38
5	4,8	None	6.10	1.11	0.62	6.99
5	4,8	1,00E+14	6.10	1.37	0.68	9.54
5	4,8	1,00E+15	6.10	1.37	0.68	9.52
5	4,8	1,00E+16	6.10	1.37	0.68	9.50

3.1.1. Effect of GaAs substrate thickness

With GaAs acting as an absorption area, and graphene as a transparent electrode allowing light to penetrate into the GaAs substrate.

Due to the difference between GaAs and Graphene work functions, a Schottky junction appears between them.

Figures IV.3(a) - IV.3(d) show the photogeneration rates of our Graphene-GaAs solar cell under AM 1.5 illumination, with GaAs depth maintained at $1\mu m, 2\mu m, 5\mu m$ and $10\mu m$ respectively, with no doping, and the work function maintained at *4.55*

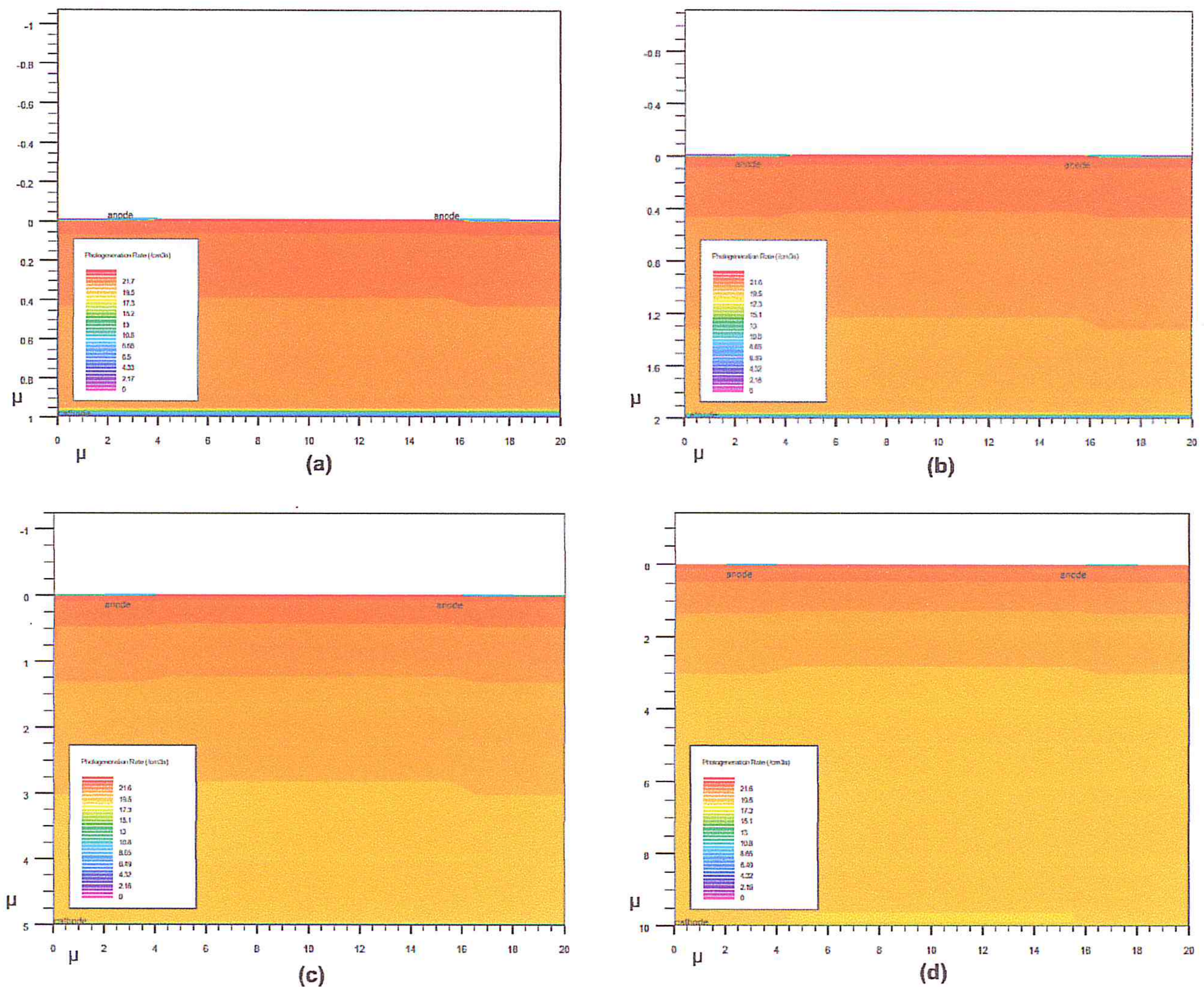

Figure 4-14: The Photogeneration rate in GaAs substrate under AM1.5 illumination versus different thicknesses.

We notice that the light could be absorbed in the barrier layer, and inside the GaAs substrate. The results show that the most effective absorption is located in the surface (approximately 0.1 µm). As from figure IV-3. (d), we notice that 10 µm GaAs thickness is enough for full spectrum absorption, due to the fact that the intensity of the photo-generated carriers dramatically reduces in the deep area of the GaAs substrate.

The following figure represents the I-V curves of our Graphene-GaAs solar cell with the previous parameters of thicknesses:

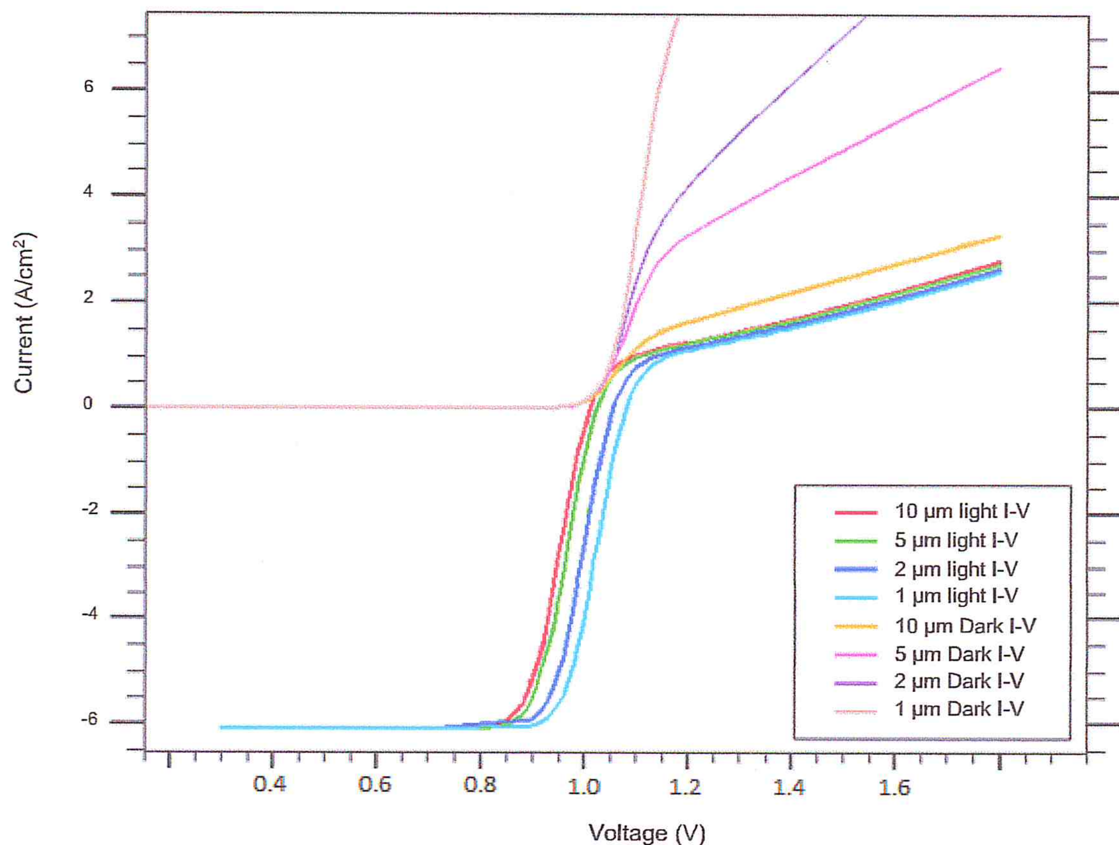

Figure 4-15: Current-Voltage curves of Graphene-GaAs solar cell versus different GaAs thicknesses.

Here we notice that despite the thickness of the GaAs substrate affects the distance between the *Dark I-V* and *Light IV* curves. If we look at the Dark and Light I-V curves of 1µm GaAs thickness, we notice that they do not cross with each other,

and they are separated by a distance between them. While it is clear that both Dark I-V and Light I-V curves for 10µm GaAs thickness cross with each other.

3.1.2. Effect of Graphene Work function

According to the theoretical model described in chapter II, the barrier height ϕ_B is related to the difference between graphene work function ϕ_G and electron afnity χ of GaAs. Consequently, higher work function increases ϕ_B and further enhances the built-in potential V_{bi} via the equation $V_{bi} = \phi_B - V_n$ where V_n means the distance between E_c and E_f in GaAs.

Therefore, the increase of graphene work function implies the increase of V_{bi} corresponding to the upper limitation of V_{oc} . Lancellotti et al. reported the dependence of graphene work function and transmittance on the number of layers [137]. We calculated the *I-V* curves of graphene GaAs solar cells versus different graphene work functions.

The following figure represents the graphs of results we obtained from these modifications:

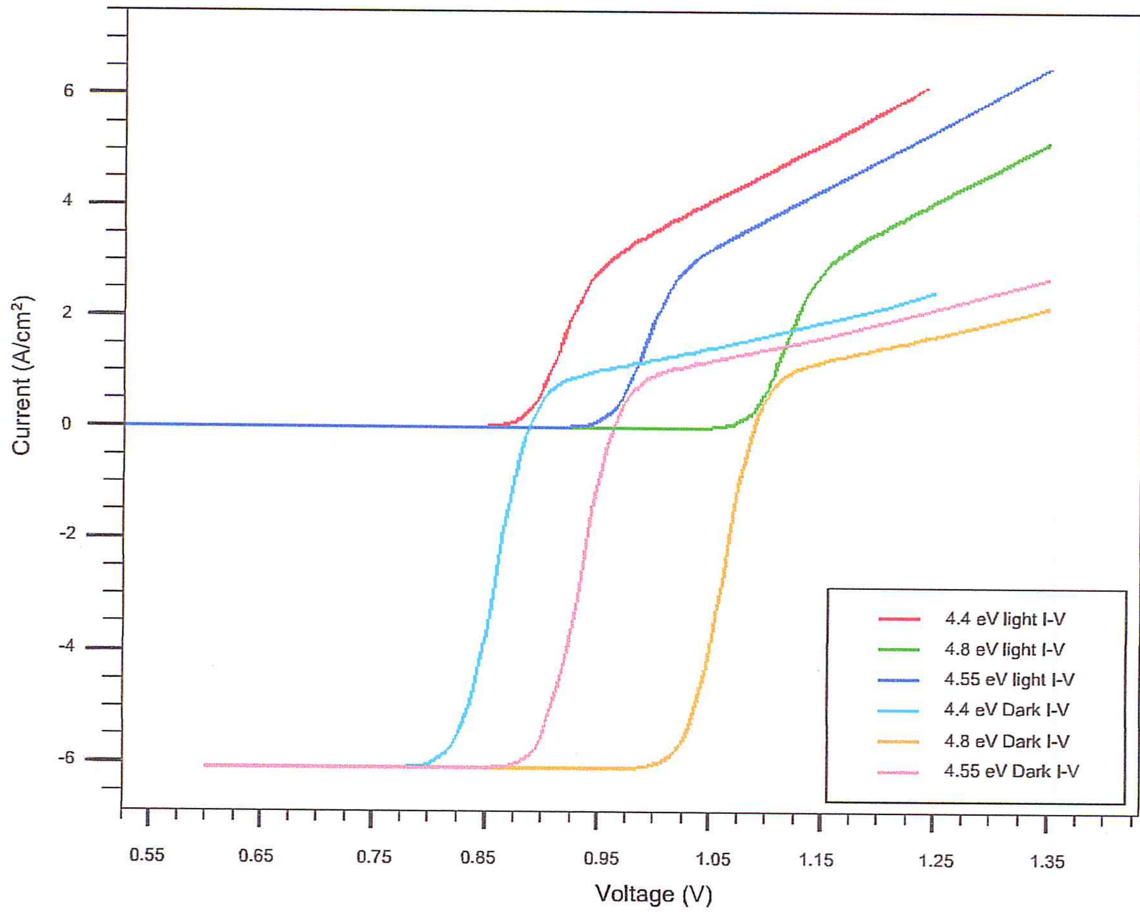

Figure 4-16: Current-Voltage curves of Graphene-GaAs solar cell versus different Graphene Work functions.

From the graphs, we notice that the changes in graphene's work function cause a significant shift in I_{sc} and V_{oc}, which confirms the theory.

3.1.3. Effect of n-type doping

In solid-state physics, it is known that the Fermi level increases in an n-type doped semiconductor. For doping concentrations 1×10^{14} cm^{-3}, 1×10^{15} cm^{-3}, and 1×10^{16} cm^{-3}, we noticed that all solar cell's characteristics J_{sc}, V_{oc}, FF and $\eta_{(\%)}$ are approximately the same, despite the changes in doping levels.

The following figure is a graphic representation of I-V characteristics of the studied solar cell versus different doping levels:

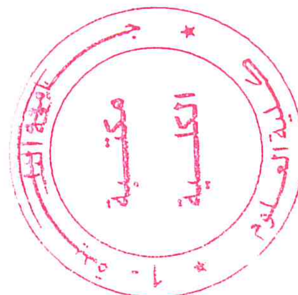

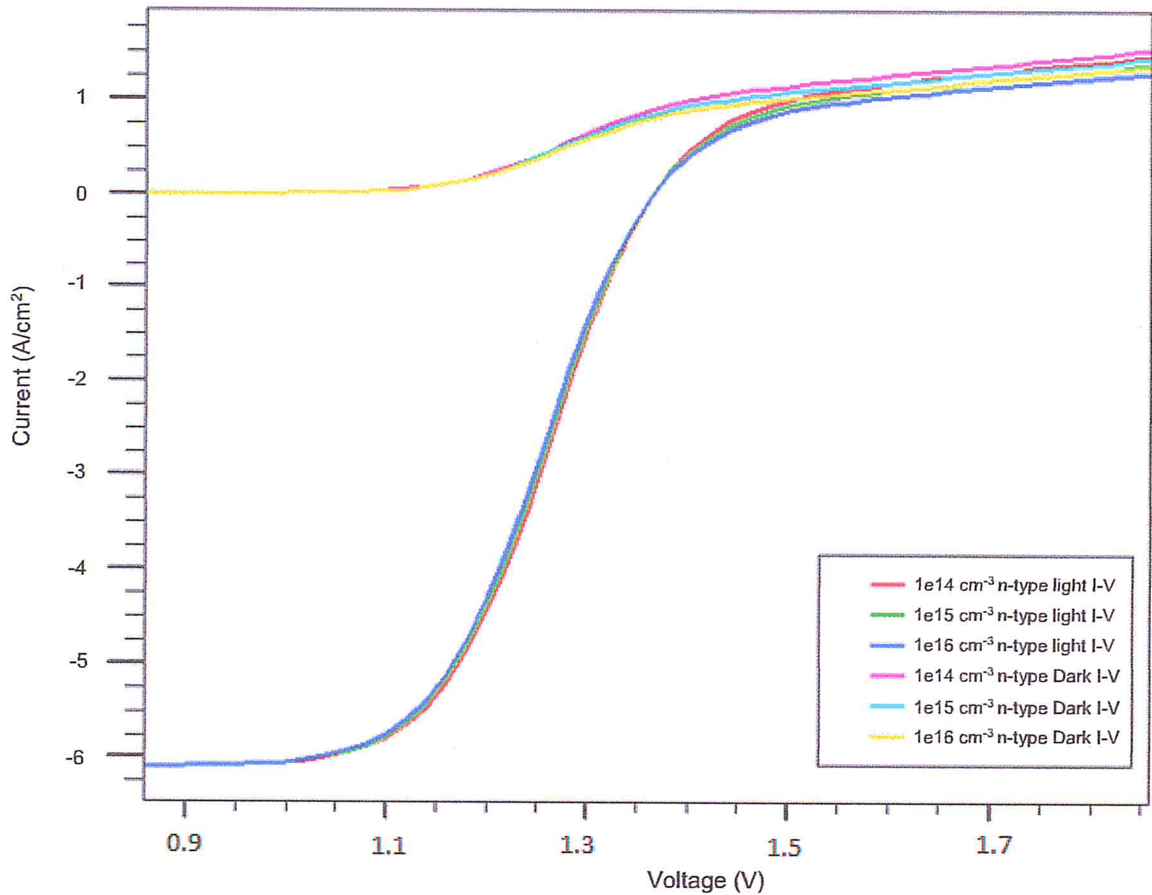

Figure 4-17: Current-Voltage curves of Graphene-GaAs solar cell versus different n-type doping concentrations.

From the graphs, we can notice that the Light I-V curves of different doping concentrations are almost identical, then they start to separate in the area where the applied voltage is higher than V_{oc}

4. CHAPTER SUMMARY

In this chapter, we have presented the software that was used in our work to simulate a Graphene-GaAs solar cell, seen what are the different steps to create the structure, allocate materials to it, give these materials their respective properties, study the optical-electrical behavior of our devices and extract the different results represented into graphs and numerical results.

These results showed us that the most important factors for higher efficiencies are:

- A thin GaAs substrate (1μm)
- A "moderate" concentration of n-type doping
- A relatively high graphene work function

Thus, we conclude that it is important to take these factors into consideration in future projects in the subject of using graphene in solar cells and other optoelectronic devices.

V. General Conclusion

In this work, we have shown how a Graphene Schottky junction Solar Cell is modeled in SILVACO ATLAS (TCAD). This model was incorporated into a GaAs Solar Cell and it was shown how it can contribute to improving the efficiency of the solar cell compared to a normal p-n junction solar cell. The unique properties of Graphene layer on the surface of the solar cell allow for better charge carrier collection due to its ultra-high charge carrier mobilities and its low recombination rates, while having very small losses of light input power based on the light transmission of the Graphene layer.

The performance of our solar cell depended strongly on the properties of the Graphene-based Schottky contact. The ultra-high mobility of the charge carriers allowed for a better collection of the current, allowing it to travel through the contact with a low resistance path.

Another property that allowed for such great performance of the solar cell is Graphene's transparency to the visible light spectrum; This allowed for more collection of the light spectrum, which generates more electron-hole pairs in the depletion region, and a wider Graphene contact for better collection of the generated photo-current. This was possible by introducing the values of the wavelength-dependent refractive index of Graphene.

Additionally, the thickness of the GaAs substrate played a significant role in the performance of the solar cell; we have noticed that the thicker the substrate gets, the lower efficiencies we get. We interpreted this by assuming that the generated electron-hole pairs had to travel longer distances to get to the contacts, which resulted in higher recombination rates, resulting in a lower photo-current, which is related directly to the performance of the solar cell.

Finally, the effect of uniform n-type doping of the GaAs substrate was also investigated. The efficiency increases with higher doping and reaches a saturation state. The results show that efficiency of Graphene/GaAs solar cell with 1014 cm-3 doping concentration is higher than the efficiency of Graphene/GaAs solar without doping. We also noticed that the efficiency does not change or slightly decreases when increasing doping concentration. This could be due to the movement of the depletion boundary close to the graphene surface.

Solar cells are currently a high priority for both the military and the civilian sectors as a viable source of renewable energy, and as a power source in remote areas such as space or countryside. Research regarding the improvement in efficiency of solar cells have to be intensified in our universities and research centers, as nations are shifting from traditional sources of energy, such as fossil fuels, by attempting to generate more energy from renewable resources for domestic and industrial use, and to allow new technologies to be accessible in remote areas.

LIST OF SYMBOLS

Symbol	Name	Unit
h	Planck's constant	$eV.s$
ν	Photon frequency	s^{-1}
c	Light speed in vacuum	m/s
K_B	Boltzmann constant	$photons.cm^{-2}s^{-1}$
T	Room temperature	$°K$
q	Elementary charge	C
W	Depletion region width	μm
λ	Photon Wavelength	μm
N_C, N_V	Densities of State	cm^{-3}
E_F	Fermi energy state level	eV
E_C	Lowest level of energy in the conduction band	eV
E_V	Lowest level of energy in the valence band	eV
n_i	Intrinsic concentration	cm^{-3}
n	Density of free electrons	cm^{-3}
p	Density of free holes	cm^{-3}
ϕ_B	Schottky Barrier height	eV
ϕ_m	Metal work function	eV
χ	Electron affinity in a semiconductor	eV
V_{BI}	Built-in potential	eV
ϕ_s	Semiconductor work function	eV
N_a , N_d	Concentration of acceptors and donors respectively	cm^{-3}
V_{OC}	Open circuit voltage	V
V_A	Applied voltage	V
V_{max}	Maximum power voltage	V
I_{SC}	Short circuit current	mA
I_F	Forward bias current	mA
I_{max}	Maximum power current	mA
I_0	Initial current	mA
I_R	Reverse bias current	mA
k	Boltzmann's constant	$eV.K^{-1}$
A	Area of contact between metal and semiconductor	cm^2
R_S	Series resistance	Ω
V_{RB}	Reverse Bias Voltage	V
ε_m	Permittivity in metal	$\mathrm{F \cdot cm^{-1}}$
ε_0	Permittivity in vacuum	$\mathrm{F \cdot cm^{-1}}$
P_{max}	Maximum power	$Watts$
FF	Fill Factor	%
η	Efficiency	%
$A.M$	Air mass	
E	Photon energy	eV
E_g	Energy Bandgap	eV
$GaAs$	Gallium Arsenide	
Si	Silicon	

$4H - SiC$	Silicon carbide	
τ_c	Mean free time between collisions	s
$\underline{n}$	Complex refractive index	
n	Real part of the complex refractive index	
κ	Imaginary part of the complex refractive index	
R_{SH}	Sheet resistance	Ω/sq
ρ	Resistivity	$\Omega.cm$
μ_n, μ_p	Electron and hole mobilities	$cm^2/V.s$
t	Graphene thickness	nm

REFERENCES:

[1] Novoselov, K. S. et al. Electric field effect in atomically thin carbon films. Science 306, 666–669 (2004).

[2] M. Burghard, H. Klauk, and K. Kern, Adv. Mater. 21, 2586 (2009).

[3] X. Li, Y. Zhu, W. Cai, M. Boryslak, B. Han, D. Chen, R. D. Piner, L. Colombo, and R. S. Ruoff, Nano Lett. 9, 4359 (2009).

[4] H. G. Craighead, J. Cheng, and S. Hackwood, Appl. Phys. Lett. 40, 22 (1982). 5. S. R. C. Vivekchand, C. S. Rout, K. S. Subrahmanyam, A. Govindaraj, and C. N. R. Rao, J. Chem. Sci. 120, 9 (2008).

[6] D. A. Dikin, S. Stankovich, E. J. Zimney, R. D. Piner, G. H. B. Dommett, G. Evmenenko, S. T. Nguyen, and R. S. Ruoff, Nature 448, 457 (2007).

[7] F. Schedin, A. K. Geim, S. V. Morozov, E. W. Hill, P. Blake, M. I. Katsnelson, and K. S. Novoselov, Nat. Mater. 6, 652 (2007).

[8] G. Wang, X. Shen, J. Yao, and J. Park, Carbon 47, 2049 (2009).

[9] J. Li, J. Chen, B. Shen, X. Yan, and Q. Xue, Appl. Phys. Lett. 99, 163103 (2011).

[10] D. Ye, S. Moussa, J. D. Ferguson, A. A. Baski, and M. S. Shall, Nano Lett. 12, 1265 (2012).

[11] X. Li, H. Zhu, K. Wang, A. Cao, J. Wei, C. Li, Y. Jia, Z. Li, X. Li, and D. Wu, Adv. Mater. 22, 2743 (2010).

[12] W. J. Hong, Y. X. Xu, G. W. Lu, C. Li, and G. Q. Shi, Electrochem. Commun. 10, 1555 (2008).

[13] S. K. Behura, P. Mahala, A. Ray, I. Mukhopadhyay, and O. Jani, Appl. Phys. A (2012), DOI: 10. 1007/s00339-012-7335-2

[14] G. Xiao, Y. Tao; J. Lu; Z. Zhang, "Highly transparent and conductive carbon nanotube coatings deposited on flexible polymer substrate by solution method,"Proc. 3rd International Nanoelectronics Conference (INEC), pp.208–209, 3–8Jan. 2010.

[15] J. Guo, "Carbon Nanotube Electronics, Modeling, Physics, and Applications," Doctoral Dissertation, Purdue University, 2004.

[16] B. Zeghbroeck, Principles of Electronic Devices, http://ecee.colorado.edu (accessed March 4, 2012).

[17] A. Bates, "Novel Optimization Techniques for Multijunction Solar Cell Design USING SILVACO ATLAS," Master's Thesis, Naval Postgraduate School, 2004.

[18] "Chapter 3: Metal Semiconductor Junctions" Retrived: June 1, 2007 Copyright 2004 B. Van Zeghbroeck http://ece-www.colorado.edu/~bart/book/book/chapter3/ch3_3.htm

[19] Ben G Streetman "Solid State Electronic Devices" 3rd Edition, Prentice Hall Series in Solid State Physical Electronics. ISBN 0-13-822941-4 Date: pg. 200 -205 December 1990.

[20] S. Michael, EC3230 Lecture Notes, Naval Postgraduate School, Winter 2004 (unpublished).

[21] S. Michael, "The Design and Optimization of Advanced Multijunction SolarCells," Presented at the 35th IEEE PV Specialists Conference, Vancouver, Canada, 2004.

[22] Gueymard, C.; Myers, D.; Emery, K. (2002). "Proposed reference irradiance spectra for solar energy systems testing". Solar Energy. **73** (6): 443–467. doi:10.1016/S0038-092X(03)00005-7.

[23] Reference Solar Spectral Irradiance: Air Mass 1.5 NREL retrieved 1 May 2011

[24] Reference Solar Spectral Irradiance: ASTM G-173 ASTM retrieved 1 May 2011

[25] Reference Solar Spectral Irradiance & PV Cell Operational Regions (ASTM G173-03) ASTM

[26] R.Castagné et all, "Circuits intégrés en arsenure de de Gallium. Physique, Technologie et règles de conception", Masson et CINET ENST Paris, 1989.

[27] S.Laval, "Physique des semi-conducteurs III-V", Ecole d'été d'optoélectronique,2002.

[28] III-V compound semiconductor material systems *"Design, fabrication, characterization and modeling of: High Electron Mobility Transistors, RTD, Gunn diodes, nanocolumns."* ISG-1, Research Center Juelich, Germany.

[29] H. Welker, Z. Naturforsch, Vol. A, No. 7, p. 744, 1952.

[30] S. M. Sze, Semiconductor Devices Physics and Technology, J. Wiley, New York, 1985.

[31] R. F. Pierret, Semiconductor Fundamentals, Addison-Wesley Publishing, New York, 1989.

[32] R. Williams, Modern GaAs Processing Methods, Artech House, Dedham, MA, 1990.

[33] H. C. Casey, "Diffusion in III-V Compound Semiconductors," Atomic Diffusion in Semiconductors, D. Shaw, Editor, Plenum, New York, 1973.

[34] S. Y. Chiang, "Properties of Vacancy Defects in GaAs Single Crystals," J. Appl. Phys., Vol. 45, p. 2986, 1975.

[35] S. Markram-Ebied, "Nature of EL2: The Main Native Midgap Electron Trap in VPE and Bulk GaAs," in Semi-insulating III-V Materials, D. Look, Editor, Shiva Publishing Ltd., England, 1984.

[36] Y. Nanishi, Jpn. J. Appl. Phys., Vol. 22, 1983.

[37] S. Miyazawa, Appl. Phys. Lett., Vol. 44, 1984.

[38] T. Honda, Jpn. J. Appl. Phys., Vol. 22, 1983.

[39] S. Wemple, "*Thermal Design of Power GaAs,*" in GaAs FET Principles and Technology, J. DiLorenzo, Editor, Artech House, Dedham, MA., 1982.

[40] A. K. GEIM AND K. S. NOVOSELOV, *"The rise of graphene",* Manchester Centre for Mesoscience and Nanotechnology, University of Manchester, Oxford Road, Manchester M13 9PL, UK

[41] Fradkin, E. Critical behavior of disordered degenerate semiconductors. Phys. Rev. B 33, 3263–3268 (1986).

[42] Haldane, F. D. M. Model for a quantum Hall effect without Landau levels: Condensed-matter realization of the 'parity anomaly'. Phys. Rev. Lett. 61, 2015–2018 (1988).

[43] B. Ozpeneci, L.M. Tolbert, "Comparison of Wide –Bandgap Semiconductors for Power Electronics Applications" Oakridge National Laboratory, pg. 6-10 December 12, 2003

[44] Novoselov, K. S. et al. Two-dimensional atomic crystals. Proc. Natl Acad. Sci. USA 102, 10451–10453 (2005).

[45] Novoselov, K. S. et al. Two-dimensional gas of massless Dirac fermions in graphene. Nature 438, 197–200 (2005).

[46] Zhang, Y., Tan, J. W., Stormer, H. L. & Kim, P. Experimental observation of the quantum Hall effect and Berry's phase in graphene. Nature 438, 201–204 (2005).

[47] Peierls, R. E. Quelques proprietes typiques des corpses solides. Ann. I. H. Poincare 5, 177–222 (1935).

[48] Landau, L. D. Zur Teorie der phasenumwandlungen II. Phys. Z. Sowjetunion 11, 26–35 (1937).

[49] Landau, L. D. & Lifshitz, E. M. Statistical Physics, Part I (Pergamon, Oxford, 1980).

[50] Mermin, N. D. Crystalline order in two dimensions. Phys. Rev. 176, 250–254 (1968).

[51] Venables, J. A., Spiller, G. D. T. & Hanbucken, M. Nucleation and growth of thin flms. Rep. Prog. Phys. 47, 399–459 (1984).

[52] Evans, J. W., Tiel, P. A. & Bartelt, M. C. Morphological evolution during epitaxial thin flm growth: Formation of 2D islands and 3D mounds. Sur. Sci. Rep. 61, 1–128 (2006).

[53] Stankovich, S. et al. Graphene-based composite materials. Nature 442, 282–286 (2006).

[54] Meyer, J. C. et al. Te structure of suspended graphene sheets. Nature (in the press); doi:10.1038/nature05545.

[55] Nelson, D. R., Piran, T. & Weinberg, S. Statistical Mechanics of Membranes and Surfaces (World Scientifc, Singapore, 2004).

[56] Partoens, B. & Peeters, F. M. From graphene to graphite: Electronic structure around the K point. Phys. Rev. B 74, 075404 (2006).

[57] Morozov, S. V. et al. Two-dimensional electron and hole gases at the surface of graphite. Phys. Rev. B 72, 201401 (2005).

[58] Zhang, Y., Small, J. P., Amori, M. E. S. & Kim, P. Electric feld modulation of galvanomagnetic properties of mesoscopic graphite. Phys. Rev. Lett. 94, 176803 (2005).

[59] Dresselhaus, M. S. & Dresselhaus, G. Intercalation compounds of graphite. Adv. Phys. 51, 1–186 (2002).

[60] Shioyama, H. Cleavage of graphite to graphene. J. Mater. Sci. Lett. 20, 499–500 (2001).

[61] Viculis, L. M., Mack, J. J., & Kaner, R. B. A chemical route to carbon nanoscrolls. Science 299, 1361 (2003).

[62] Horiuchi, S. et al. Single graphene sheet detected in a carbon nanoflm. Appl. Phys. Lett. 84, 2403–2405 (2004).

[63] Krishnan, A. et al. Graphitic cones and the nucleation of curved carbon surfaces. Nature 388, 451–454 (1997).

[64] Land, T. A., Michely, T., Behm, R. J., Hemminger, J. C. & Comsa, G. STM investigation of single layer graphite structures produced on Pt(111) by hydrocarbon decomposition. Surf. Sci. 264, 261–270 (1992).

[65] Nagashima, A. et al. Electronic states of monolayer graphite formed on TiC(111) surface. Surf. Sci. 291, 93–98 (1993).

[66] Van Bommel, A. J., Crombeen, J. E. & van Tooren, A. LEED and Auger electron observations of the SiC(0001) surface. Surf. Sci. 48, 463–472 (1975).

[67] Forbeaux, I., Temlin, J.-M. & Debever, J. M. Heteroepitaxial graphite on 6H-SiC(0001): Interface formation through conduction-band electronic structure. Phys. Rev. B 58, 16396–16406 (1998).

[68] Berger, C. et al. Ultrathin epitaxial graphite: 2D electron gas properties and a route toward graphene-based nanoelectronics. J. Phys. Chem. B 108, 19912–19916 (2004).

[69] Berger, C. et al. Electronic confnement and coherence in patterned epitaxial graphene. Science 312, 1191–1196 (2006).

[70] Ohta, T., Bostwick, A., Seyller, T., Horn, K. & Rotenberg, E. Controlling the electronic structure of bilayer graphene. Science 313, 951–954 (2006).

[71] Tapash Chakraborty, " GRAPHENE: A NANOSCALE QUANTUM PLAYING FIELD", LA PHYSIQUE AU CANADA November / Décembre 2006.

[72] Behnaz Gharekhanlou and Sina Khorasani, "AN OVERVIEW OF TIGHT-BINDING METHOD FOR TWO-DIMENSIONAL CARBON STRUCTURES", Nova Science Publishers, Inc., ISBN 978-1-61470-949-7, pp. 1-36, (2011).

[73] Y. H. Wu1, T. Yu, and Z. X. Shen, "Two-dimensional carbon nanostructures:Fundamental properties, synthesis, characterization, and potential applications ", J. Appl. Phys. 108, 071301 (2010).

[74] Rupali Kundu, "Tight binding parameters for graphene" , Mod. Phys. Lett.B, 25, 163 (2011).

[75] P. Obraztsov, "Nonlinear optical phenomena in graphene based materials" Publications of the University of Eastern Finland Dissertations in Forestry and Natural Sciences Number 47, ISBN: 978-952-61-0549-9, (2011).

[76] S. S. Fan, M. G. Chapline, N. R. Franklin, et al., Science 283, 512 (1999).

[77] L. Schlapbach and A. Zuttel, Nature 414, 353 (2001).

[78] A. C. Dillon, K. M. Jones, T. A. Bekkedahl, et al., Nature 386, 377 (1997).

[79] P. M. Ajayan, O. Stephan, C. Colliex, et al., Science 265, 1212 (1994).

[80] P. C. Collins, M. S. Arnold, and P. Avouris, Science 292, 706 (2001).

[81] Valentin N. Popov, " Carbon nanotubes: properties and application " , Materials Science and Engineering R 43, 61–102, (2004).

[82] M.S. Dresselhaus, G. Dresselhaus, P.C. Eklund, Science of Fullerenes and Carbon Nanotubes, Academic Press, New York, (1996).

[83] A. Jorio, R. Saito, J.H. Hafner, C.M. Lieber, M. Hunter, T. McClure, G. Dresselhaus, M.S. Dresselhaus, Structural (n, m)determination of isolated single-wall carbon nanotubes by resonant Raman scattering, Phys. Rev. Lett. 86, 1118, (2001).

[84] Rajesh Kumar et al. / International Journal of Engineering Science and Technology (IJEST), Vol. 3 No. 7, (5635-5640), July (2011). 183

[85] M. Holzinger, A.Hirsch,_, P. Bernier, G.S. Duesberg, M. Burghard, Appl. Phys. A 70, 599–602, (2000).

[86] Cheng-Hsiung Kuo • Hwei-Ming Huang," Responses and thermal conductivity measurements of multi-wall carbon nanotube (MWNT)/epoxy composites ", J Therm Anal Calorim, 103:533–542 (2011).

[87] Martin Pumera, "Electrochemical properties of double wall carbon nanotube electrodes", Nanoscale Res Lett, 2:87–93 (2007).

[88] Tobias Hertel,Axel Hagen, Vadim Talalaev, Katharina Arnold, Frank Hennrich,| Manfred Kappes,|Sandra Rosenthal, James McBride, Hendrik Ulbricht,† and Emmanuel Flahaut, Nano Letters, Vol. 3, 511-514, (2005).

[89] Lanhua Wei, P. K. Kuo, and R. L. Thomas," Thermal Conductivity of Isotopically Modified Single Crystal Diamond", Phys. Rev. Lett., 70, 24 (1993).

[90] L. Wei, P.K. Kuo and R.L. Thomas, "Determination of the temperature dependent thermal conductivity of isotopically modified single crystal diamond", Colloque C7-229, supplkment au Journal de Physique 111, 4 (1994).

[91] T. Ando, "The electronic properties of graphene and carbon nanotubes", NPG Asia Materials (2009) 1, 17–21; doi:10.1038/asiamat.2009.1.

[92] Valeri N. Kotov , Bruno Uchoa , Vitor M. Pereira , F. Guinea , and A. H. Castro Neto, Rev. Mod. Phys. 84, 1067–1125 (2012).

[93] Davood Fathi, Journal of Nanotechnology, Volume 2011 (2011), Article ID 471241, 6 pages.

[94] H. S. Philip Wong, D Akinwande, "Carbon Nanotube and Graphene Device Physics", Cambridge University Press The Edinburgh Building, Published in the United States of America, New York, (2011). 184

[95] S. Sultan, F. Gao, R. Vickers and C. Zhang, "Electrically Switchable Optical Response in Graphene", IRMMW-THz, 2010 35th International Conference, Rome, 10.1109/ICIMW.2010.5612572, IEEE Confence.

[96] Sung-Hoon Lee , Hyun-Jong Chung , Jinseong Heo ,Heejun Yang , Jaikwang Shin , U-In Chung , and Sunae Seo, ACS Nano, 5 (4), pp 2964–2969, , 2011.

[97] V.M. Pereira, A.H. Castro Neto, Phys. Rev Lett. 103, 046801, (2009).

[98] F. Guinea, M.I Katsnelson, A.K. Geim, Nature Physics, 6, 30, (2009).

[99] G Giovannetti, P.A. Khomyakov, G. Brocks, P.J. Kelly, J. van den Brink, Phys. Rev. B 76, 073103, (2007).

[100] L. Ci, L. Song, C.H. Jin, D. Jariwala, D.X. Wu, Y.J. Li, et al., Nature Mater. 9, 430, (2010).

[101] Y.W. Son, M.L. Cohen, S.G. Louie, Phys. Rev Lett. 97, 216803, (2006).

[102] D.C. Elias, R.R. Nair, T.M.G. Mohiuddin, S.V. Morozov, P. Blake, M.P. Halsall, et al., Science 323, 610 (2009); R. Balog, B. Jorgensen, L. Nilsson, M. Andersen, E. Rienks, M. Bianchi, et al., Nature Mater. 9 (2010) 315; F. Withers, M. Dubois, A.K.Savchenko, Phys. Rev. B 82, 073403 (2010).

[103] Xu Xu-Guang, Zhang Chao, Xu Gong-Jie, and Cao Jun-Cheng, Chin. Phys. B Vol. 20, No. 2 (2011) 027201.

[104] M. Koshino, "Orbital Magnetism of Graphenes-Physics and Applications of Graphene - Theory", Edited by Sergey Mikhailov, ISBN 978-953-307-152-7, Published: March 22nd, 2011 under CC BY-NC-SA 3.0 license, in subject Nanotechnology and Nanomaterials.(395-414) (2011).

[105] Beidou Guo, Liang Fang, Baohong Zhang , Jian Ru Gong, " Graphene Doping: A Review", Insciences J., 1(2), 80-89, (2011).

[106] K. S. Novoselov, A. K. Geim, S. V. Morozov, D. Jiang, Y. Zhang, S. V. Dubonos, I. V. Grigorieva, and A. A. Firsov, Science, 306(5696), 666-669, (2004).

[107] A. K. GEIM AND K. S. NOVOSELOV, " The rise of graphene ", nature materials | VOL 6 | MARCH 2007 | www.nature.com/naturematerials (2007).

[108] E. Stolyarova, K. Taeg Rim, S. Ryu, Janina Maultzsch, Philip Kim, L. E. Brus, Tony F. Heinz, Mark S. Hybertsen, and George W. Flynn, " High-resolution

scanning tunneling microscopy imaging of mesoscopic graphene sheets on an insulating surface", PNAS, vol. 104 , no. 22 _ 9209–9212, May 29 (2007).

[109] Igor A. Luk"yanchuk, and Yakov Kopelevich," Phase Analysis of Quantum Oscillations in Graphite", Phys. Rev. Lett., 93, 16 (2004).

[110] Keun Soo Kim, Yue Zhao, Houk Jang, Sang Yoon lee, Jong Min Kim, et al., Nature , Vol. 5, 706-710 (2009).

[111] A. J. Pollard, R. R. Nair, S. N. Sabki, C. R. Staddon, L. M. A. Perdigao, C. H.Hsu, J. M. Garfitt, S. Gangopadhyay, H. F. Gleeson, A. K. Geim, and P. H.Beton, J. Phys. Chem. C, Vol. 113, 16565- 16567, No. 38 (2009).

[112] Johannes Jobst, Daniel Waldmann, Florian Speck, Roland Hirner,Duncan K. Maude, Thomas Seyller, and Heiko B. Weber, "How Graphene-like is Epitaxial Graphene Quantum Oscillations and Quantum Hall Effect", arXiv:0908.1900 [cond-mat.mes-hall] (2009) .

[113] A. H. Castro Neto, F. Guinea, N. M. R. Peres, K. S. Novoselov and A. K. Geim, "The electronic properties of graphene", REVIEWS OF MODERN PHYSICS, 81, (2009).

[114] K. Nakada, M. Fujita, G. Dresselhaus and Mildred S. Dresselhaus, Phys. Rev. B, 54, 24, 15 December–II (1996).

[115] H. Zheng, Z. F. Wang, Tao Luo, Q. W. Shi, and Jie Chen, PHYSICAL REVIEW B 75, 165414, (2007).

[116] Katsunori Wakabayashi, Ken-ichi Sasaki, Takeshi Nakanishi and Toshiaki Enoki, Sci. Technol. Adv. Mater. 11, 054504 (2010).

[117] K. S. Novoselov, A. K. Geim, S. V. Morozov, D. Jiang, M. I. Katsnelson, I. V. Grigorieva, S. V. Dubonos and A. A. Firsov, Nature 438, 197, (2005).

[118] Y. Zhang, Y. W. Tan, H. L. Stormer and P. Kim , Nature 438, 201 (2005).

[119] A. K. Geim and K. S. Novoselov, Nature Mater. 6, 183 (2007).

[120] Edward McCann and Vladimir I. Fal"ko, "Landau level degeneracy and quantum Hall effect in a graphite bilayer", Phys. Rev. Lett. 96, 086805 (2006).

[121] E. McCann, Phys. Rev. B, 74, 161403(R), (2006).

[122] Hongki Min, Bhagawan Sahu, Sanjay K. Banerjee, and A. H. MacDonald, "Ab initio theory of gate induced gaps in graphene bilayers", Phys. Rev. B 75, 155115 (2007).

[123] M. Aoki and H. Amawashi, Solid State Commun. 142, 123 (2007).

[124] F. Guinea ,A. H. Castro Neto and N M R Peres, Phys. Rev. B 73 245426 (2006).

[125] J. Cserti, A. Csordas, and G. David, Phys. Rev. Lett. 99, 066802, (2007).

[126] Edward McCann and Mikito Koshino, "The electronic properties of bilayer graphene Rep. Prog. Phys., 76 , 056503 (28pp), (2013).

[127] Edward McCann and Mikito Koshino, "The electronic properties of bilayer graphene", arXiv:1205.6953v1, cond-mat.mes-hall, 31 (2012).

[128] Edward McCann, David S.L. Abergel_, Vladimir I. Fal"ko, Solid State Communications 143, 110–115, (2007).

[129] L. A. Falkovsky,"Gate-tunable bandgap in bilayer graphene", Journal of Experimental and Theoretical Physics, February, 110, Issue 2, pp 319-324 (2010).

[130] Y. Kuang and Y. Liu, "Modeling and Design of Graphene GaAs Junction Solar Cell", School of Physics and Electronic Engineering, Changshu Institute of Technology, Changshu 215500, China, (2014).

[131] Song-ang Peng and Zhi Jin, "The sheet resistance of graphene under contact and its effect on the derived specific contact resistivity", Department of Microwave devices and Integrated Circuits, Institute of Microelectronics, Chinese Academy of Sciences, Beijing 100029, China, (2014).

[132] J. W. Weber, V. E. Calado, and M. C. M. van de Sanden, "Optical constants of graphene measured by spectroscopic ellipsometry", Department of Applied Physics, Eindhoven University of Technology, P.O. Box 513, 5600 MB Eindhoven, The Netherlands. (2010).

[133] P. Avouris and M. Freitag, "Graphene photonics, plasmonics, and optoelectronics," IEEE Journal on Selected Topics in Quantum Electronics, vol. 20, no. 1, Article ID 6000112, (2014).

[134] Alina Cismaru, Mircea Dragoman and Adrian Dinescu, "Microwave And Millimeterwave Electrical Permittivity Of Graphene Monolayer", arXiv:1309.0990. Condensed Matter. Mesoscale and Nanoscale Physics. (2013).

[135] T. Feng, D. Xie, Y. Lin et al., "Graphene based Schottky junction solar cells on patterned silicon-pillar-array substrate," Applied Physics Letters, vol. 99, no. 23, Article ID 233505, (2011).

[136] J. Brunton, TCAD Analysis of Heating and Maximum Current Density in Carbon Nanofiber Interconnects Master's Thesis, Naval Postgraduate School, (2011).

[137] L. Lancellotti, T. Polichetti, F. Ricciardella et al., "Graphene applications in Schottky barrier solar cells," Tin Solid Films, vol.522, pp. 390–394, (2012).

[138] Atlas User's Manual *"Device Simulation Software"*, Silvaco, Inc. 4701 Patrick Henry Drive, Bldg. 2. Santa Clara, CA 95054 (2016).